Master Thesis

Investigation of Leading-Edge Vortex Formation on a Robotic Bird's Wing

Master Mechanical Engineering, Energy and Flow
Faculty of Engineering technology (ET)

Author:
Laurens Schalk
S1727850

Exam committee:
Prof. dr. ir. C.H. Venner
Ir. L. Groot Koerkamp
Dr. ir. M.P.J. Sanders
Dr. A. Martinetti Msc.

November 23, 2022
Document number: 416

UNIVERSITY OF TWENTE.

1 Summary

The RoBird is a flapping wing drone that is developed by mimicking a peregrine falcon. It generates both lift and thrust by flapping its wings, similar to how real birds fly. The drone works, but there is still a poor understanding of how and why the aerodynamics work as they do. By investigating the RoBird's aerodynamics, more can be learned about how birds fly. This could help humans for example in designing better drones, but could also help us understand birds, and therefore help us protect them.

This research focuses on leading-edge vortex (LEV) formation on the bottom side of the RoBird's wing. This LEV is an unsteady aerodynamic phenomenon that creates very high lift forces and is a key mechanism that enables insect flight. It's however poorly understood in the context of vertebrate flight as the high Reynolds numbers associated with vertebrate flight and complicated wing designs change the flow and complicate research. It is known that vertebrates are capable of developing LEVs. But even when a LEV is found on a vertebrate's wing, it is often not known for which flight maneuvers they precisely use the LEV, and how different factors influence its formation.

The goal of the research is to find out if leading-edge vortices form on the bottom side of the RoBird's wing during flapping flight. This has been investigated by performing measurements at $0.20 \leq St \leq 0.41$, as most vertebrates fly in this region and cruise at $0.20 \leq St \leq 0.25$ [Nudds et al., 2004] [Taylor et al., 2003]. The selected Reynolds regime is $55.100 \leq Re \leq 106.400$, which has been chosen mainly due to limitations in the measurement set-up used. Three wings have been produced to investigate the effect of leading-edge sharpness on LEV formation. Of these wings, two had a changed leading-edge radius relative to the original RoBird wing design, resulting in a blunt, original, and sharp wing. Based on the performed literature study, the hypothesis has been formed that LEV formation conditions are the most optimal for wings with sharp leading-edges flapping at high Strouhal numbers, and at a Reynolds number of $Re \approx 100.000$. The results of the measurements were used to investigate the effect of the Strouhal number, Reynolds number, and leading-edge shape on LEV formation. This knowledge can be used to test whether or not the mentioned hypothesis is true.

A flapping mechanism that flaps a single RoBird wing up and down has been mounted in the open jet aero acoustic wind tunnel of the University of Twente, where the flow around the flapping wing was measured with particle tracking velocimetry (PTV). This technique works by injecting neutrally buoyant helium-filled soap bubbles into the airflow. By illuminating the bubbles with a powerful laser and recording the reflections with four high-speed cameras, the bubbles can then be converted into digital 3D particle tracks over time, which can be used to analyze the flow. Also, force measurements have been performed by mounting the flapping mechanism on a half-model balance in order to measure the high lift associated with LEVs. No information was available about the angle of the body relative to the wind during flight, so the body has been mounted under zero angle of attack, to serve as a stepping stone for more complicated research. Also, no phase change has been applied to the wing during the flapping motion, due to a non-functioning phase change mechanism.

From the particle tracks, it was found that leading-edge vortices do form in the bottom side of the RoBird's wing, with the only exception being the blunt and sharp wing not forming a LEV at $Re = 55.100$ and $St = 0.20$. The strengths of the LEVs that were found have been quantified using the maximum spanwise velocity inside the vortex U_y since this spanwise flow is crucial for LEV stability according to the literature. The noted values of U_y have been divided by the free stream velocity U_∞, resulting in a relative, dimensionless spanwise velocity U_y/U_∞. Despite being a crude quantification method, the measured vortex strengths could be used to compare the vortex strength for different Strouhal numbers, Reynolds numbers, and the three different leading-edge shapes.

From this comparison, a clear Strouhal number effect could be seen, with increasing vortex strengths for increased Strouhal numbers. At constant $St = 0.20$ a clear Reynolds effect could be seen, with no or weak LEVs at $Re = 55.100$, an apparent peak in LEV strength at $70.900 \leq Re \leq 86.600$ and a decrease in vortex strength for Reynolds numbers beyond the observed peak. This peak is thought to be close enough to the peak observed in literature to be in line with the hypothesis. At $St = 0.26$, no clear Reynolds number effect could be seen. From the comparison of the different leading-edge shapes, no definite statements could be made about its influence on LEV development, as no clear trends were visible and the data seemed to contradict the hypothesis. However, its believed to be likely that for example production inaccuracies have disrupted the measurements, making the comparison of the data of the different leading-edge shapes very hard.

The force data has been filtered and recalculated into aerodynamic force data, showing highly detailed forces acting on the wings during their flapping cycles. However, the results showed large deviations in similar data sets, indicating that a large error has been introduced somewhere along the process, possibly by noise or the calculation of the aerodynamic forces. Therefore the data was deemed unreliable, and force enhancement by LEVs could not be accurately determined.

Table of contents

List of symbols

Symbol	Definition	Dimension
$\mathbf{a}$	Acceleration of air	$[ms^{-2}]$
A	Flapping amplitude, circumferential distance traveled from the midline by an airfoil in the Φ direction	[m]
$\dot{A}$	Flapping velocity, circumferential velocity of an airfoil traveling around the flapping axis	$[ms^{-1}]$
c	Chord length of the wing	$[m]$
d_{p}	Diameter of tracer particle	$[m]$
D	Distance traveled by wing	$[m]$
f	Flapping frequency	$[Hz]$
F	Force	$[N]$
L	Variable used for different dimensions of the flapping mechanism	$[m]$
M	Moment	$[Nm]$
n	Number of data points	[-]
p	Pressure of the air	$[Pa]$
Q	Volume flow rate	$[l/h]$
r	Spanwise distance from the axis of rotation of the flapping motion to an airfoil	$[m]$
Re	Reynolds number	[-]
Ro	Rossby number	[-]
R_{specific}	Specific ideal gas constant for dry air (=278.05)	$[Jkg^{-1}K^{-1}]$
S	Sunderland constant (= 110.4)	$[K]$
St	Strouhal number	[-]
t	Time	$[s]$
t/T	Dimensionless time of a flapping wing	[-]
t^*	Dimensionless time of flat plate under translation	[-]
T	Period, time of a single flapping cycle	$[s]$
T	Temperature	$[K]$
T_{ref}	Reference temperature for Sunderland's law (=273.15)	$[K]$
U_{eff}	Effective velocity experienced by an airfoil	$[ms^{-1}]$
U_{lag}	Velocity lag between a tracer particle and an accelerating fluid	$[ms^{-s}]$
U_y/U_∞	Relative, dimensionless spanwise velocity of air	[-]
U_∞	Free stream velocity	$[ms^{-1}]$
x	Axis in streamwise direction of Cartesian coordinate system	$[m]$
y	Axis in spanwise direction of Cartesian coordinate system	$[m]$
z	Axis perpendicular to $x-y$ plane	$[m]$

Table 1: List of Latin Symbols

Symbol	Definition	Dimension
α	Angle of attack	[°]
α_{eff}	Effective angle of attack	[°]
β	Motor angle	[°]
γ_0	Angle between the midline and the y axis	[°]
Γ	Circulation	$[m^2 s^{-1}]$
Δ	Difference between two values of a variable	[-]
θ	Pitch of the RoBird's wing	[°]
λ	Angle of between RoBird's wing and y axis ($\lambda = \Phi + \gamma_0$)	[°]
μ	Dynamic viscosity of the air	$[Pas]$
μ_{ref}	Reference dynamic viscosity for Sunderland's law ($= 1.813 * 10^{-5}$)	$[Pas]$
ξ	Angle between axis of L_3 and L_4	[°]
ρ	Density of the air	$[kgm^{-3}]$
ρ_{p}	Density of tracer particle	$[kgm^{-3}]$
Φ	Angle between RoBird's wing and the flapping midline	[°]
$\dot{\Phi}$	Angular velocity of RoBird's wing around the flapping axis	$[^\circ s^{-1}]$

Table 2: List of Greek Symbols

2 Introduction

The RoBird is a robotic bird from the company Clear Flight Solutions in Enschede, the Netherlands. Its design is based on a peregrine falcon as can be seen in Figure 1, and it flies by flapping its wings, which creates both lift and thrust. Movable surfaces in the tail allow for further control during flight. The RoBird has been designed by a falconer, who used his experience with falcons and trial and error to produce a flying drone [UToday, 2012]. Although this trial and error approach worked, it results in little understanding of why the drone works, and what aerodynamic mechanisms are working on the RoBird during its flight. The fact that it works, however, makes the RoBird and its wings a good starting point for research into flapping wing aerodynamics.

Figure 1: RoBird (left) and peregrine falcon (right) [Brentjes and Hoeijmakers, 2017]

Flapping-wing drones like the RoBird are typically still outperformed by either fixed-wing- and/or rotary drones. This is for example due to inefficient transmissions, and difficulties in designing for flight modes like hovering [Floreano and Wood, 2015][Chin et al., 2020]. Vertebrates however easily outperform drones in many aspects due to millions of years of evolution and specialization. Migrating birds can travel enormous distances in a single flight, with the longest observed flight being an 11.000 km flight by bar-tailed godwits from Alaska to New Zealand [Gill Jr et al., 2005]. Birds like hummingbirds, but also larger birds such as kites or ospreys are capable of hovering in their search for food. Hunter and prey birds perform high speed or high G maneuvers to capture prey or avoid being captured, like the peregrine falcon, which can reach velocities over 320 km/h during their dive [Ponitz et al., 2014]. Predatory birds like owls can fly with hardly making any sound, making them very hard to spot for their prey [Lilley, 1998].

Understanding the mechanisms that enable these extraordinary skills is vital for developing and improving flapping-wing drones such as the RoBird. These drones not only have the potential to outperform fixed- and rotary-wing drones in performance, their bird-like appearance makes them very useful for scaring off birds at for example airports, or for military and surveillance purposes. Not only humans could benefit from this knowledge, but vertebrates themselves could also benefit. Increased knowledge of their aerodynamics could help explain their behavior, and therefore help humans in protecting them.

This thesis will focus on a specific aerodynamic phenomenon observed mainly in unsteady aerodynamics: a Leading-Edge Vortex (LEV). This aerodynamic structure can develop on the top or bottom of a wing during a respective down- or upstroke and can greatly increase lift forces acting on the wing. It is still poorly understood in the context of vertebrate flight, so using the RoBird wing, particle tracking velocimetry (PTV), and a half-model force balance, its formation will be investigated on the bottom surface of the wing for a blunt, normal, and sharp leading-edge in the range of $55.100 \leq Re \leq 106.400$ and $0.20 \leq St \leq 0.41$.

3 RoBird

In this chapter, the RoBird, its design, and a kinematic model that describes the flapping motion of the RoBird will be discussed. This kinematic model and the resulting effective angle of attack will be used throughout the thesis to describe the moving wing and the resulting flow around the wing.

The exact free flight conditions of the RoBird are disputed. [Brentjes and Hoeijmakers, 2017] claim that it flies with free stream velocity $U_\infty = 8m/s$ and flapping frequency $f = 5Hz$, [Groot Koerkamp, 2018] claims that it flies with $U_\infty = 13.6m/s$ and $f = 5.3\,Hz$, while [Folkertsma et al., 2017] (vaguely) claim that it flies with (or up to) $U_\infty = 16\,m/s$ with either $f = 3\,Hz$ or $f = 6\,Hz$. Research with (some) of these flight conditions would therefore be most relevant for Robird flight, but due to limitations in the measurement set-up, this is not possible. As will be discussed further in Chapter 6.1 and 6.3, the wind tunnel velocity must be $U_\infty \geq 5\,m/s$, while the flapping mechanism is limited to $f \leq \pm 3\,Hz$. This thesis has been made with these limitations taken into account, and therefore not all the results will be applicable to the RoBird itself.

3.1 Design

The RoBird's wings are produced out of 20 kgm^{-3} EPP foam, with two spars running through the wing for extra stiffness, as can be seen in Figure 2. The spars consist of titanium pieces partly sticking out of the wing which are connected to an internal driving mechanism, and carbon fiber tubes which are located inside the wings. Near the tip of the wing, a carbon fiber strip is placed close to the leading-edge, as is highlighted in blue in Figure 2, to provide additional strength and stiffness.

Figure 2: Finished (left) and unfinished (right) RoBird wing. The blue line indicates the position of the carbon fiber reinforcement strip. Modified from [Groot Koerkamp, 2018]

The RoBird's body contains an internal driving mechanism that drives the flapping motion of the wings, as can be seen in Figure 3. The flapping motion starts with a motor rotating with a constant angular velocity. A gear with a 1:1 ratio transfers this rotation to a so-called 'crank rocker' system, which changes the rotation into a flapping motion. Both the leading- and trailing spar are attached to the wings, so their movement determines the movement of the wing. When the motor stops applying energy to the system, the flapping motion stops, and the latching mechanism locks the system in place, which enables the bird to glide. The $\Delta\Phi$ mechanism is a mechanism that rotates the wing in a pitching motion while the wings are flapping, which changes the effective angle of attack. This mechanism is located between the two crank rocker systems and works by letting the leading- and trailing spar move out of phase with each other [Folkertsma et al., 2017].

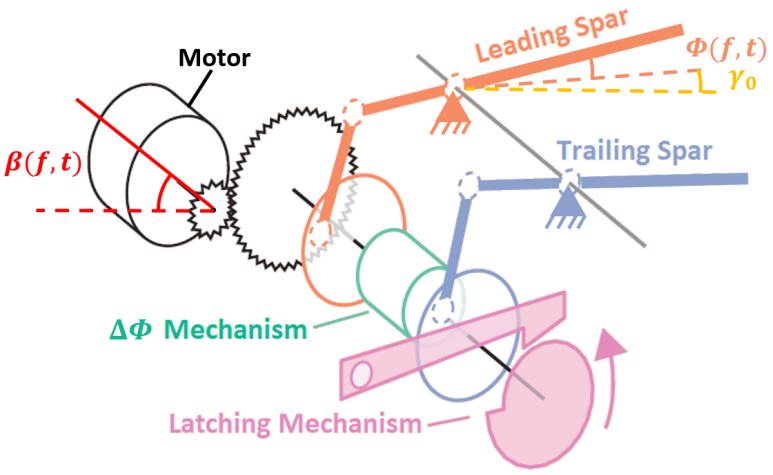

Figure 3: Working principle of the internal driving mechanism of the RoBird. Modified from [Folkertsma et al., 2017]

However, when looking closely at the working principle behind the $\Delta\Phi$ mechanism, it can be seen that the system is over-defined. When the internal mechanism applies a phase change to the spars, they will not be parallel to each other anymore, causing the distance between the spars to increase the further one moves away from the axis of rotation. The spars are locked in place inside the wing, however, as can be seen in Figure 2, and are therefore not able to move. The bending of parts like the spars might allow the phase-change mechanism to work to a certain extent, but it is believed that this design flaw strongly limits the phase-changing capabilities of the internal mechanism.

3.2 Kinematics

The complex motion of a flapping wing can be simplified into a 2D motion by looking at a cross section of the wing and describing it's motion by pitching and the distance the airfoil moves. Pure plunging does not exist when rotating a wing around the x axis, as the airfoil moves in both the z and y direction, which makes the $x-z$ plane unsuitable for describing a 2D flapping motion. The flapping movement of the airfoil can be described in the $x-\Phi$ plane however, by using the circumferential motion of the airfoil as can be seen in Figure 4. The flapping motion's midline is not parallel to the y-axis, but it's slightly tilted. The maximum and minimum flapping angle relative to the y-axis are $42.7°$ and $-28.8°$ respectively, resulting in a midline of the flapping motion under an angle $\gamma_0 = 6.97°$ with respect to the y-axis.

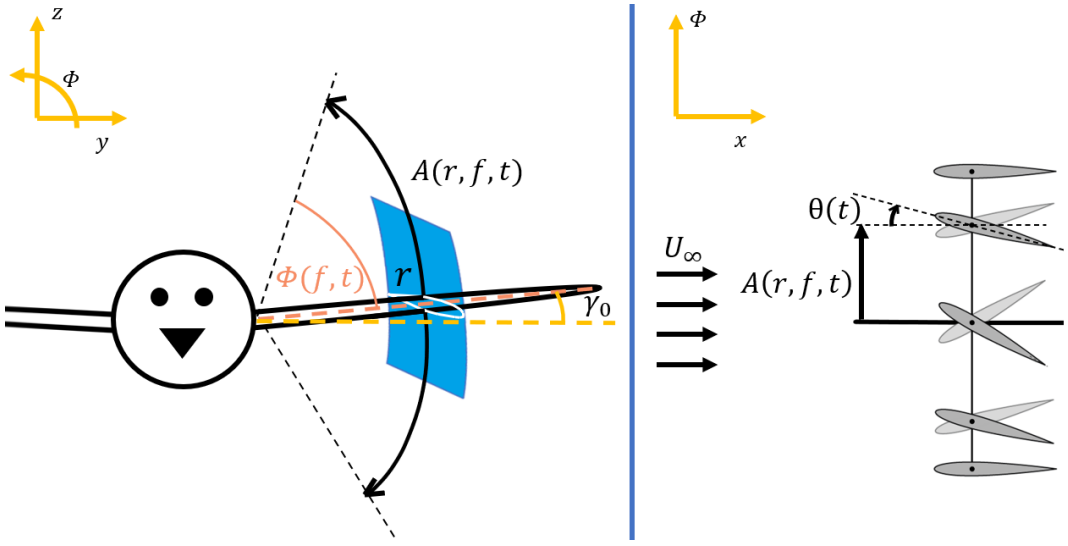

Figure 4: Simplified kinematic motion of flapping bird flight in 2D. Left shows the front view of the RoBird in flight, and the right shows a section view of an airfoil traveling in the $x-\Phi$ plane

The flapping amplitude A is defined as the circumferential distance traveled away from the midline by an airfoil in the Φ direction, and can be calculated as:

$$A(r, f, t) = \frac{2\pi}{360} r\Phi(f, t) \tag{1}$$

Where r is the spanwise distance from the axis of rotation of the flapping motion and $\Phi(f, t)$ is the angle between the RoBird's wing and the flapping midline in degrees. The geometries of the components of the crank rocker mechanism are known, so with the use of the motor angle $\beta(f, t)$ in degrees, a relation between the motor angle and the flapping angle $\Phi(f, t)$ is deducted in Appendix A. The motor angle can then be written as a function of time t and the frequency f as it rotates with constant angular velocity, resulting in the following relation:

$$\begin{aligned}\Phi(f,t) = tan^{-1}&\left(\frac{L_x + L_1\cos(360ft)}{L_y - L_1\sin(360ft)}\right) \quad \cdots \\ - cos^{-1}&\left(\frac{-L_2^2 + L_3^2 + [L_x + L_1\cos(360ft)]^2 + [L_y - L_1\sin(360ft)]^2}{2L_3\sqrt{[L_x + L_1\cos(360ft)]^2 + [L_y - L_1\sin(360ft)]^2}}\right)\end{aligned} \tag{2}$$

Where the constants L_x, L_y, L_1, L_2 and L_3 are dimensions of rigid components of the flapping mechanism, which can be found in Appendix A. The angular velocity $\dot{\Phi}(f, t)$ can now be calculated by differentiating $\Phi(f, t)$ over time while keeping f constant, which is elaborated further in Appendix A. The angular velocity $\dot{\Phi}(R, f, t)$ can now be used to calculate the flapping velocity $\dot{A}$, which is the circumferential velocity of an airfoil traveling around the flapping axis:

$$\dot{A}(r, f, t) = \frac{\partial A(r, f, t)}{\partial t} = \frac{2\pi}{360} r \left(\frac{\partial \Phi(f, t)}{\partial t}\right)_f = \frac{2\pi}{360} r\dot{\Phi}(f, t) \tag{3}$$

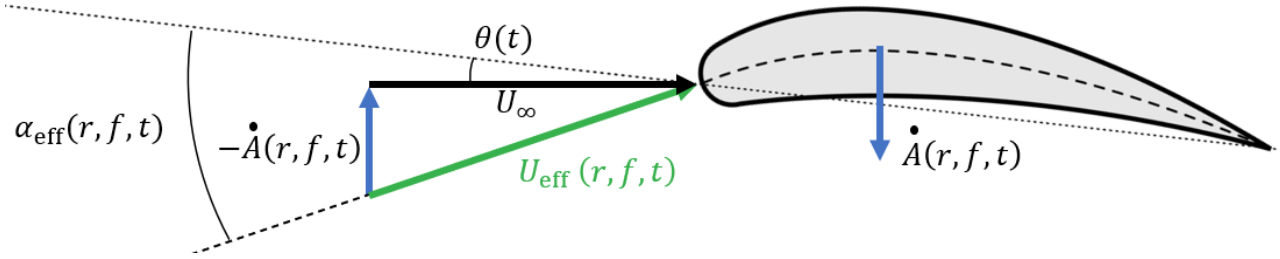

Figure 5: Contributing factors to the effective angle of attack of an airfoil in flapping motion.

With the use of Figure 5, the effective angle of attack α_{eff} can now be calculated at any frequency, time, and location on the wing, as all the velocity components are known. This results in:

$$\alpha_{\text{eff}}(r, f, t) = tan^{-1}\left(\frac{-\dot{A}(r, f, t)}{U_\infty}\right) + \theta(t) \tag{4}$$

Where $\theta(t)$ is the pitch induced by the $\Delta\Phi$ mechanism. Due to the design flaw of the $\Delta\Phi$ mechanism, the phase change of the wing during measurements, and therefore $\theta(t)$, can not accurately be prescribed. Therefore no phase change will be performed, and $\theta(t)$ will be set to zero for this thesis. Figure 6 shows a plot of α_{eff} for different locations on the wing at an exemplary frequency and velocity. From these plots, it can be seen that there is a large difference in α_{eff} during a flapping cycle and at different locations on the wing

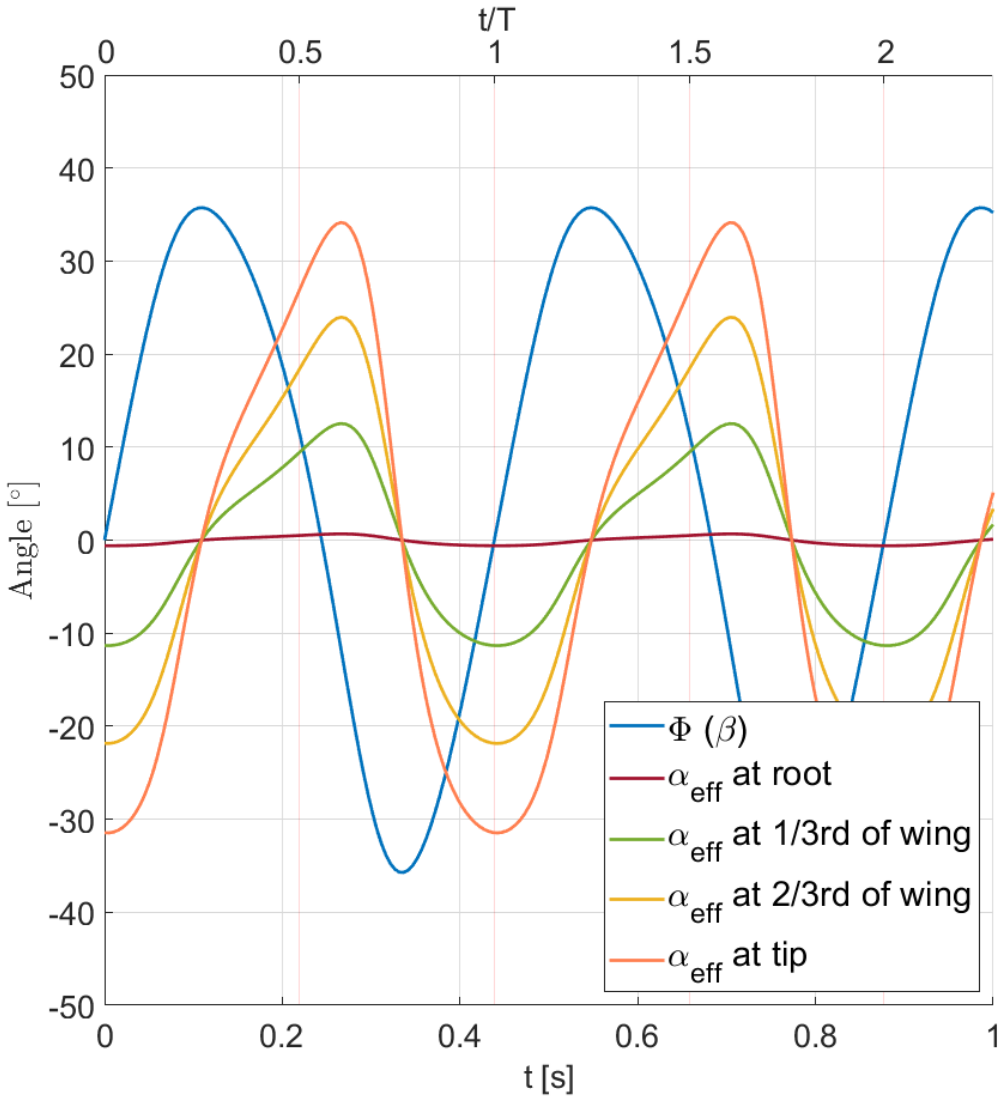

Figure 6: α_{eff} at different locations on the wing for $f = 2.28\,Hz$ and $U_\infty = 7.40\,m/s$. The angles are plotted with both the time in seconds and the non-dimensional time t/T, where the period T is equal to $T = 1/f$.

Note that for the kinematic model of the RoBird some simplifications have been made. In free flight, the body of a bird moves up and down in the opposite direction of the flapping motion, resulting in an extra vertical velocity component. This velocity has been ignored however as its magnitude is relatively small compared to the heaving velocity [Wolf and Konrath, 2015], and the measurement set-up restricts this motion from occurring anyhow. When the body of the bird is placed under an angle relative to the incoming wind, an additional velocity, in the Φ direction will be acting on the wing, changing the effective angle of attack. This has been ignored for the rest of the thesis, as it will make the kinematic model unnecessarily complex. For the equations of Φ and $\dot{\Phi}$ no significant assumptions have been made though, as they are a direct result of the design of the flapping mechanism and the constant motor velocity. For the calculations of the flapping amplitude A, the flapping velocity $\dot{A}$, and α_{eff} the wing has been assumed to be infinitely stiff, while in reality wing bending and twisting due to inertia and aerodynamic loading influence these variables. These complex effects will not be further discussed as it's beyond the scope of this thesis, but it should be remembered that in real life the values of A, $\dot{A}$ and α_{eff} can differ from the simplified model discussed in this chapter.

4 Flapping Wing Aerodynamics

In this chapter, the current knowledge, and gaps in knowledge about flapping wing aerodynamics will be discussed, in particular with respect to leading-edge vortices. This will serve as a foundation for the research questions, which will be discussed in Chapter 5.

4.1 Dimensionless Numbers in Flapping Flight

Before analyzing the research performed on different flying animals, it is first important to be able to compare different research with each other. Therefore, in this section, a framework of dimensionless numbers is established, which combine relevant variables describing kinematics, wing morphology, and air properties. These dimensionless numbers allow for a comparison of different research performed, regardless of for example animal size or flight speed. Note that these dimensionless numbers also allow for comparison with for example swimming animals, but also for example wind turbines, and planes. The flow around a flapping wing can be described by the following dimensionless numbers:

$$Re = \frac{\rho U_\infty c}{\mu} \tag{5}$$

$$St = \frac{2A_{\text{tip}} f}{U_\infty} \tag{6}$$

$$Ro = \sqrt{\left(\frac{1}{2St}\right)^2 + 1} * \frac{r}{c} \tag{7}$$

The Reynolds number Re represents the ratio of inertial to viscous forces, where ρ is the density of the air ($kg\,m^{-3}$), c is the chord length of the wing (m) and μ it's dynamic viscosity ($Pa\,s$). The Strouhal number St describes the kinematics for flapping wings, where $2A_{tip}$ is the peak-to-peak amplitude of the wing tip (m). The Rossby number Ro describes the ratio of inertial to Coriolis forces, where r is the wingspan and c is the chord length. The values of ρ and μ for air have been calculated with the ideal gas law and Sunderland's law respectively, as is further explained in Appendix B, resulting in $\rho = 1.206\ kgm^{-3}$ and $\mu = 1.706 * 10^{-5}\ Pas$. With the use of Equation 1 one can calculate A_{tip} with $\Phi = \Phi_{\text{max}}$ and $r = r_{\text{max}}$:

$$A_{\text{tip}} = \frac{2\pi}{360} r_{\text{max}} \Phi_{\text{max}} \tag{8}$$

Where $\Phi_{\text{max}} = 35.7°$ and $r_{\text{max}} = 0.53\,m$. This results in $A_{\text{tip}} = 0.33\,m$ and a peak-to-peak amplitude of the wingtip of $2A_{\text{tip}} = 0.66\,m$. The chord length used is the average chord length of the RoBird wing, which is $c = 0.16\,m$.

The Reynolds number is the parameter that changes the most over flying animals. The difference in sizes and velocities results in Re values around 1 for small hovering insects to around 1.000.000 for a diving falcon. Most vertebrates fly at $Re > 10.000$, which means that the transition from laminar to turbulent flow can occur [Chin and Lentink, 2016]. The low Reynolds numbers of insect flight result in viscous damping of both small external disturbances, and the wake shed by the insect. The influence of these disturbances and the wake is relatively small for insect flight. Large flyers like birds or bats are more influenced by atmospheric phenomena and shed large wakes since their large Reynolds numbers result in little viscous damping [Swartz et al., 2008]. The Reynolds number does influence unsteady aerodynamic phenomena such as leading-edge vortex structure, but can not fully explain them [Chin and Lentink, 2016]. In order to do so, more dimensionless numbers are needed. Note that local Reynolds numbers differ from the average Reynolds number, due to the varying chord length of the RoBird's wing, and due to varying flow velocities caused by the flapping motion of the wing. This is further elaborated in Chapter 7.1.

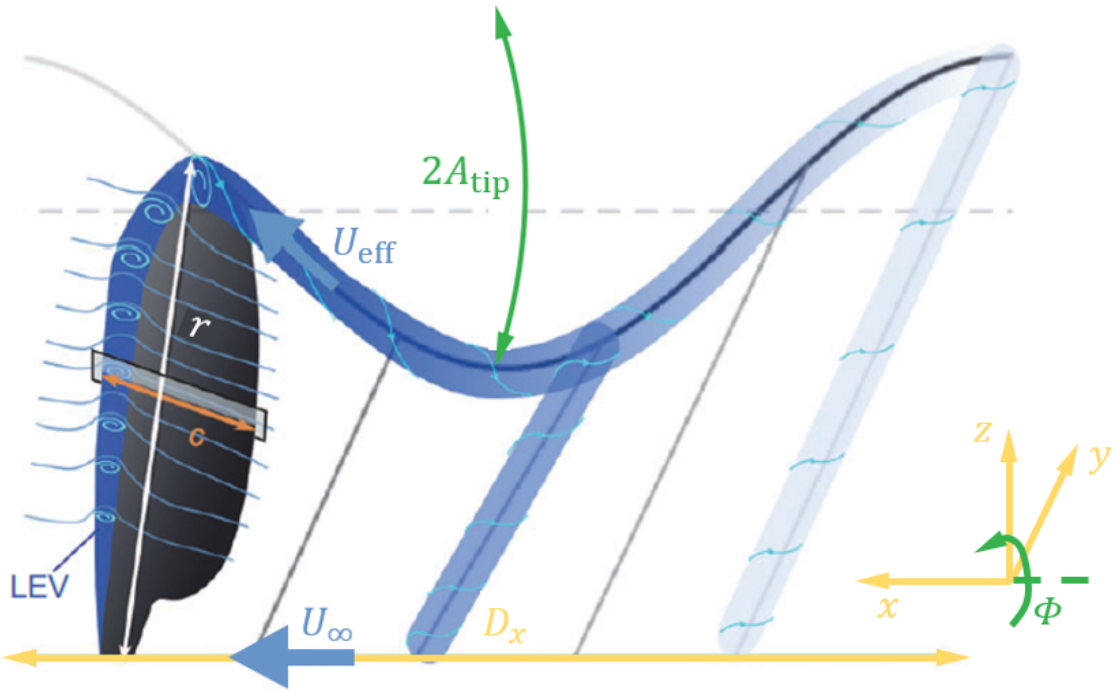

Figure 7: Visualisation of length scales and velocities contributing to the Strouhal- and Rossby number. Adapted from [Chin and Lentink, 2016].

The Strouhal number affects the aerodynamic forces coefficients, as it defines the timescales associated with vortex growth and shedding. The length scales and velocities associated with the Strouhal number can be seen in Figure 7. The Strouhal number can be more intuitively understood by rewriting it to the ratio of effective velocity as experienced by the wing U_{eff} relative to U_∞. It can also be rewritten to the distance traveled in the x direction D_x during one flapping cycle relative to the distance traveled by the wing in the circumferential direction, resulting in:

$$St = \frac{U_{\text{eff}}}{2U_\infty} = \frac{2A_{\text{tip}}}{D_x} \tag{9}$$

Where $U_{\text{eff}} = \sqrt{U_\infty^2 + \dot{A}^2}$, as can be seen in Figure 5. From the first fraction in Equation 9, it can be seen that the Strouhal number defines the ratio between $\dot{A}$ and U_∞, which are precisely the factors contributing to α_{eff}, as is explained in Chapter 3.2. Therefore the Strouhal number defines the effective angle of attack experienced by the wing at a given radius. The usefulness of the Strouhal number for analyzing flapping flight became even more apparent when it was discovered that flying and swimming animals cruise at a narrow range of $0.2 \leq St \leq 0.4$. It is believed that natural selection has caused animals independent of one another and independent of Reynolds number to converge to this narrow range, as this region is associated with peak propulsion efficiencies (mechanical input vs aerodynamic output) [Taylor et al., 2003]. Birds often operate in the lower end of the Strouhal regime, where out of 60 species in cruising flight a mean value of $St = 0.21$ was found for direct flyers, and $St = 0.25$ for intermittent fliers [Nudds et al., 2004].

The Rossby number characterizes the rotational effects acting on the wing during a flapping motion as it compares the rotational wing to the degree of translational movement. It can also be interpreted as the aspect ratio of the wing with respect to the flapping axis or rotation. A Rossby number of approximately four or lower is required for the stability of leading-edge vortices [Lentink and Dickinson, 2009] [Kruyt et al., 2015]. The average Rossby number of over 300 insects, birds, bats, autorotating seeds, and pectoral fins of fish for single-wing aspect ratios were calculated to be $Ro \approx 3$, meaning that they theoretically can create stable LEVs. The Rossby number varies over the wingspan due to variations in c and r, which is further elaborated in Chapter 7.1.

4.2 Leading-Edge Vortex Importance

Flying animals use all kinds of unsteady aerodynamic phenomena to produce enough lift and thrust. This section will discuss some of these phenomena and highlight the importance of leading-edge vortices in animal flight.

The unsteady aerodynamic phenomena of animal flight are in themselves not easy to investigate due to their time dependency, but large flying animals like birds and bats make research even more complex. These animals can change all kinds of variables of their wings like the local angle of attack, camber, or aspect ratio [Wolf and Konrath, 2015] [Norberg, 2012] and the large Reynolds numbers associated with these animals can create turbulent airflow. Due to this, it is very difficult to distinguish what causes certain aerodynamic phenomena and why the airflow behaves as it does. Due to their small size, insect wings have a relatively simple shape, without any possibility of actively morphing them. Insects can therefore change relatively few variables during their flight, resulting in a relatively good understanding of the mechanisms that enable insect flight. Some aerodynamic mechanisms in insect flight are for example added mass and wing-wake interaction. Added mass is caused by accelerating and decelerating a wing, resulting in a similar acceleration or deceleration of the air close to the wing as the air can not move through the wing, effectively creating extra inertia [Sedov, 1965]. Wing-wake interaction occurs when the wing passes through a strong velocity field created by shed vortices of previous wing beats, which can increase aerodynamic forces [Dickinson et al., 1999]. It is not unlikely that these or other aerodynamic mechanisms are also present in vertebrate flight, but this has not yet been studied thoroughly [Chin and Lentink, 2016].

The most important aerodynamic feature in insect flight however is the absence of stall, caused by a leading-edge vortex. This leading-edge vortex was found to be sufficient to explain the difference in forces as calculated from 'quasi-steady' models, and actual measurements [Dickinson and Gotz, 1993] and was proven to be present on insect wings by [Ellington et al., 1996]. This leading-edge vortex occurs in flapping flight during the upstroke or downstroke at a high angle of attack. The flow can separate at the leading-edge, after which the flow rolls up into a stable leading-edge vortex. Behind the leading-edge vortex, the flow attaches to the wing, which maintains the Kutta condition and therefore prevents stall [Dickinson and Gotz, 1993].

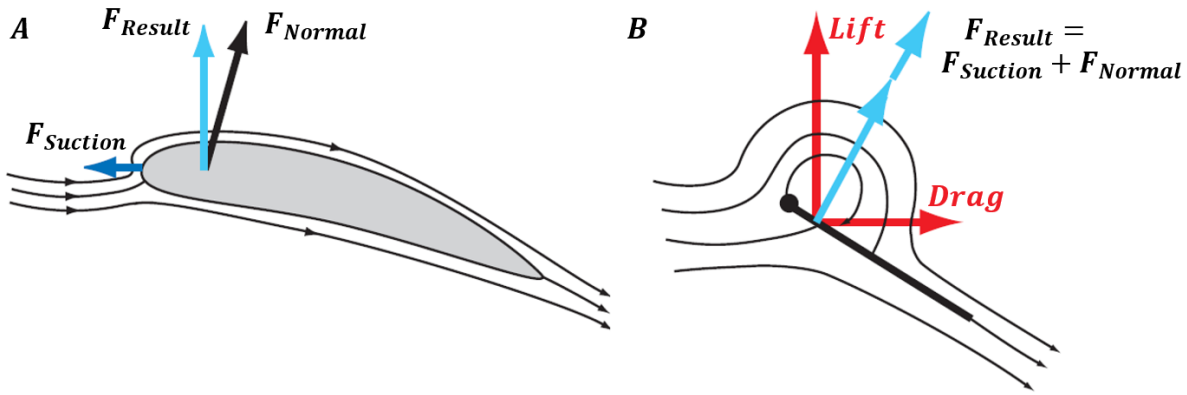

Figure 8: Force generation due to flow around a blunt wing (A) and flow around a thin wing with a leading-edge vortex (B) [Sane, 2003].

The high lift associated with a leading-edge vortex can be explained well with Polhamus' leading-edge suction analogy [Polhamus, 1966]. When air arrives at the leading-edge of a blunt airfoil, the flow must change direction drastically in order to follow the highly curved leading-edge. As can be seen in Figure 8A, this creates a suction force parallel to the wing chord (dark blue arrow). When combining this force component and the potential force component acting normal to the wing plane (black arrow), the resulting force will be perpendicular to the free flow. For airfoils with a sharp leading-edge and a leading-edge vortex this suction force does not form parallel, but normal to the plane of the wing,

as can be seen in Figure 8B. When combining this force component and the potential force component acting normal to the wing plane, it can be seen that the force component pointing upwards has increased compared to the blunt airfoil, but at the cost of added drag [Dickinson and Gotz, 1993]. Simulations of unstable 2D leading-edge vortices over a thin plate reveal a clear region of low pressure under the leading-edge vortex. As the LEV grows in size, this region of low pressure grows both in magnitude and size. When the vortex starts breaking off of the wing and moves away a clear drop in generated lift was found for all evaluated angles of attack [Eldredge and Jones, 2019].

Another way of explaining the lift-enhancing capabilities of a LEV is with circulation Γ. Due to the circulation inside the LEV, the airflow over the wing is given an extra 'push' by which it flows faster over the wing than it normally would. This acceleration of the air on the top of the wing results in a lower pressure, and therefore a stronger pull on the wing normal to the surface of the wing [Ellington et al., 1996]. The circulation inside a LEV is therefore often used to calculate the forces acting on a wing [Chin and Lentink, 2016].

4.3 Leading-Edge Vortex Diversity

Leading-edge vortices can be found in a wide range of applications. This section will discuss some examples of different applications of LEVs and will discuss their presence on vertebrate wings and the differences in observations when a LEV is found.

After the discovery of leading-edge vortices, it was first applied to delta-wing planes with sharp leading-edges at high angles of attack. This caused the flow to separate, after which it formed a stable leading-edge vortex, capable of producing high lift coefficients [Wilson Jr and Lovell, 1947]. Stable leading-edge vortices have been observed on autorotating plant seeds, where it is most prominent near the base, after which it merges with the tip vortex. The high lift produced by the leading-edge vortex allows the seeds to have a longer descent time and a greater wing loading compared to non-autorotating seeds. This gives autorotating seeds a relative advantage in the dispersion of seeds [Lentink and Dickinson, 2009]. Unstable leading-edge vortices can also form on high-lift yacht sails with a sharp leading-edge, where they can produce more than 20% of the total lift, after which they are shed into the wake [Arredondo-Galeana and Viola, 2018].

Interestingly, leading-edge vortices have also been observed for a large range of different vertebrates. Videler et al. were one of the first to observe leading-edge vortices in a water tunnel on models of swift wings during gliding flight. These vortices were found for relatively small angles of attack of $5 < \alpha < 10$. The paper hypothesizes that the LEV is mainly used for demanding flight maneuvers, as the leading-edge vortex not only creates lift but also drag [Videler et al., 2004]. A study with hummingbird wings found a high lift-to-drag ratio, which was believed to be caused by leading-edge vortices [Altshuler et al., 2004]. PIV measurements on a hovering hummingbird indeed confirmed their presence during the downstroke and found that approximately 75% of the weight support was produced during this downstroke [Warrick et al., 2005]. PIV measurements around the wings of a slow-flying passerine revealed a leading-edge vortex on top of the wing during the downstroke supporting up to 49% of the weight. The increase in circulation strength of the LEV during the downstroke suggests that the LEV is not stable. Contrary to earlier observations, the LEV is relatively weak at the wing tip and stronger closer to the root. This may be explained by the bending of the feathers, causing a decrease in α_{eff} when moving towards the wing tip [Muijres et al., 2012]. Studies into bats have found prominent leading-edge vortices on top of the wing during the downstroke, as well as a leading-edge vortex of reversed spin on the bottom of the outer wing during the upstroke. Muijres et al. found that the leading-edge vortex provides significant lift support at slow flight speeds, but no leading-edge vortex was found during cruising flight. Due to the drag associated with leading-edge vortices, it is hypothesized that bats avoid generating them in cruising flight to increase efficiency [Muijres et al., 2014]. Measurements with a model of a pigeon wing found stable leading-edge vortices for $0.20 \leq St \leq 0.30$ and unstable leading-edge vortices at $St = 0.40$ [Thielicke and Stamhuis, 2015]. This indicates that pigeons can use leading-edge vortices even during cruising flight.

4.4 Leading-Edge Vortex Stability

Despite the importance of the leading-edge vortices in animal flight, the vortices found when researching flapping flight are not always stable. This section will discuss what causes this instability, and what factor prevents instabilities from forming.

Wings with a 2D motion like translation, plunging, and pitching always show an unstable leading-edge vortex, given that a leading-edge vortex is found. If a leading-edge vortex is formed in 2D, the shear layer keeps feeding the leading-edge vortex, resulting in an increase in both strength and size of the vortex. The region of reattachment of the flow behind the vortex moves downstream as the vortex grows until it reaches the trailing edge. When the stagnation point reaches the trailing edge, the flow separates, and the vortex breaks away from the surface, as can be seen in Figure 9. After the vortex detachment, a clear drop in the lift is observed [Eldredge and Jones, 2019].

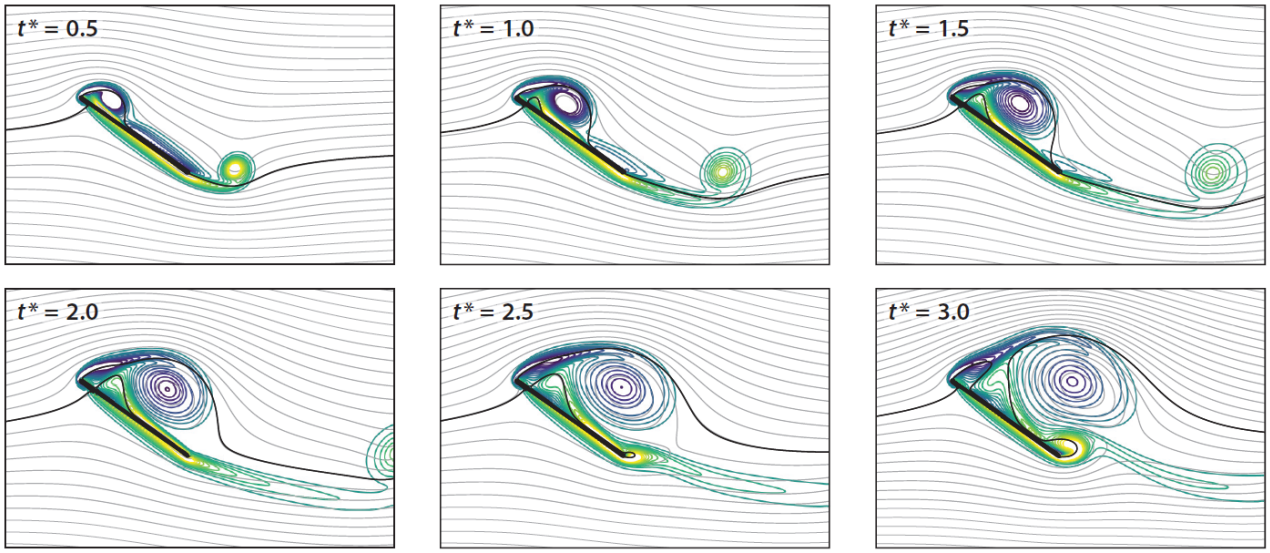

Figure 9: Streamlines (grey), vorticity field (colored), and stagnation streamlines (black) around a flat plate under translation at $\alpha = 35°$ and $Re = 500$. The dimensionless time t^* is given by $t^* = \frac{tU_\infty}{c}$, where t is the time, U_∞ is the plate velocity and c is the chord length [Eldredge and Jones, 2019].

Contrary to 2D flows, a 3D vortex can remain stably attached to the surface of a wing, with a near-constant strength and near-constant position on the wing. This is caused by spanwise flows through the center of the vortex balancing the inflow of mass and vorticity coming from the shear layer which feeds the leading-edge vortex [Eldredge and Jones, 2019]. It was found that these spanwise flows are caused by 'quasi-steady' centripetal and Coriolis accelerations directed in the spanwise direction caused by the angular velocity of the wing. This stabilization mechanism is independent of the Reynolds number for at least the insect Reynolds regime [Lentink and Dickinson, 2009]. Despite 3D effects being able to stabilize leading-edge vortices, they do not always stabilize the flow on 3D wings in practice. One example is the flow around a flapping goose's wing at $28.000 \leq Re \leq 113.000$, where the observed leading-edge vortex both on the top and bottom of the wing during down- and upstroke had a strong tendency to change into flow separation. The authors explain this however by the high Rossby number on the wing, which is $Ro \approx 15$ [Hubel and Tropea, 2010].

4.5 Leading-Edge Vortex Definition

Hubel and Tropea investigated the flow around a flapping goose model, and stated that a fully developed leading-edge vortex is characterized by the reverse flow direction close to the upper surface. The paper claims that their PIV measurements show a stable leading-edge vortex present on the upper surface, and backs this claim with vector fields where the average velocity is subtracted [Hubel and Tropea, 2010]. These images indeed show a circulating flow on top of the airfoil, but it is debatable whether or not the authors have spotted a real leading-edge vortex. Close to the wing, the air must move at the same velocity as the wing due to the no-slip condition, therefore the velocity after subtracting U_∞ must be approximate $-U_\infty$. The air is accelerated over the suction side of an airfoil, meaning that after subtracting U_∞ the velocity vector is still positive. For positive angles of attack, there will therefore always be a circulation and reversed flow visible in the vector field on the upper surface, when U_∞ is subtracted from the vector field, while the actual flow does not need to have any reversed flow. This does not automatically mean that there is no leading-edge vortex present on the top surface of the goose wing model in flapping flight, but the method of detecting it is dubious.

Muijres et al. identifies 2 different vortex structures that can be present on a slow-flying passerine's wing: A laminar separation bubble and a leading-edge vortex [Muijres et al., 2012]. A laminar separation bubble (LSB) occurs on the suction side of a wing at a relatively low angle of attack ($\alpha \approx 7°$) when laminar flow can not follow the curvature of a wing due to the adverse pressure gradient becoming too large. This causes the flow to separate after which it becomes turbulent. The turbulent flow can better follow the curvature of the wing than a laminar flow and is therefore able to reattach. This effectively creates a bubble of relatively small height compared to its length, with little energy exchange and a strong recirculating zone at the back of the bubble. An LSB is generally not desired as it increases drag and can burst, which causes either a sudden shift in pressure distribution or complete stall [Muijres et al., 2012][Jahanmiri, 2011].

Leading-edge vortices are typically produced at the leading-edge due to separated flow at higher angles of attack ($\alpha > 20°$) [Muijres et al., 2012], although their formation has also been observed for $\alpha > 5°$ [Videler et al., 2004]. A leading-edge vortex starts after the flow has detached at the leading-edge. The generated vorticity near the leading-edge forms a shear layer that quickly rolls up into a LEV. During the growth of a LEV, reversed flow and secondary vorticity is created under the LEV. When this region meets the feeding shear layer, a characteristic lambda-shaped region of counter-rotating vorticity is created upstream of the leading-edge vortex [Eldredge and Jones, 2019]. An example of this can be seen in Figure 9, where the flow around a translating flat plate is simulated. The produced LEV has a very similar height and chordwise width [Muijres et al., 2012].

Based on the mentioned characteristics of leading-edge vortices, the following criteria have been found to identify a leading-edge vortex: A rotating structure with reversed flow needs to be visible without subtraction of U_∞. This structure needs to be generated relatively close to the leading-edge and needs to have a more or less similar height and width. Extra certainty in the identification can be obtained by detecting a strong vorticity in the structure's core, and by identifying a lambda-shaped region of counter-rotating vorticity. Spanwise flow is in itself not enough to identify a leading-edge vortex, as it is only crucial for stability, and not for leading-edge vortex formation, as discussed in Chapter 4.4. Observed spanwise flow combined with other observed characteristics, does make it more likely though that an observed structure is a leading-edge vortex.

4.6 Influences on Leading-Edge Vortex Formation

Leading-edge vortex formation is influenced by dimensionless numbers like the Reynolds- and Strouhal numbers, and by morphological wing features. This section investigates the effect of these different parameters on leading-edge vortex formation for vertebrate flight, and identifies a research gap. The parameters with large effects are identified and combined into a hypothesis about leading-edge vortex development. This hypothesis, combined with the research gap, is used to formulate research questions in Chapter 5.

4.6.1 Morphology

A bird's wings consists of a so-called arm wing located close to the body, which is often relatively cambered and thick. Attached to this arm wing is the hand wing, which is often relatively thin, has a sharp leading-edge, and has a lower camber [Thielicke and Stamhuis, 2015], as can be seen in Figure 10a. The RoBird's wing design is based on a real peregrine falcon, resulting in a relatively similar wing as birds typically have, with a strongly cambered arm wing, with a swept back hand wing of decreasing camber, as can be seen in Figure 10b.

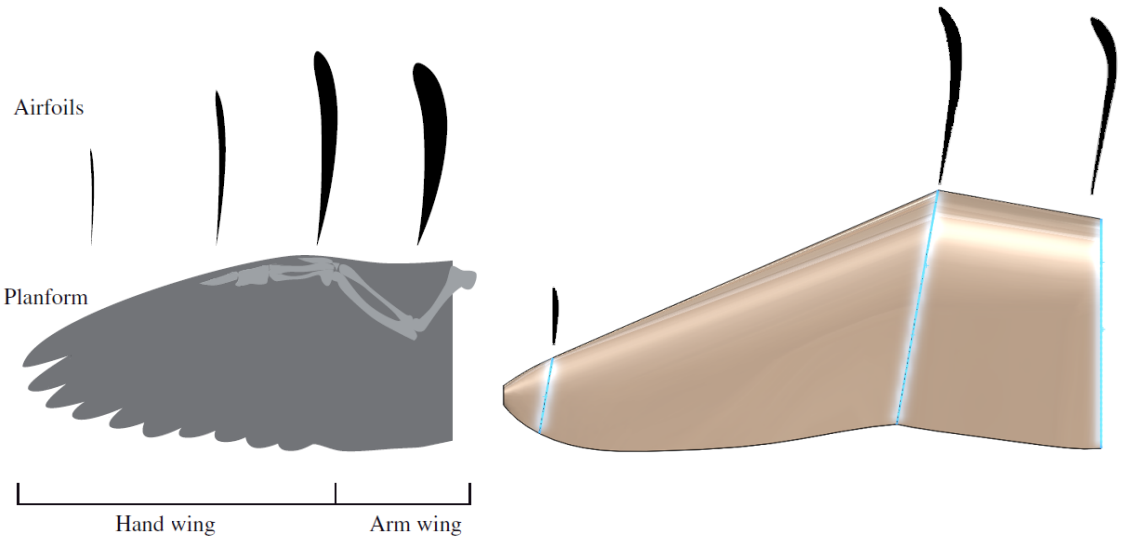

(a) Typical bird wing, with different airfoil cross sections. Modified from [Thielicke and Stamhuis, 2015]

(b) RoBird wing with three different airfoils

Figure 10

Vertebrates can change their wing shape during a wing beat cycle both passively (e.g. bending and twisting due to aerodynamic and inertial forces) and actively (e.g. changing camber, wing sweep, leading-edge shape, angle of attack). Due to the complexity of vertebrate wing shape, researchers have focused on investigating the effects different morphological wing parameters have on the flow field for flapping flight. Since leading-edge vortices can be such prominent lift-enhancing mechanisms, a lot of this research has focused on the effect all of these parameters have on any possible leading-edge vortices:

Contrary to delta wing planes, the sweep angle is not necessary to maintain stable leading-edge vortices, but it probably is helpful in enhancing its stability [Lentink and Dickinson, 2009]. The effect of thickness is difficult to investigate independent of other parameters, as it's liked to the maximum leading-edge radius. It is believed however from research into a pigeon's wing model wing at $22000 \leq Re \leq 26000$ and $0.2 \leq St \leq 0.4$ that thin wings in flapping flight create a stronger leading-edge vortex compared to thicker wings, which increases the total bound circulation. At $St = 0.40$, thin wings create more unstable leading-edge vortices though. Thin wings are desirable from an inertial point of view, as they lower the power requirements during flapping flight. Both inertial and aerodynamic advantages of thin wings might explain the typically observed thin hand wings of birds

[Thielicke and Stamhuis, 2015]. The aerodynamic effect of thickness is less pronounced than the effect of camber though. From the research into the pigeon's wing model wing, it was found that higher-cambered wings had an increased total bound circulation, and increased leading-edge vortex stability, but the leading-edge vortices were of lower strength and smaller size. The effect of camber varies over the span of the wing. At the same time, camber increased circulation in the inner 50% of the wing and decreased the leading-edge vortex strength for the outer 50% of the wing [Thielicke and Stamhuis, 2015]. A study into rotating insect wings at $120 \leq Re \leq 1500$ found that positive cambered wings had the highest lift-to-drag ratio, as the suction of the leading-edge vortex acted on a plane facing relatively upwards [Harbig et al., 2013]. Bats are capable of making large changes in the camber [Norberg, 2012], resulting in the speculation that they utilize this feature to actively control leading-edge vortices throughout their flight [Hedenström and Johansson, 2015].

The parameter that is mentioned most often in the literature however is leading-edge sharpness due to its large influence on leading-edge vortex development. Research with 2D simulations into tilting airfoils with different leading-edge radii in a flow of $1000 \leq Re \leq 1.000.000$ showed for the entire investigated Reynolds domain that the sharper the airfoil, the more prone it was to develop a leading-edge vortex [Ramesh et al., 2012]. Experiments with a plunging profile with three different leading-edge geometries at $Re = 10.000$ and $St = 0.16$ found that sharp leading-edges developed leading-edge vortices a bit earlier than round profiles, while the growth rate of the vortex remained the same [Rival et al., 2014]. These observations make intuitive sense, as a sharp leading-edge can support little suction compared to a round leading-edge, resulting in faster separation of flow at the leading-edge. Bats can not only change the camber but also the leading-edge shape of their wings [Norberg, 2012], which again makes it plausible that they utilize this feature to actively control leading-edge vortices throughout their flight [Hedenström and Johansson, 2015].

4.6.2 Dimensionless Numbers

The Strouhal number is found to be the most important dimensionless number influencing leading-edge vortex formation. As discussed in Chapter 4.3, the low Strouhal numbers linked to cruising flight do not always result in leading-edge vortices, although their development is possible. In the upper Strouhal regime close to $St = 0.4$, it is believed that leading-edge vortices are essentially unavoidable [Nudds et al., 2004].

The effect of the leading-edge radius is strongly dependent on the Reynolds number. In steady conditions for $Re > 10^6$, a large leading-edge radius will allow a much larger range of angles of attack before flow separation occurs. This effect becomes smaller for decreasing Reynolds numbers until the angle of attack range is the same for $Re = 10^4$ [Thielicke and Stamhuis, 2015]. Research into unsteady flow with a model insect wing at $Re \approx 8000$ found that the measured force coefficients were hardly affected when changing the leading-edge thickness, wing camber or twist [Usherwood and Ellington, 2002]. 2D simulations into pitching airfoils with different leading-edge shapes at $1000 \leq Re \leq 1.000.000$ also found little difference in leading-edge vortex formation at low Reynolds numbers for the different shapes. As the Reynolds number increased, however, the positive effect of a sharp leading-edge on leading-edge vortex formation became more and more significant. For $Re > 5000$ leading-edge vortices developed more easily regardless of leading-edge shape as Reynolds numbers increased, up until $Re = 100.000$, where leading-edge vortices were most likely to develop. At the Reynolds numbers investigated beyond this value ($Re = 500.000$ and $1.000.000$), leading-edge vortices were less likely to develop as the Reynolds number increased. These simulations suggest that the optimal conditions for leading-edge vortex formation are on a wing with a sharp leading-edge, somewhere between $50.000 < Re < 500.000$, most likely close to $Re = 100.000$ [Ramesh et al., 2012]. Note however that due to the large jumps in Reynolds numbers investigated ($Re = 50.000$, 100.000, 500.000, etc.), the true optimum might still be relatively far away from $Re = 100.000$.

As discussed in Chapter 4.1 and 4.4, the Rossby number is a measure of leading-edge vortex stability. Even when a wing has a higher Rossby number than four, a wing can still locally produce stable LEVs close to the root, as the $\frac{r}{c}$ component is low there, resulting in Rossby numbers lower than four. An example of this is wind turbine blades, where the flow near the hub undergoes a '3D stall' very similar to flow on revolving insect wings [Lentink and Dickinson, 2009]. The Rossby number is not important for the formation itself of leading-edge vortices though.

4.6.3 Research Gap and Hypothesis

The morphological parameters that were identified to influence leading-edge vortex formation the most were camber and leading-edge radius. Of the dimensionless numbers, the Strouhal- and Reynolds numbers have the greatest influence on leading-edge vortex formation. From the literature, the following recommendations were found for further studies:

A study into a flapping goose model at $28.000 \leq Re \leq 113.000$ found leading-edge vortices for $Re < 77.000$, despite using a wing with a relatively round leading-edge. Therefore, the authors recommend continuing research with sharper wings, as it should enhance leading-edge vortex development even more [Hubel and Tropea, 2010]. [Lentink and Dickinson, 2009] state that more research is needed into the influence of airfoil shape on LEV development, stability, and the forces generated by the LEV in the $10.000 \leq Re \leq 100.000$ domain. [Thielicke and Stamhuis, 2015] state that more research is needed at $Re > 100.000$ to gain insight into the effect of the leading-edge radius at higher Reynolds numbers.

The main research gap is whether or not leading-edge vortices form on the wing of the RoBird during flight, since still very little is known about their presence on vertebrate wings. Although the effect of the Strouhal number on leading-edge vortex formation seems clear, it is not clear at which Strouhal numbers leading-edge vortices start to form precisely for different Reynolds numbers. Based on this, and the recommendations from the literature, the research will be performed such, that if leading-edge vortices are found, the influence of the leading-edge radius, the Reynolds and Strouhal number can be investigated. Based on Chapter 4, the following hypothesis is therefore formed, which will serve as a foundation for the research questions in Chapter 5:

"Leading-edge vortex formation on flapping vertebrate wings will be the most profound for sharp wings operating at high Strouhal numbers and $Re \approx 100.000$."

5 Research Questions

The measurement set-up limitations are first identified in this chapter. These limitations, combined with the research gap as identified in Chapter 4 will form the research questions of this thesis.

The flapping mechanism's phase-changing capabilities are severely limited, as discussed in Chapter 3.1, so no attempts will be made in performing measurements with a varying pitch. No further information exists about the body angle of attack of the RoBird, so the choice has been made to mount the wing in the wind tunnel under zero angle of attack. The results from this thesis can therefore be used as a stepping stone to more complicated research, for example with a wing under an angle of attack.

As will be discussed further in Chapter 6.1 and 6.3, the wind tunnel velocity must be $U_\infty \geq 5\,m/s$, while the flapping mechanism is limited to $f \leq \pm 3\,Hz$. These restrictions in the measurement set-up strongly limit the measurements possible with the RoBird wing. As discussed in Chapter 4.1, a Strouhal range of $0.20 \leq St \leq 0.40$ is most relevant for vertebrate flight. Using these limitations, a measurement matrix is constructed which can be seen in Figure 11.

Re:	**55.100**	***63.000***	***70.900***	***78.800***	***86.600***	***98.500***	***106.400***
U_∞ [m/s]:	5,18	*5,92*	*6,66*	*7,40*	*8,14*	*9,25*	*9,99*
St:	**f [Hz]:**	**f [Hz]:**	**f [Hz]:**	**f [Hz]:**	**f [Hz]:**	**f [Hz]:**	**f [Hz]:**
0,20	1,60	1,83	2,05	2,28	2,51	2,85	*3,08*
0,26	2,00	2,28	2,57	2,85	*3,14*		
0,31	2,40	2,74	*3,08*				
0,36	2,79	*3,19*					
0,41	*3,19*						

Figure 11: Measurement matrix which is possible due to set-up limitations. Orange frequencies are possibly not achievable by the flapping mechanism. Green regions are the selected measurement frequencies.

The green region is the region selected for the measurements in this thesis. The region $0.20 \leq St \leq 0.26$ is important as this is the range where most vertebrates cruise, indicating maximum flight efficiency. At $Re = 55.100$ a Strouhal sweep over the entire $0.20 \leq St \leq 0.41$ range is possible, which enables a Reynolds-independent study. The three remaining measurement frequencies have not been investigated, as there would not have been enough data to perform a proper Reynolds of Strouhal sweep. Note that the selected Reynolds and Strouhal numbers seem relatively arbitrary, but this is due to updated values of ρ, A_{tip} and c after the measurements and wing production, which resulted in a change of St and Re.

Due to the limited knowledge about leading-edge vortices in vertebrate flight, the main focal point of this thesis is investigating whether or not LEVs form on the bottom of the RoBird's wing with the use of particle tracking velocimetry (PTV) measurements. The flow over the top of the wing has also been measured, but due to the large amount of data gathered, investigating these measurements was beyond the scope of the thesis. This results in the main research question:

- **Are leading-edge vortices present on the bottom surface of the RoBird's wing under zero angle of attack for** $0.20 \leq St \leq 0.41$ **and** $55.100 \leq Re \leq 106.400$**?**

From the literature study the following hypothesis was formulated regarding factors influencing leading-edge vortex formation:

"Leading-edge vortex formation on flapping vertebrate wings will be the most profound for sharp wings operating at high Strouhal numbers and $Re \approx 100.000$"

In order to investigate whether or not this hypothesis is true, the following subquestions are formulated:

- What is the influence of the leading-edge radius on leading-edge vortex formation on the flapping wing of a robotic falcon under zero angle of attack for $0.20 \leq St \leq 0.41$ and $55.100 \leq Re \leq 106.400$?
- What is the influence of the Reynolds number on leading-edge vortex formation on the flapping wing of a robotic falcon under zero angle of attack for $0.20 \leq St \leq 0.26$ and $55.100 \leq Re \leq 106.400$?
- What is the influence of the Strouhal number on leading-edge vortex formation on the flapping wing of a robotic falcon under zero angle of attack for $0.20 \leq St \leq 0.41$ and $55.100 \leq Re \leq 86.600$?

During the wind tunnel measurements, a force balance will be mounted in the wind tunnel below the flapping mechanism. The goal of this force balance is to link the particle tracking data to the actual force data, such that more can be learned about the force-enhancing capabilities of leading-edge vortices. However, the University of Twente has no prior experience with such kind of force measurements, so the following subquestions are formulated:

- Can force measurements with a half-model balance reliably be used to determine lift and drag forces acting on the RoBird's flapping wing in a wind tunnel?
- Can force measurements with a half-model balance distinguish force enhancement due to the presence of leading-edge vortices?

6 Methods

In order to investigate the research questions from Chapter 5, measurements have been performed in a wind tunnel with the use of Particle Tracking Velocimetry (PTV), a flapping mechanism, a force balance, and self-produced RoBird wings. This chapter will explain and discuss these methods and tools, such that their strengths and limitations become apparent.

6.1 Wind tunnel

The measurements have been performed in the open jet closed circuit aero acoustic wind tunnel of the University of Twente. A schematic view of the relevant sections can be seen in Figure 12. The air starts in the settling chamber (A), where it undergoes a 10:1 contraction into the closed- (B) and then semi-open (C) test section, with a turbulence intensity of below 0.08%. The closed- and semi-open test section are located inside the anechoic chamber (D), which is large enough to place all the measurement equipment used throughout the experiment. The collector (E) is placed inside the wall of the anechoic chamber and collects the air coming from the semi-open test section, after which it is pumped back toward the settling chamber. For more information about the wind tunnel, the reader is referred to [de Santana et al., 2018].

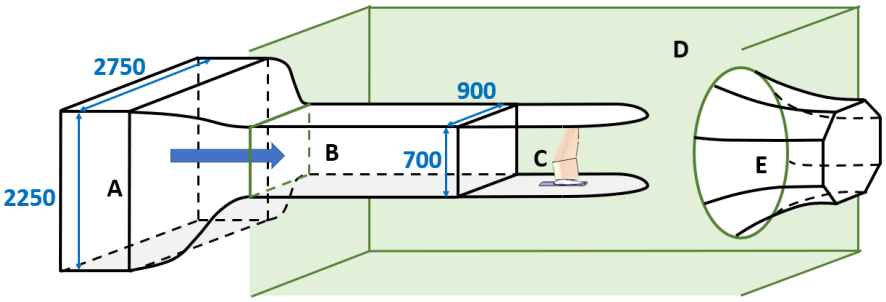

Figure 12: Schematic view of a section of the open jet closed circuit wind tunnel with flapping model mounted in the semi-open test section. Relevant dimensions are in mm.

Calibration of the wind tunnel has been performed at the start of each day before experiments were performed with the use of a pitot tube mounted to the top of the closed test section, as can be seen in Figure 13. This resulted in the required power input settings for that specific day to obtain the desired flow velocity. It was observed that for $U_\infty < 5\,m/s$ no accurate calibration could be made due to fluctuations in the measured flow velocity, resulting in $U_\infty \geq 5\,m/s$ as a requirement for the measurements.

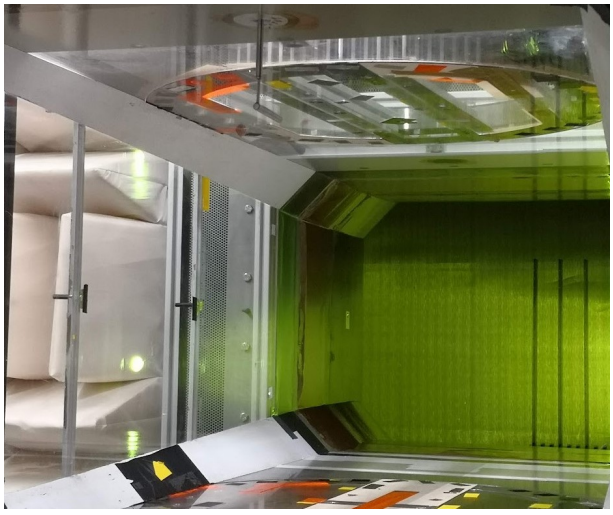

Figure 13: Pitot tube mounted on top of the closed test section, within the background linear nozzle arrays for bubble generation

6.2 Particle Tracking Velocimetry

In order to detect possible leading-edge vortices, a visualization of the airflow is necessary. The method selected for this visualization is particle tracking velocimetry (PTV). As can be seen in Figure 14, this method works by injecting tracer particles into the air upstream of the test section. When these particles are illuminated by a strong laser, one can film the reflections coming from the particles from different angles with multiple high-speed cameras. These recordings can be used to determine the particle positions in 3D space with the use of triangulation. When a small enough Δt is used between recordings, the different particle positions in 3D space can be converted into particle tracks in 4D (3D space + time) with the use of a so-called 'Shake-the-box' algorithm. PTV has been selected for this thesis due to its capability of measuring large volumes of air, but also since strong velocity gradients are expected due to leading-edge vortices, and PTV is an excellent method in capturing this [Raffel et al., 2018].

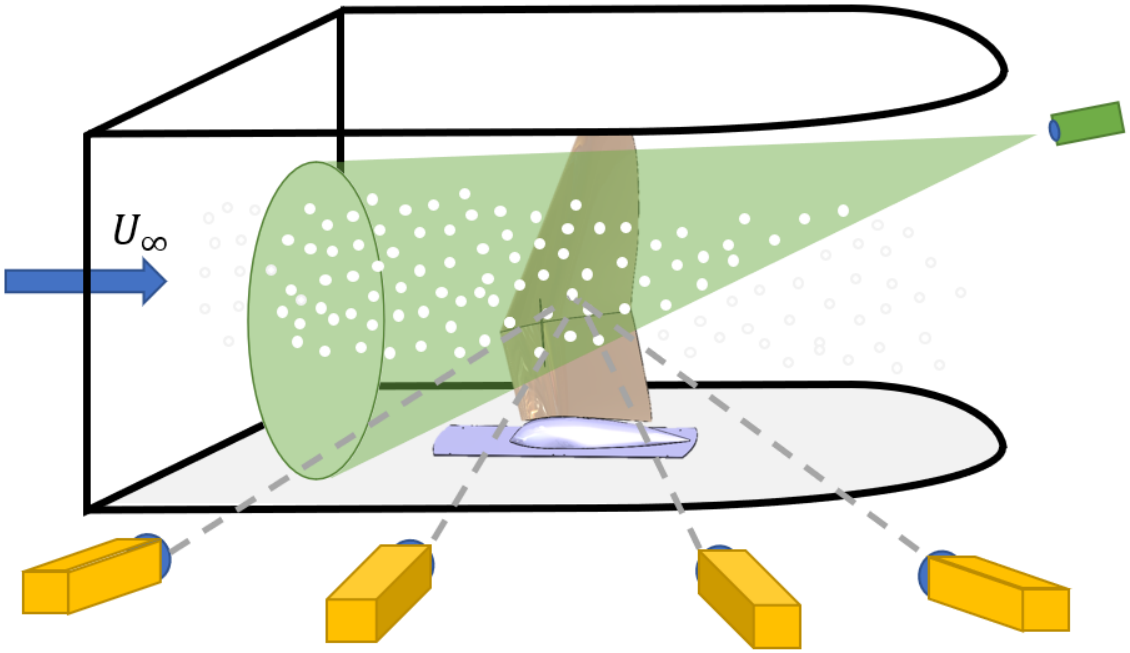

Figure 14: Experimental arrangement of PTV in a wind tunnel

If one wants to visualize the air, the injected particles must follow the air as well as possible. The velocity lag U_{lag} between a given particle and an accelerating fluid must therefore be as close to 0 as possible. When assuming that the particles are spherical in a viscous fluid at a very low Reynolds number, its equation can be obtained from Stokes' drag law [Raffel et al., 2018] and can be seen below:

$$\mathbf{U}_{\text{lag}} = d_{\text{p}}^2 \frac{(\rho_{\text{p}} - \rho)}{18\mu}\mathbf{a} \tag{10}$$

Where $\mathbf{a}$ is an acceleration of the air, μ the dynamic viscosity of the air, d_p the particle diameter, and $\rho_p - \rho$ the difference in particle and air density. From Equation 10 it can be concluded that either the particle diameter should be as small as possible, or the particle density should be identical to the air density, and therefore neutrally buoyant. Large particles have the advantage that they reflect a lot of light, which allows for a large, and especially thick measurement domain, enabling volumetric measurements. Therefore PTV works by using neutrally buoyant particles with a large diameter compared to conventional seeding particles: sub-millimeter helium-filled soap bubbles (HFSBs).

6.2.1 Bubble Generation

The HFSB generator used for the experiment is the LaVision Fluid Supply Unit combined with four linear nozzle arrays spaced 120 mm apart, as can be seen in Figure 15a and 15b. The linear nozzle arrays are made out of NACA0016 profiles with 20 specialized nozzles coming out of the trailing edge spaced 40 mm apart, resulting in 80 nozzles in total in an area of $360 * 760\, mm^2$. The linear nozzle arrays have been mounted on a base and placed inside the wind tunnel settling chamber, causing the lowest nozzles to be located 650 mm from the floor of the settling chamber. The area with bubbles should decrease in size according to the 10:1 wind tunnel compression, resulting in a theoretical bubble area inside the test section of 118 mm width, 236 mm height located 200 mm from the test section's floor.

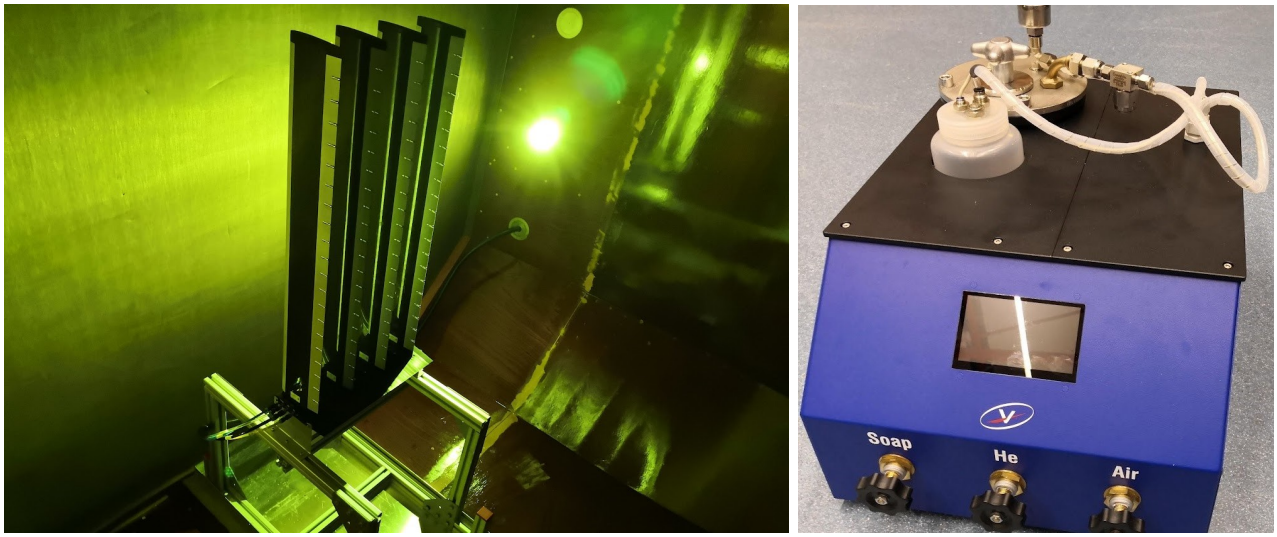

(a) Linear nozzle array's mounted on the base inside wind tunnel settling chamber

(b) Fluid Supply Unit

Figure 15

Helium filled soap bubbles are created with air, helium, and bubble fluid solution (BFS), which is the SAI 1035 from Sage Action, Inc. When they flow through a nozzle, as is displayed in Figure 16, bubbles are formed by either bubbling or jetting. In order to create neutrally buoyant bubbles, there are generally four different parameters one can change: The amount of air, helium, and BFS added, and the nozzle geometry. For this thesis, the nozzle geometry can not be changed however as it is already produced by LaVision's design. It is unknown how this design looks like precisely, but it's expected to be very similar to the 'DLR' design of Figure 16, as DLR helped LaVision design their nozzles. Therefore, effectively only three parameters can be changed.

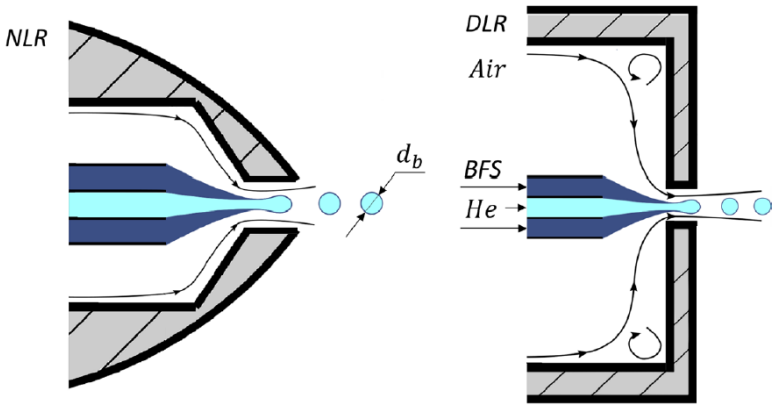

Figure 16: Schematic sectional view of the bubble generator nozzles used by [Faleiros et al., 2019]

Research into the operating regimes of the two bubble generator nozzles as displayed in Figure 16 found that in practice a $Q_{\mathrm{He}}/Q_{\mathrm{BFS}} = 900 \pm 50$ is needed to produce neutrally buoyant bubbles. Compared to the theoretically predicted $Q_{\mathrm{He}}/Q_{\mathrm{BFS}} \cong 1080$, this requires a bit more BFS due to spillage. By trying different air and helium flows, and by looking at the resulting bubble production regimes, a graph could be made showing a monodisperse neutrally buoyant regime for different air- and helium flow inputs. As can be seen in Figure 17, the average bubble diameter $\langle d_{\mathrm{b}} \rangle$ and average bubble production rate $\langle f \rangle$ are consequences of air- and helium flow inputs [Faleiros et al., 2019].

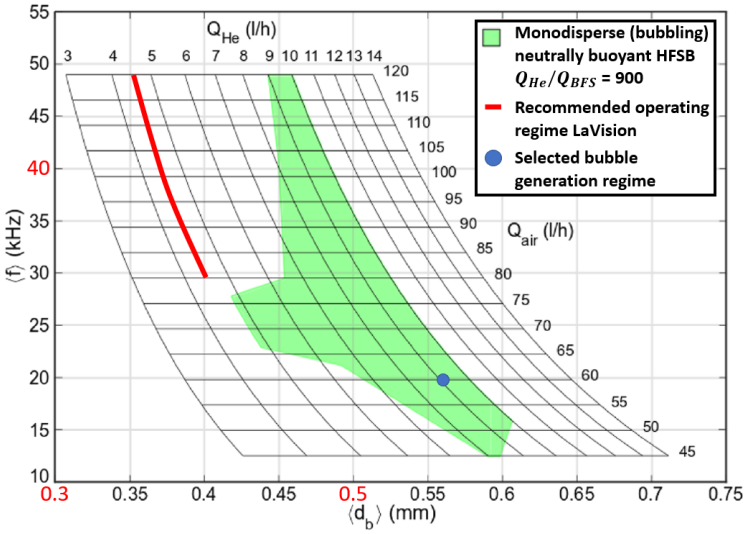

Figure 17: HFSB production rate and diameter as a function of air- and helium flow rates [Faleiros et al., 2019], the operating regime as recommended by LaVision when assuming $Q_{He}/Q_{BFS} = 900$ and the selected bubble generation regime.

The documentation provided by LaVision states that the airflow per nozzle can be adjusted from 80-160 l/h for each nozzle with a BFS flow of $5\,ml/s$, resulting in bubble sizes ranging from $0.3\,mm \leq \langle d_{\mathrm{b}} \rangle \leq 0.5\,mm$, with a production rate of $\langle f \rangle \approx 40\,kHz$ per nozzle. This region lies outside the green region of Figure 17, and for $Q_{air} > 120\,l/h$ even outside of the graph. Furthermore, the maximum achievable droplet size should be $\langle d_{\mathrm{b}} \rangle \approx 0.4\,mm$ when using $Q_{air} = 80\,l/h$ and the fixed production rate of $40kHz$ do not correspond to the variable production rate of $29\,kHz \leq \langle f \rangle \leq 49\,kHz$ as can be seen in the graph. These contradictions raise questions about the correctness of either LaVision's documentation or the research of Faleiros et al.. Bubble generation tests with the input settings as provided by LaVision resulted in a poor generation of HFSBs, while tests within the green region of Figure 17 seem to produce bubbles very well. Due to these tests, combined with the vague, partly contradicting input settings provided by LaVision and the lack of proof provided with their documentation it is believed that the research of Faleiros et al. is more credible. Therefore LaVision's recommendations have further been ignored, and the green region of Figure 17 has further been used as a guideline to produce neutrally buoyant HFSBs.

During the calibration of the test set-up, it was found that relatively large particles were needed in order to obtain strong enough reflections from the bubbles, which resulted in the setpoints $Q_{BFS} = 10\,ml/h$, $Q_{He} = 9\,l/h$ and $Q_{air} = 60\,l/h$. Throughout the experiments, these values could vary slightly. The maximum and minimum values of each respective flowrate have been documented in table 3, resulting in $905 \leq Q_{He}/Q_{BFS} \leq 914$, which is within the 900 ± 50 range. From Figure 17 it can be seen that these input settings should result in $\langle d_{\mathrm{b}} \rangle \approx 0.56\,mm$ and $\langle f \rangle \approx 20\,kHz$

Soap [ml/h]	He [l/h]	Air [l/h]
$9.92 \leq Q_{BFS} \leq 10.02$	$Q_{He} = 9.07$	$58.69 \leq Q_{air} \leq 61.00$

Table 3: Maximum and minimum flow rates observed throughout the experiments

6.2.2 Laser and Camera Set-up

In order to film the bubbles, four high-speed cameras have been mounted on a stand inside the anechoic chamber directed towards the flapping wing, as can be seen in Figure 18a. The two outer cameras were the Phantom VEO 710 18GB with a CMOS sensor with a resolution of 1280×800 pixels combined with VZ scheimpflug adapter V3 with AF Nikkon 50mm f/1.4 D lenses mounted on them. The two middle cameras were the Phantom v611 8GB with a similar CMOS sensor with a resolution of 1280×800 pixels, combined with VZ scheimpflug adapter V4.1 with AF Nikkor 50mm f/1.8 D lenses mounted on them. The scheimpflug adapters allow for a shift in the plane of focus for the cameras since they are all mounted under a different angle with respect to the wing. The exposure time used for the cameras is $300\,\mu s$ per laser pulse, with a lens f-stop of 1.8.

The laser used is the Photonics DMX-527DH. It was operated at a single pulse on maximum power, with a frequency of $2\,kHz$ with an illumination time of $0.5\,\mu s$ per pulse. The laser is connected to LaVision's laser guiding arm, as can be seen in Figure 18b. At the end of the laser guiding arm, a focus lens and a diverging lens is mounted with a focal length of $-50\,mm$, which spreads out the beam into a large volume. The end of the laser guiding arm is mounted to the top of the semi-open test section and pointed toward the bottom of the wing. The laser was cooled using the HC025H1-06A(C48) cold water chiller.

A LaVision Precision Timing Unit was used to synchronize the laser pulse and camera recordings with precise trigger pulses. To minimize reflections coming off the wind tunnel itself, everything in the view of the cameras has been painted or has been taped over with matt black paint or tape. Behind the flapping mechanism in the open part of the semi-open test section, a black cloth was clamped, such that the anechoic chamber could not be seen anymore.

(a) Four high-speed camera's mounted on a stand and laser guiding arm mounted on top of the semi-open test section all directed towards the bottom of the wing

(b) Laser connection with laser guiding arm

Figure 18

The entire set-up as shown in Figure 18 has been built twice, in order to measure the airflow both on the top and bottom of the flapping wings. This has been done by effectively mirroring the camera- and laser set-up relative to the flapping set-up. A schematic view of both set-ups and the relevant dimensions can be seen in Figure 19. More pictures of both set-ups can be seen in Appendix D.

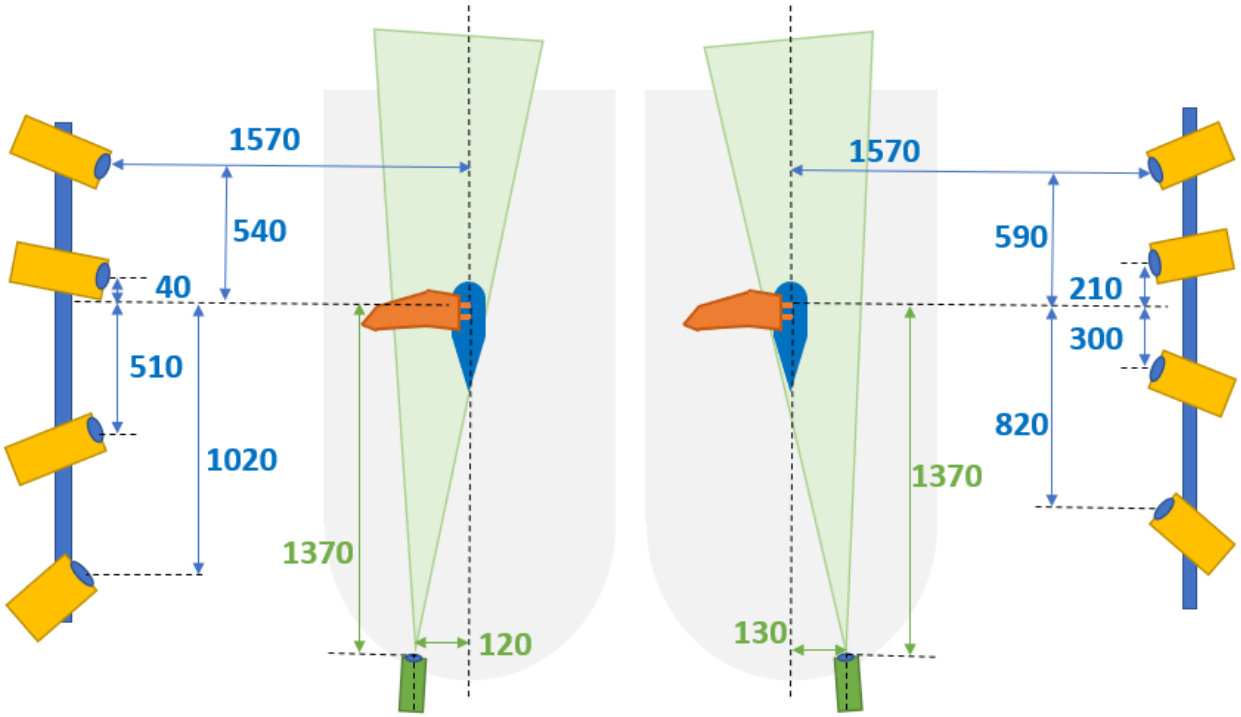

Figure 19: Camera and laser positioning with relevant dimensions in mm for measurements of the flow over the bottom of the wing (left) and over the top of the wing (right).

At the beginning of each measurement day, the cameras were calibrated with the use of a LaVision 2-level calibration plate of type 309-15. As can be seen in Figure 20, the plate was placed in the middle of the measurement volume parallel to the flow direction. With the use of the plate, the cameras were focused, and the scheimpflug angle was adapted such that the entire plate was in focus. The plate was moved back and forth to two more locations, after which each camera was calibrated. This results in the mapping of worldly xyz points into points on the camera chip.

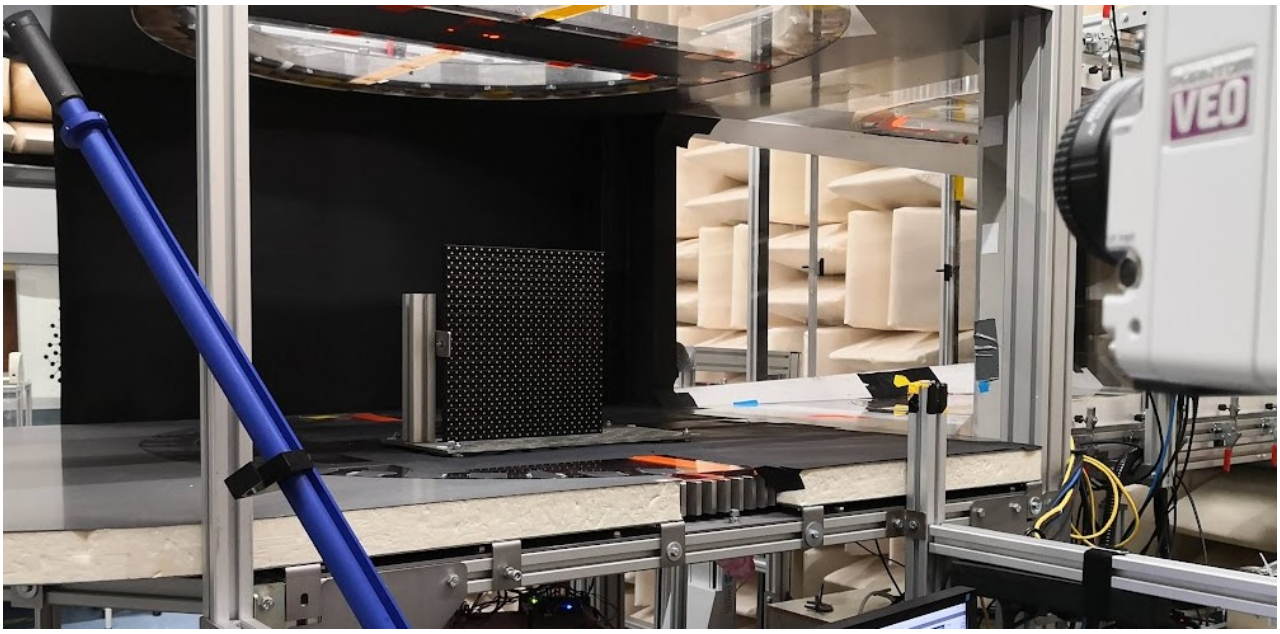

Figure 20: Calibration of the cameras using the LaVision 3D calibration plate.

6.2.3 Creating Particle Tracks

Each measurement day after camera calibration, a volume self-calibration (VSC) has been performed with a measurement of HFSBs in free flow without flapping wing. This VSC corrects small misalignments in the mapping function obtained from the camera calibration with the use of the residual triangulation error (disparity) of actual particle recordings. This can also reduce ghost particles [Wieneke, 2008]. As an enhancement to the VSC, an optical transfer function (OTF) has been applied to the data. This OTF corrects for optical distortions of the particles, mostly due to blurring and astigmatism, resulting in improved position accuracy and a lower ghost particle intensity [Schanz et al., 2012]. After the VSC and OTF, two filters have been applied to the data, such that the background, reflections coming from the wing, and noise were removed as much as possible. The first filter was a subtract time filter, which subtracts a Gaussian average, with the output format set the same as the input format. The second filter was an image preprocessing filter, where the local filters were set to 'subtract sliding minimum' with 5 pixels, normalized with the local average, and the local average was smoothed over 300 pixels for each image separately. The effect of the filters can be seen in Figure 21, where an example of data recorded by one of the cameras before and after the filter can be seen.

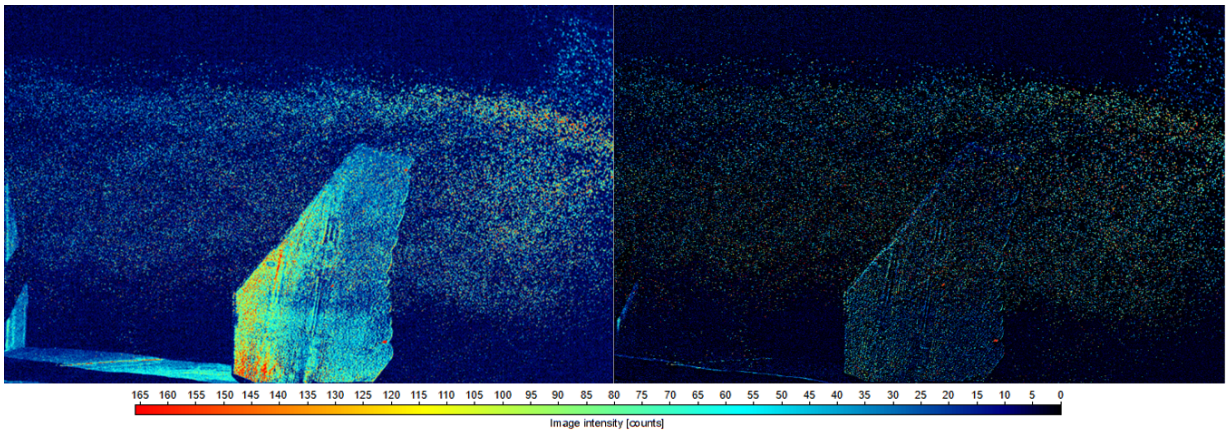

Figure 21: Data before (left) and after (right) applying the two filters.

After applying the VSC, OTF, and filters, the data is suitable for creating particle tracks with the use of a 'Shake The Box' algorithm. This algorithm first uses known path lines to predict where the particle of that specific line will be at t_{n+1}. The errors introduced by this prediction are then corrected by 'shaking' the particles in 3D space to their correct position until they match the images. The majority of the particles have known path lines, and can therefore be filtered out of the data. The residual images can then be used to identify new, untracked particles using triangulation. By comparing these particles to previous time steps, new particle tracks can be created with these particles when at least four consecutive time steps form a reasonable trajectory. The particles can then again be 'shaken' to decrease residual errors. A particle is assumed to be 'lost' when its intensity comes below a certain threshold or when it either reaches the measurement volume border, resulting in removal from the tracking process. This can be done by iterating only a few times until either a track is created, a particle is remembered for later time steps, or a particle is rejected. Solving a single time step is relatively low effort, as the system is largely pre-solved and requires only small corrections. This can be repeated for all time steps until all the flapping cycles are solved [Schanz et al., 2016]. For more information about the VSC and OTF steps and Shake the Box, the reader is referred to [Raffel et al., 2018].

An example of the result after these processing steps can be seen in Figure 22. A 3D environment with particle tracks is created, which move through the environment as time progresses. Based on the particle track data it was found that the seeding area is approximately 200 mm in width and 300 mm in height, which is quite larger than the theoretical seeding area. The cameras are capable of capturing larger volumes, as the wing contour was tracked beyond the region where particles were located. The length of the measured volume is approximately 600 mm long.

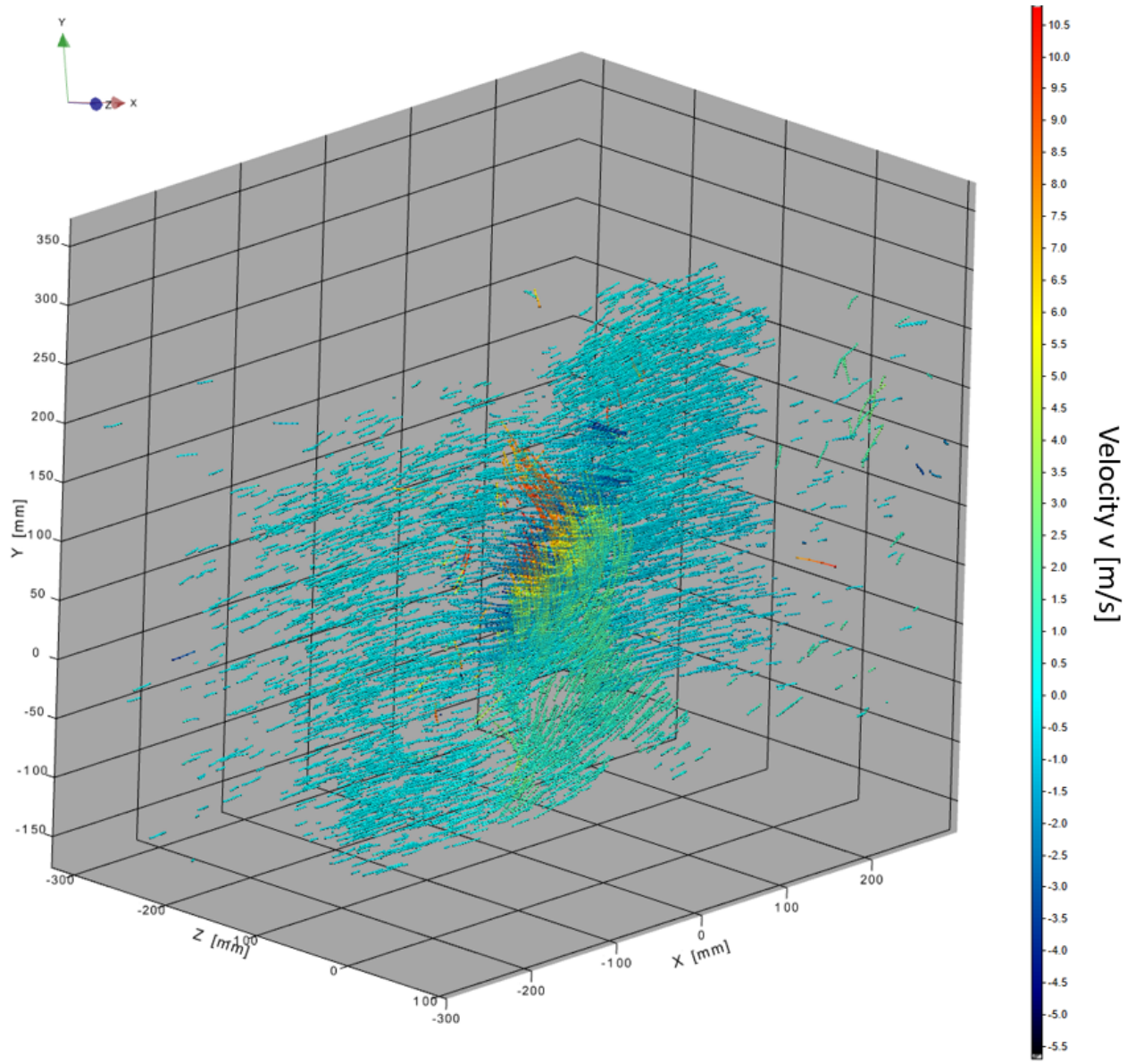

Figure 22: Example of particle tracks in 3D environment

The angle of the wing Φ corresponding to certain stages of leading-edge vortex development in the particle tracks has been determined by placing a model of the wing in ParaView 5.11.0-RC1 together with the particle tracks. The wing was then rotated such that it almost touched the particles closest to the wing, resulting in a known angle that could be recalculated to a value of Φ.

6.3 Flapping Mechanism

The mechanism used to flap the wing in the experiments is designed by the University of Twente and can be seen in Figure 23. It consists of a power supply (A), a RamStix circuit board (B), a trigger output (C), two Maxon Escon 50/5 motor controllers (D), and the flapping mechanism itself containing two Maxon EC 32 brushless 80W motors (E). The force balance used can also be seen in Figure 23, as it is mounted below the force balance and clamped to the table. Wings can be interchanged by clamping the two wing spars in place with Allen bolts.

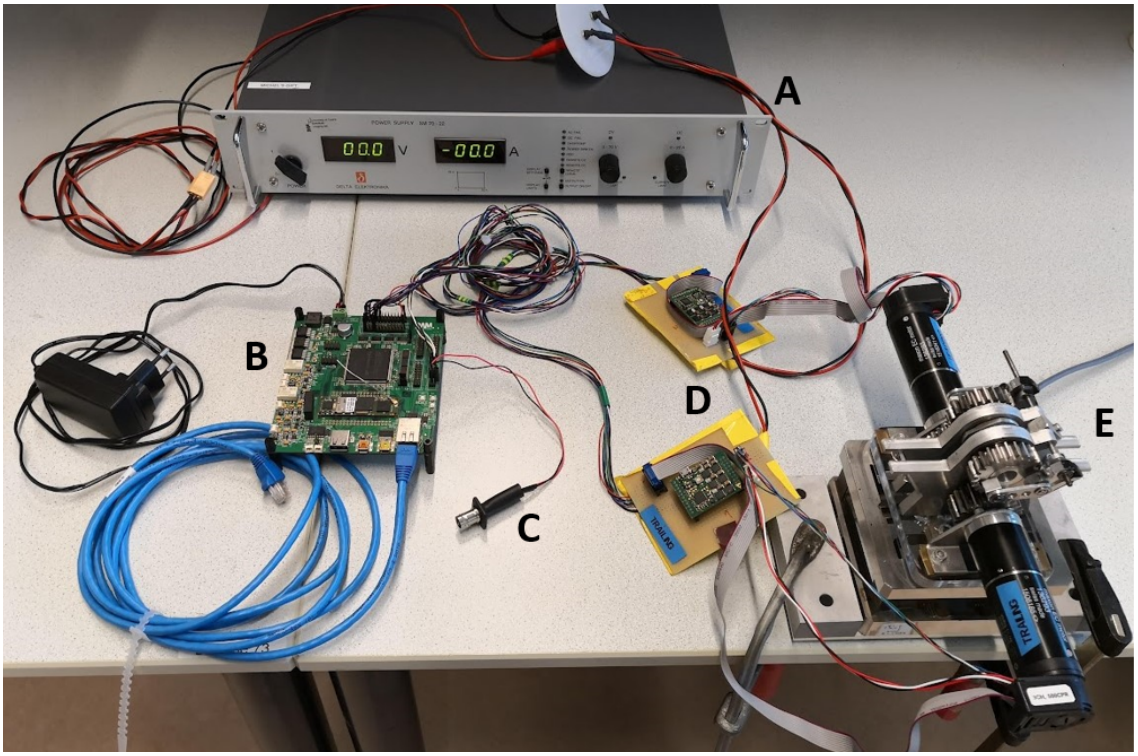

Figure 23: Flapping mechanism set-up

The RamStix circuit board is connected with a LAN cable to a laptop with 20-sim 4C, containing a programmed controller. This controller allows changing the flapping frequency and can start the flapping motion. The power supply was set to max 5.0A and 36V but uses the input flapping frequency to determine the actual voltage and current needed, as the voltage is directly proportional to f_{max}. It was found that the f_{max} of the flapping set-up with the wind on is $\approx 3Hz$, since higher frequencies result in an error, causing the motor drivers to be turned off. Note however that f_{max} is not the same for different wind speeds and different wings used. Increasing the maximum voltage does not change f_{max}, leading to the belief that the system is mechanically limited. Slow motion footage of flapping at f_{max} revealed slight bending of the flapping axle. This further backs the mechanical limitation claim, as these sub-optimal operating conditions can trigger a safety stop in the controlling software. Before the start of the experiments a calibration in 20-sim 4C was performed on the flapping mechanism with the wing placed in a fixed position ($\Phi = \Phi_{max}$ was selected), resulting in a trigger signal at a known Φ. For more information about the flapping set-up, the reader is referred to [Vaseur, 2014] and [Jongerius, 2017].

6.4 Force Balance

The force balance used is a custom-made half-model balance B20334 by Royal Netherlands Aerospace Centre (NLR). The balance is sensed in 3 directions as can be seen in table 4, and calibrated by NLR, resulting in the known root mean square errors of the measured forces or moment in every sensing direction. The balance is made as stiff as possible in the directions that are not sensed.

Component	Magnitude	RMS error (%)	Sensed
F_x (Axial force)	-30N / +30N	0.4	Yes
F_y (Side Force)	-30N / +30N	-	No
F_z (Normal Force)	-125N / +125N	0.02	Yes
M_x (Roll)	-37Nm / +37 Nm	-	No
M_y (Pitch)	-3Nm / + 3Nm	0.08	Yes
M_z (Yaw)	-3Nm / + 3Nm	-	No

Table 4: Load table and accuracies of half model force balance [Kasiemkhan and van Vilsteren, 2021].

The balance is placed in the wind tunnel in such a way that F_z is located in the lift direction and F_x in the thrust direction, as it's expected that the lift- and down forces will exceed the thrust- and drag forces. The flapping mechanism should not touch anything apart from the force balance when it's mounted in the wind tunnel, so both the force balance and flapping mechanism are mounted on a stiff structure bolted below the wind tunnel test section, as can be seen in Figure 24. The flapping mechanism was mounted slightly lower than for normal flapping wing measurements. This enabled the aerodynamic shell to be mounted flush with the wind tunnel without touching the flapping mechanism, resulting in a gap of $\pm\, 4mm$ with the flapping mechanism.

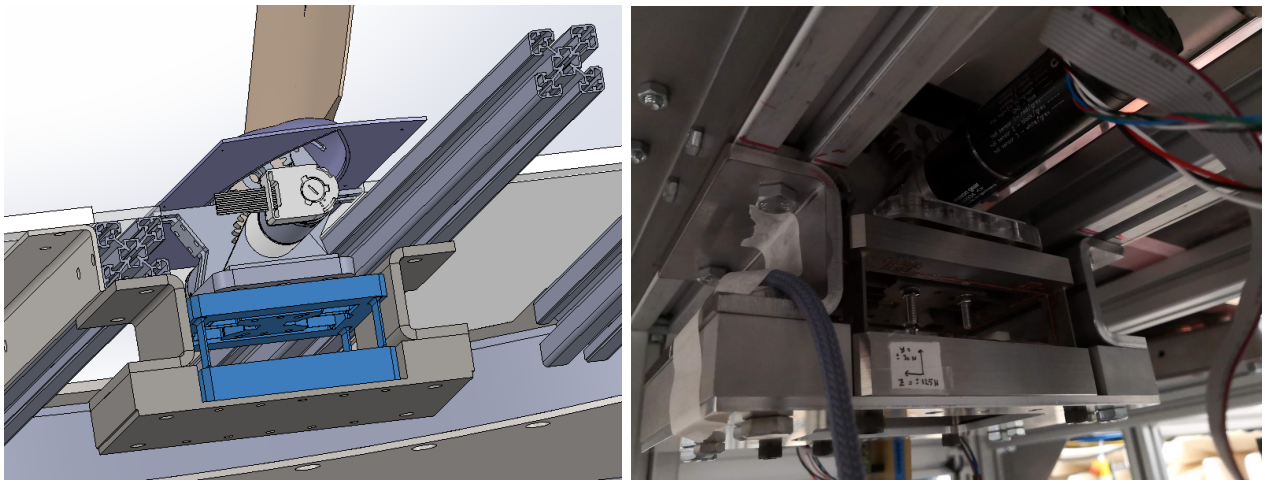

(a) Semi-cutaway view of force balance (blue) and flapping mechanism in wind tunnel

(b) Force balance and flapping mechanism mounted in wind tunnel

Figure 24

The measured force data and the trigger signal were collected by the NI DAQ 9174 Data Acquisition System, which can be seen in Figure 25. Different modules were connected to this chassis in order to convert the different analog signals into digital signals, which could be viewed and saved using NI Labview 2021 SP1. Force measurements were performed with a sampling frequency of $\pm$ 1610 Hz. Apart from the force- and trigger signals, the DAQ system was also used to convert data from the pitot tube and a thermocouple to a digital signal.

Figure 25: Data Acquisition System for force measurements

6.5 Wing Design and Production

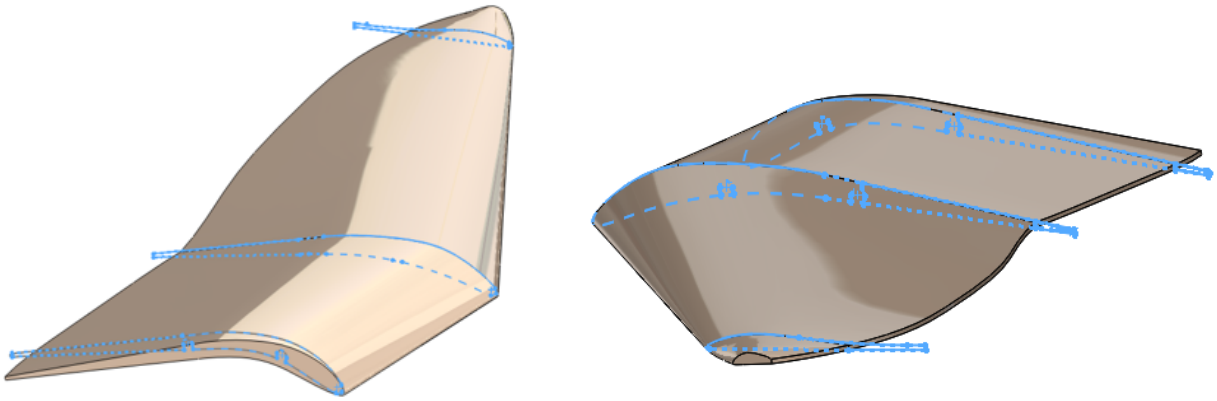

Figure 26: RoBird wing with three airfoils in blue

The RoBird wing is produced by using three distinct airfoils, as can be seen in Figure 26. In order to create wings with a sharp and blunt leading-edge, the airfoils of the original wings have been adapted. Figure 27 shows the middle airfoil as an example, where it can be seen that the blunt airfoils have been made by increasing the radius $\pm 3 - 4$ times, and the sharp airfoils by creating an angle of $\pm 75 - 80°$ while keeping the leading-edge on the camber line.

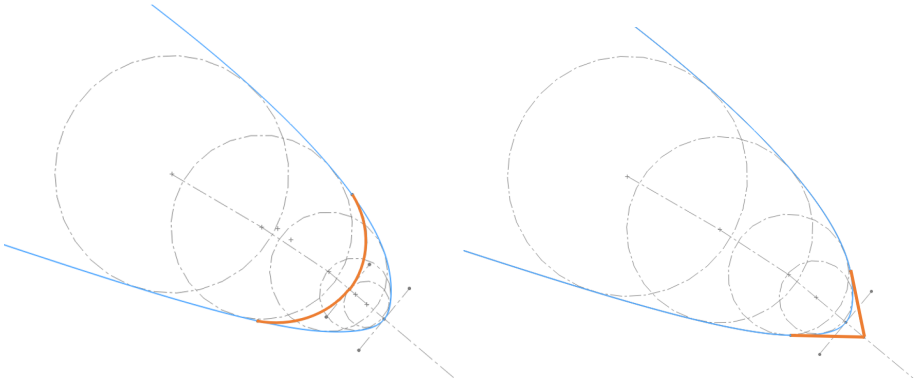

(a) Blunt airfoil design (orange) relative to original (blue) airfoil

(b) Sharp airfoil design (orange) relative to original (blue) airfoil

Figure 27

The RoBird wings are cut with a CUT 1610S CNC-hot wire foam cutter. This cutter works by creating a cutting path between two cutting profiles in two parallel planes. By using the three airfoils as cutting profiles, the hand- and armwing can be made separate from each other. The resulting arm- and hand wing leading-edges as produced by the foam cutter can be seen in Figure 28. A clear difference can be seen in the sharpness of the armwing leading-edges, but the same can not be said for the hand wings, which all look alike. No solution could be found in the cutting process of these highly swept wings. Therefore the leading-edges of the hand wings have been made sharp and blunt by post-processing the produced hand wings with a sanding machine. The sharpness and bluntness of the hand wings are therefore not clearly defined, but defined by 'eyeballing' and feeling the wings until they were deemed to match the original design well enough. Significant care has been taken to make sure the difference in sharpness between the different wings was large enough.

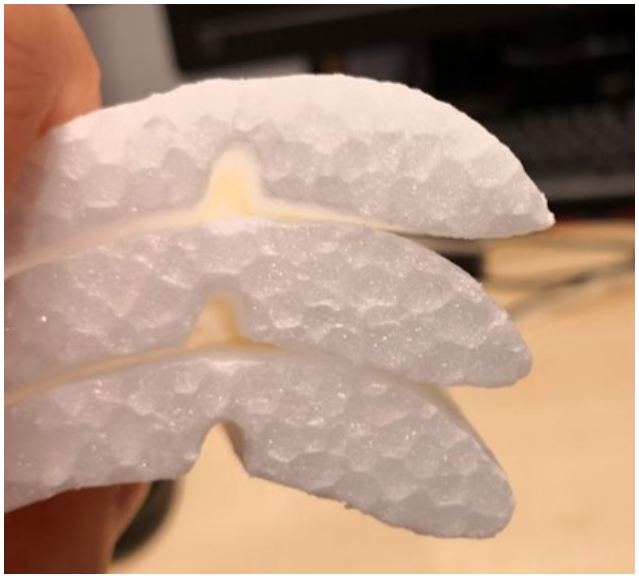

(a) Produced armwings with clear leading-edge differences

(b) Produced handwings with similar leading-edges

Figure 28

The arm- and handwings are glued together, after which they are suitable for cutting the feathers in the trailing edge. The wing spars and carbon reinforcement strip are then glued in place such that the glue changes the wing shape as little as possible. With the internals in place, the wing is coated and painted back, to minimize reflections coming from the laser, as can all be seen in Figure 29.

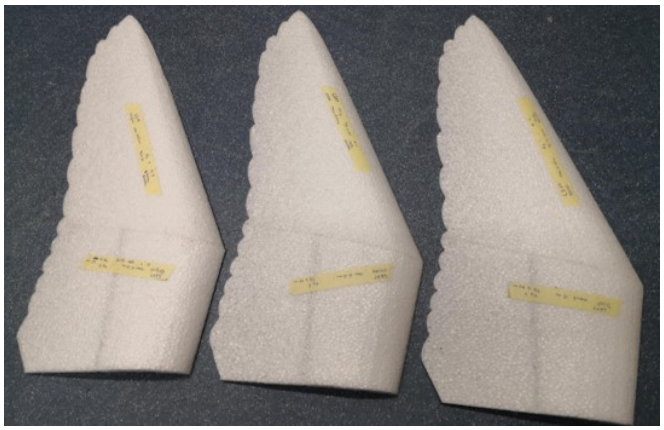

(a) Arm- and hand wings glued together

(b) Finished wings

Figure 29

7 Results

This chapter starts by analyzing the local dimensionless numbers, followed by the measurement results from the PTV and force balance measurements. A total of 90 measurement sequences have been performed. Half of these measurements were performed on the flow over the top of the wing, and the other half on the bottom flow. Of the 45 bottom- and top measurements, 16 were done for the blunt wing, 13 for the original wing, and 16 for the sharp wing. The lower amount of measurements for the original wing relative to the other two wings is due to the limitations of the flapping mechanism. If a certain frequency and flow velocity combination were too high for the flapping mechanism, the flow velocity and/or frequency was lowered such that a relatively high Reynolds- or Strouhal number was still possible. The measurement matrix in Figure 11 is therefore not always achieved, but the achieved measurement matrix per wing can be seen in Figure 30.

Re:	**55.100**	***63.000***	***70.900***	***74.500***	***78.800***	***84.100***	***86.600***	***98.500***	***106.400***
U_∞ [m/s]:	5,18	*5,92*	*6,66*	*7,00*	*7,40*	*7,90*	*8,14*	*9,25*	*9,99*
St: 0,20	B,O,S	B,O,S	B,O,S		B,O,S		B,O,S	B,O,S	B,S
St: 0,26	B,O,S	B,O,S	B,O,S	O	B,S	S	B		
St: 0,31	B,O,S								
St: 0,36	B,O,S								
St: 0,39	B,O,S								
St: 0,41	B,S								

Figure 30: Actual measurement matrix due to limitations in maximum flapping frequency. The letters indicate which of the Blunt, Original, and/or Sharp wings were used for a measurement with a specific setting.

The wing is mounted in the semi-open test section of the wind tunnel, with one of the sides being closed by a black cloth, as discussed in Chapters 6.1 and 6.2.2. Therefore, the top, bottom and one of the side walls have a no-slip condition and air can not pass through them. One of the sides is open, but contains a shear layer between the moving wind tunnel flow and the stationary air in the anechoic chamber. The measurements will therefore differ a bit from real life. A closed- or semi-open test section correction is typically applied for steady aerodynamics measurements, to correct for these wall effects, but no such corrections yet exist for unsteady flow in a semi-open test section. Therefore no attempt has been made to correct any of the results for the semi-open test section.

7.1 Local Dimensionless Numbers

Throughout the thesis, the average dimensionless numbers are used to describe the flow over the wing. It should be noted however that these average dimensionless numbers can vary quite drastically from the dimensionless numbers. For the Reynolds number, this is caused by variations of the chord length c along the wing span and variations in the effective flow velocity U_{eff} due to the flapping motion. Note that U_{eff} is dependent on Strouhal number, location on the wing, and on time.

Figure 31 shows the local Reynolds number as a percentage of the average Reynolds number at every location on the wing span for $\Phi = -19°$. This value of Φ is relevant for LEV formation, as will be discussed in Chapter 7.2, and has a relatively high wing velocity, resulting in a relatively high contribution of U_{eff} on the local Reynolds number. From this figure, it can be seen that especially at the low Strouhal numbers, the local Reynolds number is dominated by the varying chord length, and U_{eff} changes Re_{local} very minimal. For increasing Strouhal numbers the effect increases and appears to be maximal at a wing span of approximately 70 %, but its effect is still relatively modest compared to the varying chord length.

For constant Strouhal numbers, the effect of the local Reynolds number must be relatively small, as the relative difference between the different local and average Reynolds numbers must be the same. The absolute difference between different local and average Reynolds numbers does grow for larger and larger Reynolds numbers. This effect has been deemed negligible for the Reynolds region of this thesis though, as the selected Reynolds regime is relatively small.

There is a small difference in local Reynolds numbers for different Strouhal numbers, which should be kept in mind when analyzing the flow around flapping wings. For more information about the local Reynolds number and the calculations behind Figure 31, the reader is referred to appendix C.;

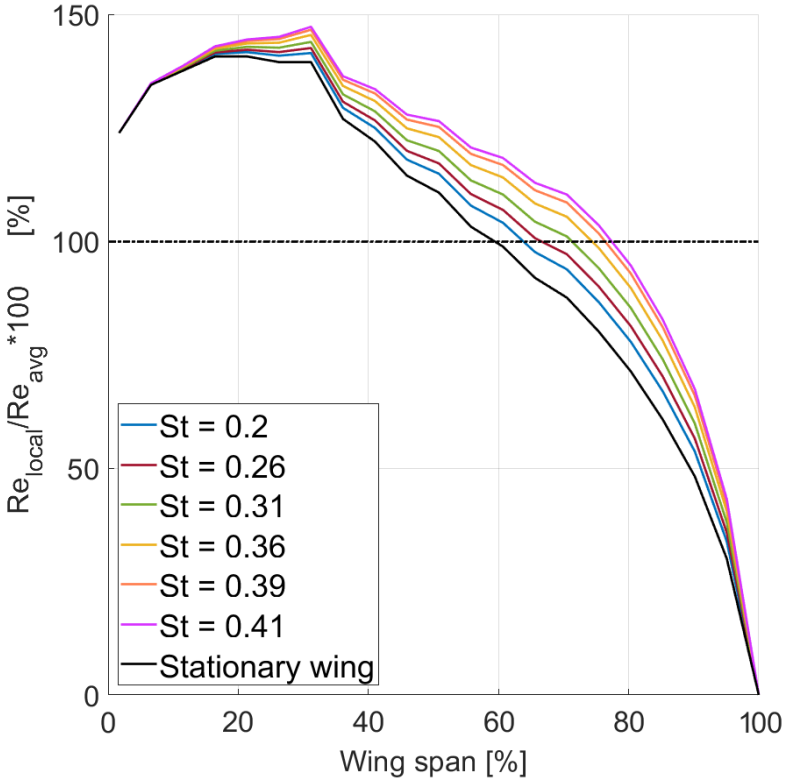

Figure 31: Local Reynolds number at $\Phi = -19°$ ($t/T = 0.91$) compared to the average Reynolds number. The stationary wing shows only the chord variation effect.

The local Rossby number is dependent on the Strouhal number, variations in wingspan when moving away from the rotational axis r, and the chord length c. These variations and the different Strouhal numbers used in the measurements have been applied to Equation 7, resulting in Figure 32.

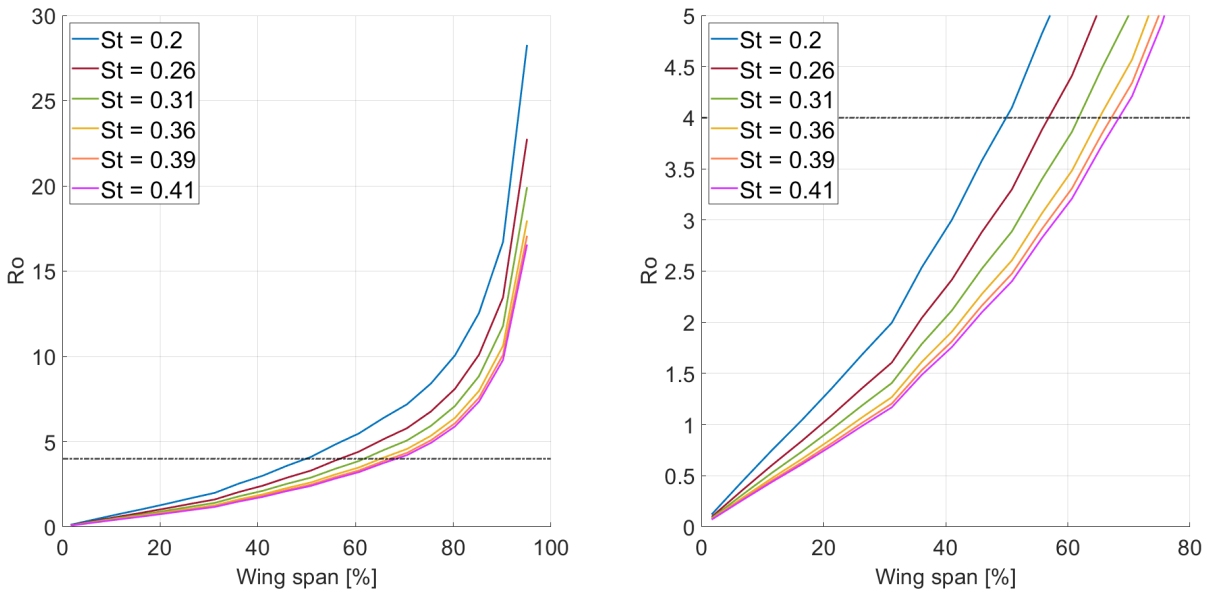

(a) Total Rossby regime

(b) Close up of Rossby regime for $Ro \leq 5$.

Figure 32: Local Rossby number over the RoBird's wing for different Strouhal numbers

As can be seen, the Rossby number remains relatively low for a relatively large percentage of the wing, after which it increases quickly when reaching the tip. When taking the $Ro = 4$ as the maximum value for the Rossby number where stable LEVs can form, it can be seen that stable LEVs can form up until a wing span of 50% for $St = 0.20$ and 68% for $St = 0.41$. Note however that while LEVs can be stable when keeping $Ro \leq 4$, they do not necessarily form. Especially very close to the root α_{eff} is very low, which often results in no formation of a LEV in that region. Also, LEVs can easily form for higher values than $Ro = 4$, but they will simply not be stable for these values of Ro.

7.2 Particle Tracking Velocimetry

Analyzing flow over both the top and bottom of the RoBird's wing was beyond the scope of the thesis due to the sheer amount of data gathered. Initial results of both the top and bottom flow indicated that no LEVs were present on the top of the wing during the downstroke and that they were present on the bottom side during the upstroke. Therefore the choice has been made to focus only on the flow over the bottom of the wing, and leave the data over the top of the wing for a future study.

A vortex structure was found in the particle tracks of 43 out of the 45 analyzed measurements. One of these measurements where the structure was very clear was at $Re = 55.100$ and $St = 0.36$, which is shown in Figure 34 as an example. The structure starts at approximately 40 % of the wing span at the beginning of the hand wing and starts rolling up into a seeming vortex at approximately 50 % of the chord. The structure seems to stop at approximately 75 % of the wing span, although it might also be possible that the particles reach the border of what the cameras can detect and can therefore not be tracked anymore. The values of Φ corresponding to the vortex development correspond very well to the lowest values of the effective angle of attack, as can be seen in Figure 33.

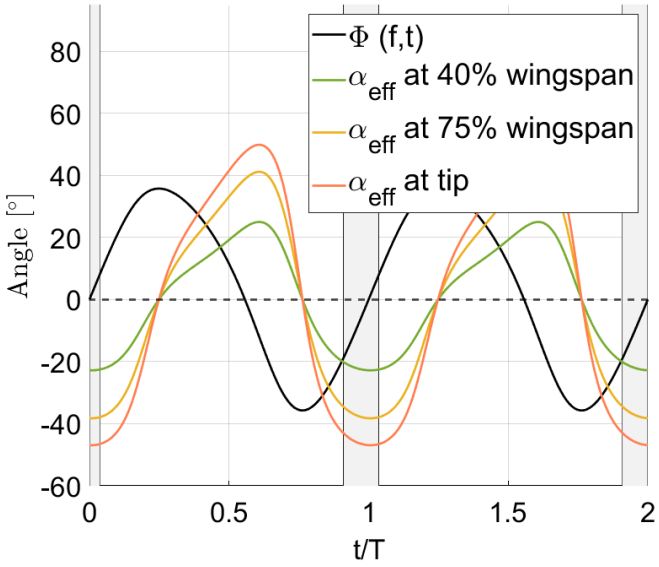

Figure 33: α_{eff} at different locations on the wing for $St = 0.36$ and $Re = 51.100$. The grey regions indicate the region where LEVs approximately form.

The height and width of the structure are more or less equal to each other, matching one of the criteria as discussed in Chapter 4.5. The flow inside the vortex has a high velocity towards the wing tip as can be seen from selecting U_y for the color scheme. This spanwise flow corresponds to the vortex stabilization mechanism as discussed in Chapter 4.4. When selecting U_x for the color scheme, as can be seen in Figure 35, it can be seen that a clear reversed flow is present in the vortex, matching one of the LEV criteria as mentioned in Chapter 4.5. Note that the high velocities observed are not a variation of the uniform flow, as one would typically see for a steady flow, but seem to be added to the flow by the moving wing. This indicates that the kinetic energy of the moving wing is fed into the flow.

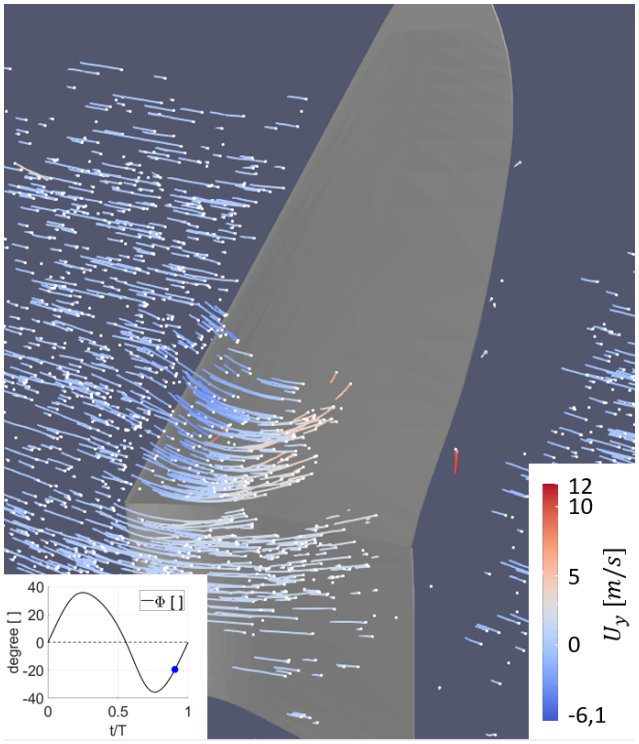

(a) Vortex starts rolling up at $\Phi \approx -19°$ ($t/T = 0.91$)

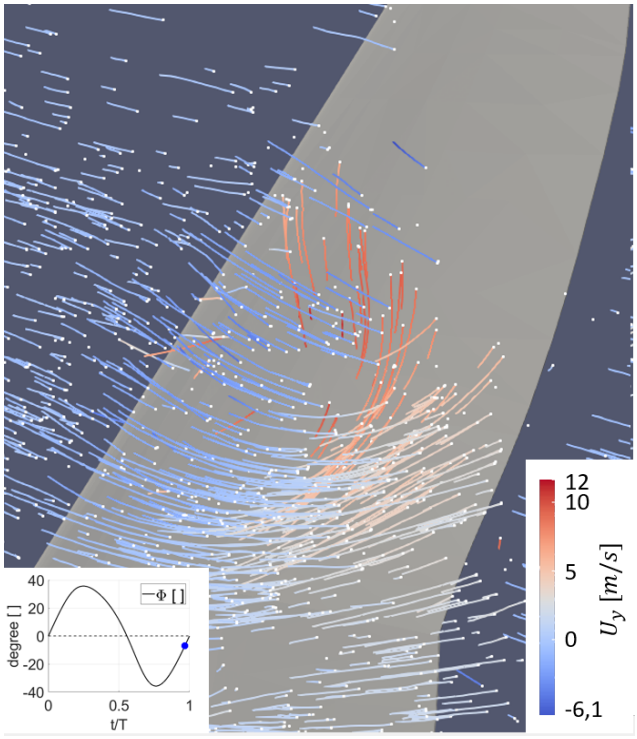

(b) Vortex approximately at max strength at $\Phi \approx -7°$ ($t/T = 0.97$)

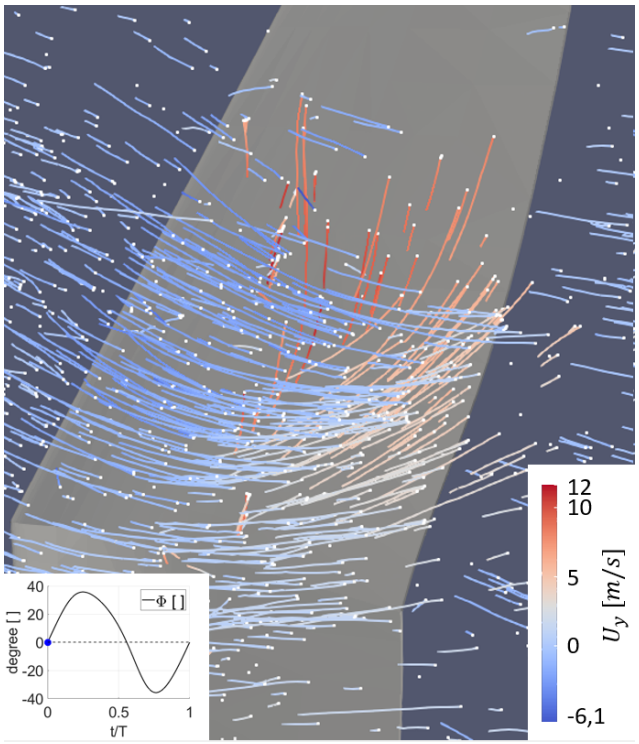

(c) Vortex moves to back of the wing at $\Phi \approx 0°$ ($t/T = 0$)

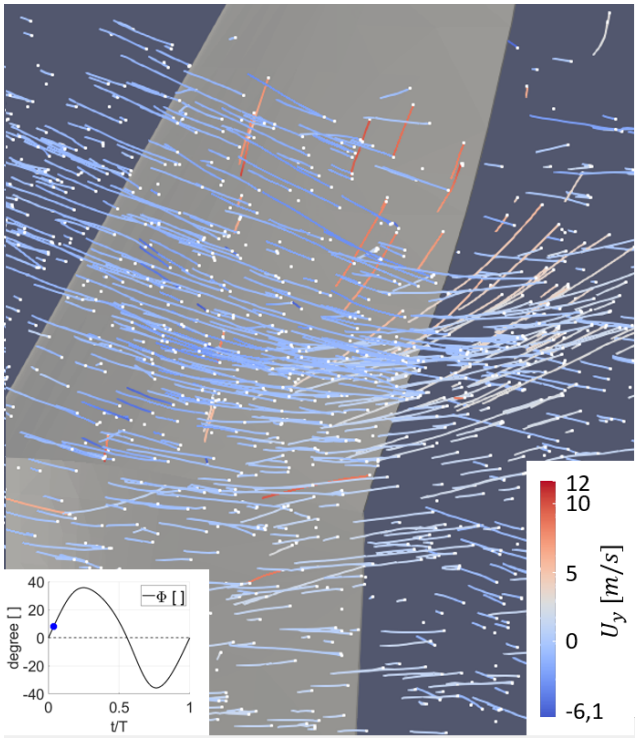

(d) Vortex is shed at $\Phi \approx 8°$ ($t/T = 0.04$)

Figure 34: Vortex formation on sharp wing at $Re = 55.100$ and $St = 0.36$. U_y is selected for the color scheme.

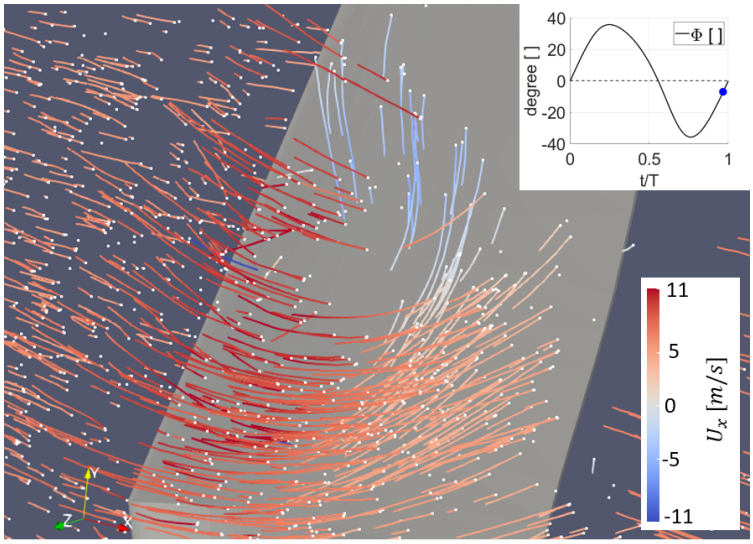

Figure 35: Vortex on sharp wing at $Re = 55.100$ and $St = 0.36$ at $\Phi \approx -7°$. U_x is selected for the color scheme.

One of the measurements where no leading-edge vortex was found was on a blunt wing at $Re = 55.100$ and $St = 0.20$, which can be seen in Figure 36. When comparing the results of Figure 34 and 35 to these measurements, clear differences can be seen. No clear region of vortex roll-up is visible, although the flow tends to curve a bit toward the tip. At the wing position where the strongest vortex was observed for the $St = 0.36$ case, no particle tracks at all are visible that indicate any vortex presence.

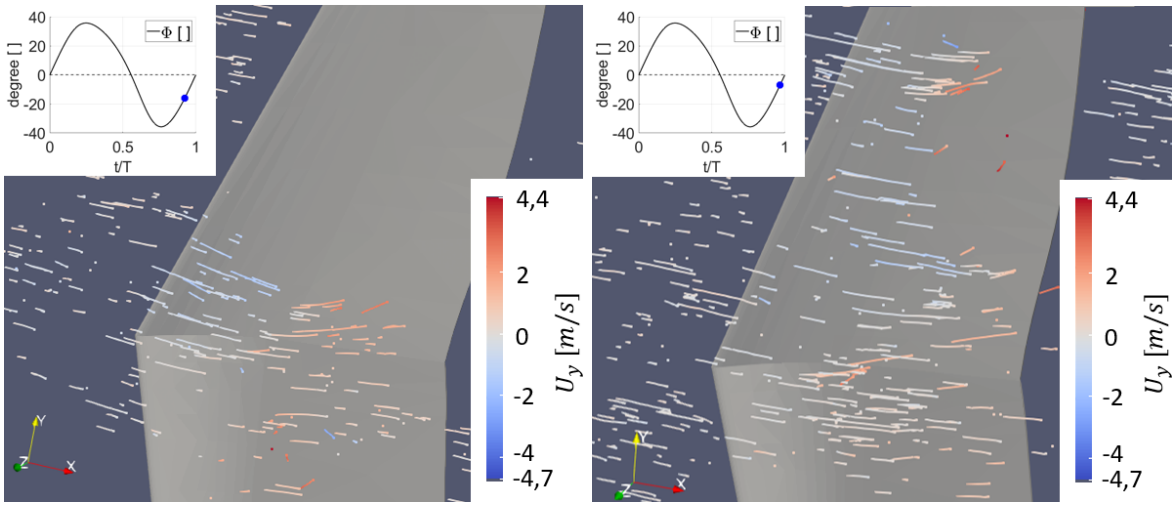

(a) No vortex roll up at $\Phi \approx -16°$ ($t/T = 0.92$)

(b) No clear horizontal tracks visible at $\Phi \approx -7°$ ($t/T = 0.97$)

Figure 36: Flow over blunt wing at $Re = 55.100$ and $St = 0.20$. U_y is selected for the color scheme.

When performing simulations or measurements, vortex identification is typically done with the use of for example vorticity, the Γ_1 or Γ_2 functions, or the Q-criterion [Eldredge and Jones, 2019]. With vorticity data available it would theoretically be possible to distinguish vorticity in the structure's core and the lambda-shaped region of counter-rotating vorticity upstream of the vortex structure as discussed in Chapter 4.5. This would result in more certainty about the vortex structure being a leading-edge vortex. Applying such methods requires a vector field of the flow though, which requires binning of the particle tracking data. This is possible with the available data and DaVis 10.2.1 software, but due to the large amount of data and limited processing power available, this was deemed to be out of the scope of the thesis. The structure forms relatively close behind the leading-edge, the height and width of the structure are more or less equal, and a clear reversed and spanwise flow is observed. Therefore, it's deemed highly likely that the observed structure is indeed a leading-edge vortex.

From the local Rossby analysis in Chapter 7.1 it becomes clear that formed LEVs can only be stable up from the root until approximately 50% to 68% of the wingspan, depending on the Strouhal number of the measurement. As can be seen in Figure 34, the vortex does seem to move to the back of the wing, where it is shed in the wake, indicating that the vortices are unstable. Given that the LEV appears at approximately 40% to somewhere between 70 and 80% indicates that the LEVs form precisely in the overlapping region where they can and can't be stable.

7.2.1 Quantifying Vortex Strength

In order to answer the research questions regarding the influence of leading-edge radius, Reynolds- and Strouhal number on LEV formation, it is desired to say something more about the vortex than 'it's there', or 'it's not there'. In order to do so, an attempt has been made to quantify the vortex strength with the particle tracks. For the color scheme, DaVis 10.2.1 allows selecting the flow velocities and accelerations in x, y, and z direction and the absolute velocity and acceleration. From these options, the velocity in the y direction inside the vortex could be distinguished the most reliably for all the different measurements. As discussed in Chapter 4.4, spanwise flow inside a LEV is key in stabilizing the vortex, so for now, the assumption is made that the maximum value of U_y inside the vortex, is representative of its strength. Therefore for all the measurements where a vortex was found, the maximum U_y inside each vortex has been noted.

Figure 37 shows the resulting U_y for the three different leading-edge shapes at $St = 0.20$ and 0.26 for $55.1000 \leq Re \leq 106.400$. As can be seen, for $St = 0.26$, the measured U_y for each wing is always higher than for $St = 0.20$. Only the original wing has a higher U_y than the sharp wing at $Re = 70.900$ while being at a lower Strouhal number, but this will be discussed in Chapter 8.4. Also, for increasing Reynolds numbers, there is a clear trend visible that U_y also increases. This can however also be explained by the increasing velocity U_∞ as the Reynolds number is increased, which automatically increases velocities in other directions. Therefore the non-dimensional U_y/U_∞ will be used from now on to compare the relative vortex strength with each other. The resulting graphs with varying Strouhal numbers and varying Reynolds numbers can be seen in respective Figures 38a and 38b.

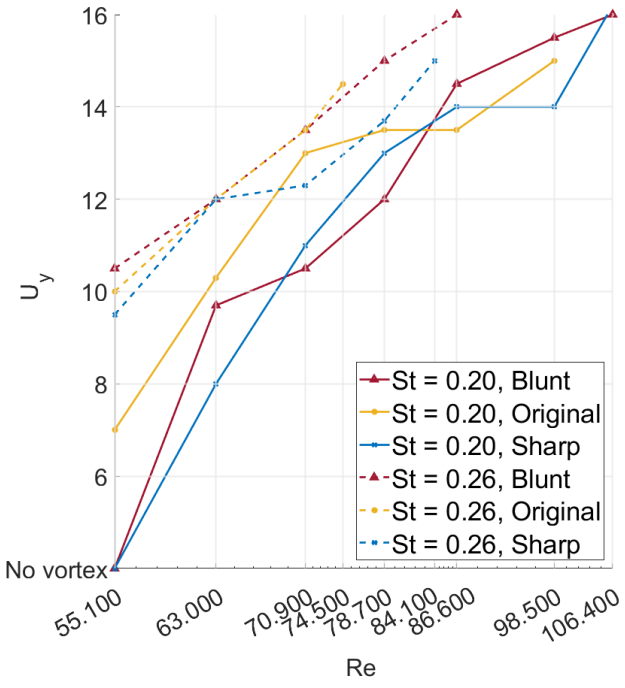

Figure 37: Maximum values of U_y inside LEV for three different leading-edge shapes at $St = 0.20$ and $St = 0.26$ for $55.100 \leq Re \leq 106.400$.

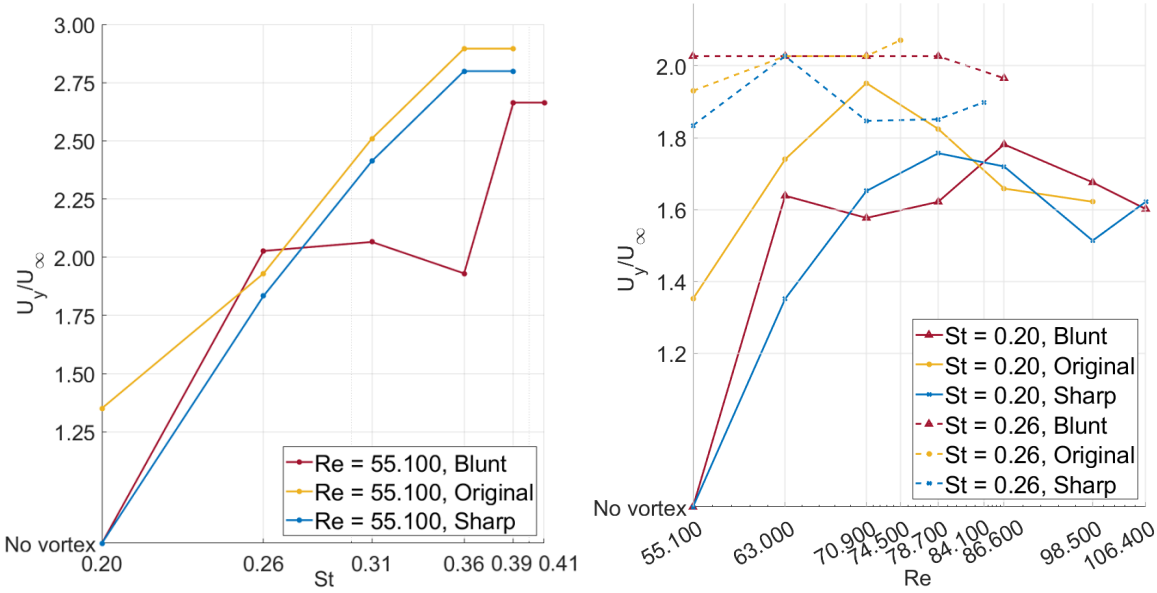

(a) Maximum values of U_y/U_∞ inside LEV for three different leading-edge shapes at $Re = 55.100$ for $0.20 \leq St \leq 0.41$.

(b) Maximum values of U_y/U_∞ inside LEV for three different leading-edge shapes at $St = 0.20$ and $St = 0.26$ for $55.100 \leq St \leq 106.400$.

Figure 38

7.2.2 Strouhal Effect

When looking at the graphs of U_y/U_∞ of the three different wings for a constant $Re = 55.100$ and $0.20 \leq St \leq 0.41$ in Figure 38a, the influence of the Strouhal number can clearly be seen. Note that due to the constant Reynolds number, the velocity U_∞ is constant for all the data. This indicates that U_y is not (only) dependent on U_∞. At $St = 0.20$ the sharp and blunt wings do not seem to develop a LEV, while the original wing develops a relatively weak LEV. The original and sharp wing show a clear trend upwards in vortex strength as St increases, with a possible limit to the vortex growth for the highest Strouhal numbers. The blunt wing also roughly follows this trend, but a clear difference can be seen at $St = 0.31$ and $St = 0.36$, where the growth of vortex strength seems to be stopped. For $St \geq 0.39$ the vortex strength seems to have more or less matched the trend of the blunt and sharp wing again by increasing in strength drastically and flattening off the growth at the highest Strouhal number. From Figure 38b it can be seen that for the entire investigated Reynolds range the vortex strength is higher at $St = 0.26$ than at $St = 0.20$. Only the mentioned original wing at $Re = 70.900$ is an exemption, as will be further discussed in Chapter 8.4.

7.2.3 Reynolds Effect

When plotting U_y/U_∞ for $55.100 \leq St \leq 106.400$ at $St = 0.20$ and $St = 0.26$ as is shown in Figure 38b, the clear upward trend that was seen in Figure 37 when plotting U_y only is not visible anymore. Instead, a more parabola-like shape can be seen for the data at $St = 0.20$. At $Re = 55.100$ the same can be observed as in Figure 38a: At $St = 0.20$ the sharp and blunt wings do not seem to develop a LEV, while the original wing develops a relatively weak LEV. For all the higher Reynolds numbers at $St = 0.20$ a leading-edge vortex does form, increasing in strength until a peak is reached at $Re = 70.900$ for the original wing, $Re = 78.700$ for the sharp wing and $Re = 86.600$ for the blunt wing. After the peak the vortex strength decreases for all three wings, indicating that some sort of optimum has been reached for vortex formation. As discussed in Chapter 7.2.2, the measurements at $St = 0.26$ all have a higher vortex strength than their respective measurement at the same Reynolds number and $St = 0.20$, with the exemption of only one measurement. The parabola-like shape as observed for $St = 0.20$ can not be distinguished anymore though, as the lines look more or less constant as the Reynolds number increases, indicating a decreased Reynolds dependency for increased Strouhal numbers.

The blunt wing is again a bit of an outlier compared to the other two wings. For the original and sharp wings U_y/U_∞ increases steadily at $St = 0.20$ until the peak is reached, after which a steady decrease in U_y/U_∞ is observed. The blunt wing however has a relatively high vortex strength at $Re = 63.000$ after which a dip in vortex strength is observed for $Re = 70.900$ and $Re = 78.700$, followed by the peak strength at $Re = 86.600$.

7.2.4 Leading-Edge Shape

When looking at Figures 38a and 38b it can be seen that there are differences in vortex development for different leading-edge shapes. The original wing seems to be most prone to vortex development. It is the only wing to develop a vortex at $St = 0.20$ and $Re = 55.100$, and the measured U_y/U_∞ is larger than for the other two the wings for a large percentage of the measurements. All three wings peak with a different magnitude at a slightly different Reynolds region for $St = 0.20$, indicating that optimal vortex formation is not only Reynolds number, but also leading-edge dependent. And interestingly, the blunt wing has 'dips' in the data where it deviates from the trends that can be seen for the original and sharp wing. At $St = 0.26$ the blunt and original wings create a more or equal vortex strength, but the sharp wing has a lower vortex strength, despite following more or less the same constant trend as the Reynolds number increased.

7.3 Force Measurements

Throughout this chapter, a measurement with a sharp wing at $Re = 55.100$ and $St = 0.39$ will be used as an example of how the data is processed. The force data of the other measurements looks very similar, and processing that data gives very similar results.

7.3.1 Raw Data

The raw data is not yet suitable for analysis. As can be seen in Figure 39, it is very noisy and it contains data from before and after the flapping sequence. The data is also not yet linked to a certain timestamp, instead, it is linked to a sample number.

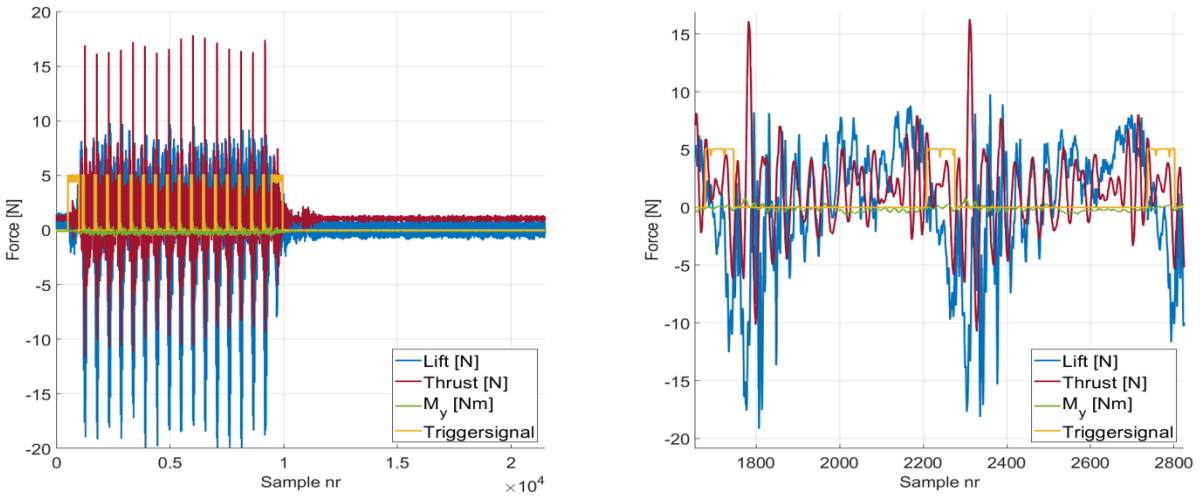

(a) Entire data set of single measurement

(b) Zoomed in on approximately two flapping cycles

Figure 39: Raw force data example of sharp wing, $Re = 55.100$ and $St = 0.39$

Therefore the data first needs to be linked to a timestamp and excess data needs to be cut off. This is done using the trigger signal, which gives a pulse precisely when the wing passes through a reference position ($\Phi = \Phi_{\max}$). The first and last cycles have also been cut off from the data, as they differ from the other cycles due to the start-up and slowing down of the flapping mechanism. The input frequency is known, so the time between two pulses is therefore also known. This allows for coupling a certain time stamp to a given sample number. This was done such that $t = 0$ was linked to $\Phi = 0$ during the upstroke, which is the actual start of the flapping cycle, as defined in Chapter 3.2. The number of samples between the pulses have been checked to make sure that the cycle length is the same for all the measured cycles, and no noteworthy differences over cycles have been observed. During some measurements, a single trigger signal was sometimes not registered. When this happened, the cycle before and after the (missing) trigger signal was not used for further analysis, as it was not sure where the cycle started and ended. The data can be plotted using the non-dimensional time t/T, resulting in data as can be seen in Figure 40.

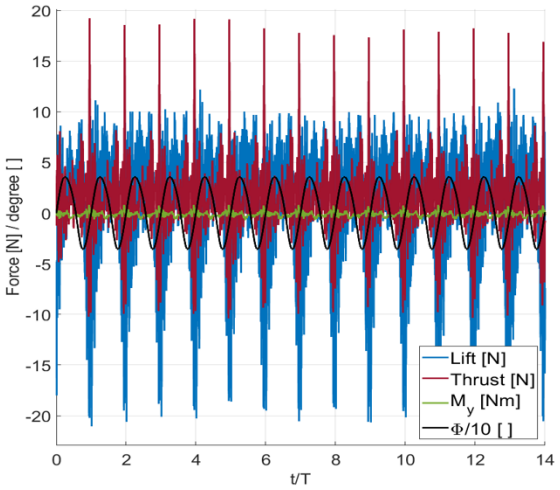

(a) Entire data set of single measurement

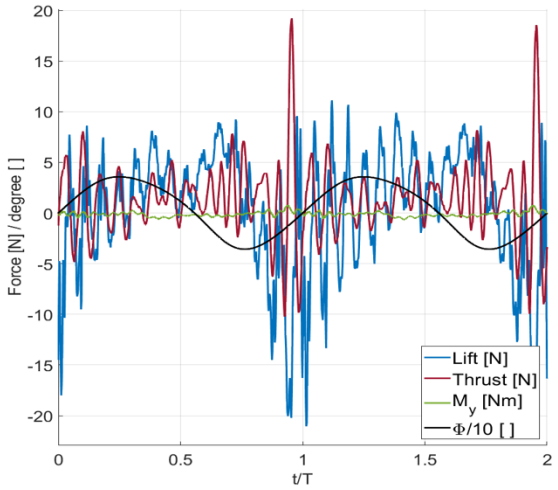

(b) Zoomed in on two flapping cycles

Figure 40: Semi-raw force data example of sharp wing, $Re = 55.100$ and $St = 0.39$

7.3.2 Low Frequency Filtering

When one wants to filter out high-frequency noise, it is first useful to understand the possible source of this noise, so that one is sure that no useful data is filtered out. A signal frequency domain analysis on the useful raw data revealed that a lot of noisy data is present at $f \approx 40 - 50\,Hz$ and a (crude) eigenfrequency analysis in SolidWorks revealed that the first eigenfrequency of the force balance with flapping mechanism mounted on it, is also located at $f \approx 50\,Hz$. Details of both analyses can be found in Appendix E, but due to these findings, it's expected that a large portion of the noise is caused by eigenfrequencies in the force balance. Therefore the cutoff frequency selected for processing the force data is $f = 30\,Hz$, as it is located far enough from the noise, while as much as possible information about the forces acting on the wing is preserved. The data of M_y has been used in the frequency domain analysis to detect possible frequency peaks which cause noise but has been ignored for the rest of the thesis, as lift and thrust forces are deemed more relevant and could therefore be given more attention.

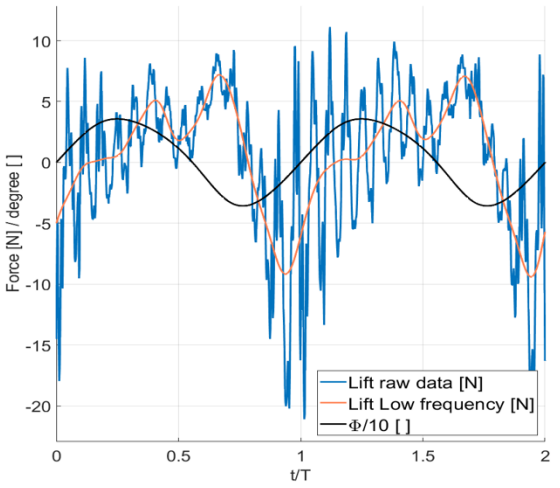

(a) Lift

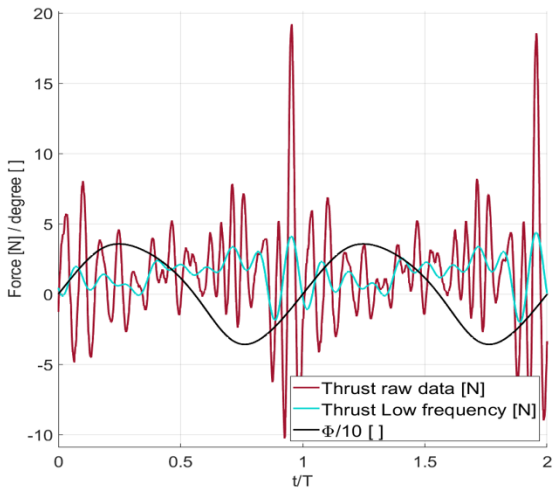

(b) Thrust

Figure 41: Raw force data compared to the low-frequency filtered data. Example of sharp wing, $Re = 55.100$ and $St = 0.39$

The result of the low-frequency filter can be seen in Figure 41 for both the lift and drag. Especially for the lift forces a lot of the noise is filtered out, leaving a relatively clean periodic signal over the wing beat cycle. For thrust also a lot of the noise is removed, but a periodic signal is less easy to spot. The low-frequency data is then used to create the average low-frequency lift- and drag force over one cycle, which can be seen in Figure 42. These low-frequency filtered and averaged forces can then be used to compare forces from different measurements. Note that from now on the approximate region of LEV development as discussed in Chapter 7.2 is highlighted by the grey area.

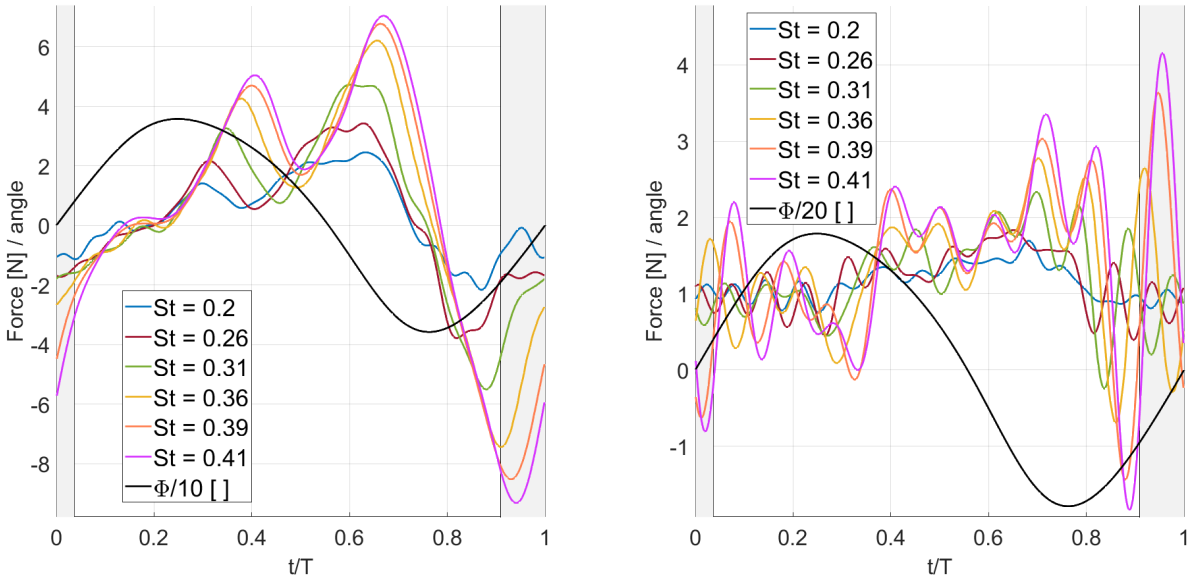

(a) Lift

(b) Thrust

Figure 42: Comparison of single cycle averaged and filtered data. Example of sharp wing, $Re = 55.100$ and $0.20 \leq St \leq 0.41$

7.3.3 Aerodynamic Forces

The forces as shown in Figure 40 to 42 are not only the aerodynamic forces but also inertial forces acting on the flapping mechanism. Changing flow velocities, flapping frequencies or the wing used will therefore always result in different measured forces, which makes the comparison of data very hard. In order to separate inertial- and aerodynamic forces, all the force measurements have been done twice: Once with wind and once without wind. Subtracting the filtered and averaged data of both measurements should in theory cancel out the inertial forces and leave only the aerodynamic forces acting on the wing. This is per definition false, as aerodynamic forces are also acting on the wing without wind and for example bending and twisting of the wing without wind is different, which changes the inertial forces. It is however expected that the error introduced is still acceptable and that the result should be suitable for examination of aerodynamic forces acting on the wing. On top of that, there are not any other suitable options to obtain aerodynamic forces from the force data. Therefore the mentioned method of obtaining aerodynamic forces is used for all further analyses. As can be seen in Figure 43, the resulting aerodynamic forces look more chaotic than the previous plots. Despite this, a periodic signal is visible for all the shown Strouhal numbers, indicating that the method to obtain aerodynamic forces works. The chaotic data could be optimized by further tweaking the cutoff frequency, or by applying another filter on the aerodynamic force data. But before processing the data further, it is important to understand the reliability of the data better, to answer the research question "Can force measurements with a half-model balance reliably be used to determine lift and drag forces acting on the RoBird's flapping wing in a wind tunnel".

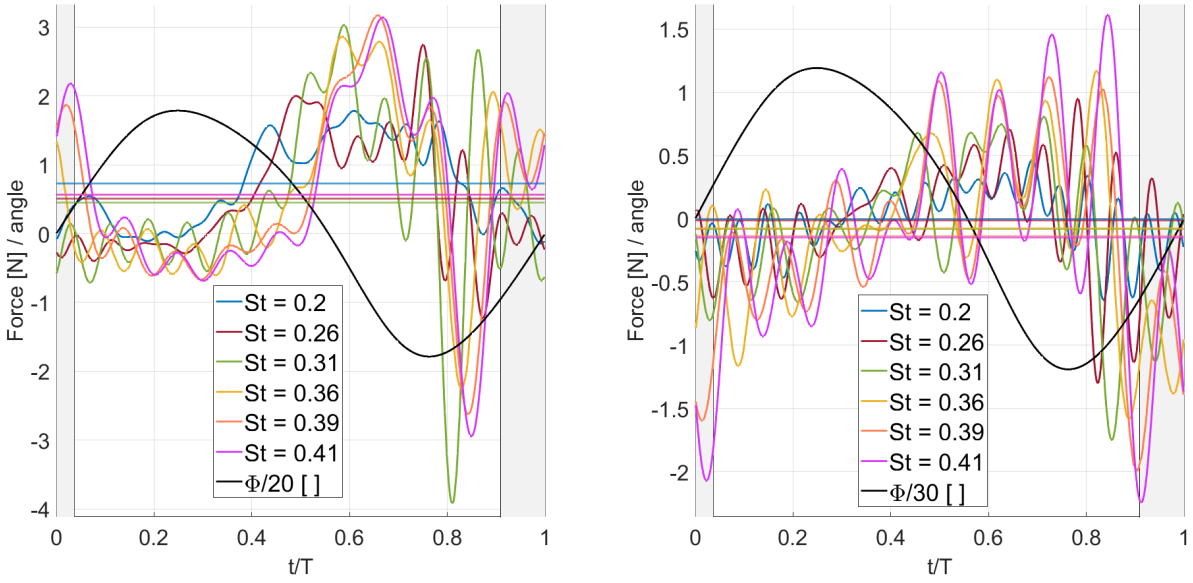

(a) Lift

(b) Thrust

Figure 43: Comparison of aerodynamic forces with average force as horizontal line. Example of sharp wing, $Re = 55.100$ and $0.20 \leq St \leq 0.41$

Appendix F contains similar graphs to Figure 43 for the sharp wing, but then for constant $St = 0.20$ and $St = 0.26$ for varying Reynolds numbers. Similar graphs have been made for the other wings, but due to their similarities, they don't contribute to the discussion and conclusions of the thesis and have therefore been left out of the appendix .

7.3.4 Data Reliability

As mentioned earlier, the PTV measurements have been performed twice: once to measure the flow on the top of the wing, and once to measure the flow on the bottom of the wing. The only change that was made to perform these different measurements was placing the camera set-up and laser on the opposite side of the wind tunnel, but the flapping mechanism and force balance were not changed at all. The force measurements have been performed every time a PTV measurement was performed, meaning that all the force data exists twice and should theoretically be equal. By processing both data sets and comparing the average aerodynamic forces, both data sets can be checked if they differ too much from each other. Figure 44 contains some examples of the average lift and thrust forces acting on the different wings during flapping. As can be seen, there are large differences between the top flow measurements (solid line) and the bottom flow measurements (dashed line). There are not only large differences in force magnitudes but even in the direction. A clear example is the lift acting on a blunt wing at $St = 0.20$. The top measurement produces downforce, while the bottom measurement produces lift, both with quite different magnitudes. As the Reynolds number increases, the magnitudes only increase for both magnitudes, which results in an opposite Reynolds dependent trend. Appendix G shows all the resulting average force data for all the performed measurements. Also, note that the magnitudes of the average forces measured are all way too small to keep the RoBird in level flight.

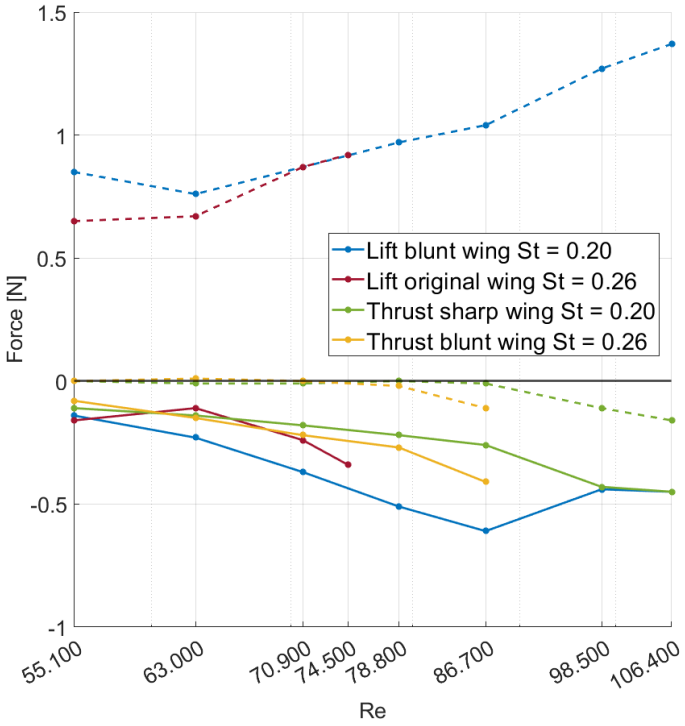

Figure 44: Example of average aerodynamic lift or drag forces acting on wings during both top measurement (solid line) and bottom measurements (dashed line).

Due to the large differences, the data is deemed unreliable, and therefore no attempt has been made to apply further filters to the aerodynamic data to check for LEV effects in the data. There do not seem to be any clear trends in the region where LEVs form, but even if there would be a trend, it is highly questionable if these results can be trusted, as the average force comparison clearly indicates that something has gone wrong and the results are not reliable.

8 Discussion

This chapter discusses the results from Chapter 7. It starts by analyzing the possible errors in the particle track analysis, which is needed to correctly interpret the PTV data. With this knowledge, the effects of the Reynolds- and Strouhal number and the leading-edge radius are compared to the hypothesis, and the reasons behind possible deviations are discussed. At last, the possible reason behind the unreliable force data is discussed.

8.1 Errors in Particle Track Analysis

Analyzing the flow around the RoBird's wing with particle tracks only is highly error-sensitive. Ghost particles, which are artifacts of the reconstruction process, do not really represent a bubble trajectory, and are often present in the data, even after applying filters to the maximum accelerations, U_x and U_y. These ghost particles can make it very hard to judge whether or not a track actually indicates a bubble trajectory. The vortex that was shown in Figures 34 and 35, shows one of the clearest examples of a vortex that was found with a lot of particle tracks showing the vortex. For some of the measurements, the vortex was not at all so clear though. Some measurements resulted in a lot of particle tracks, while other measurements resulted in relatively few, resulting in less information to work with to interpret the flow. Especially in cases with relatively few particle tracks, a ghost particle traveling towards the tip in the region where one would expect a LEV can therefore be mistaken for a vortex. The other way around is also a problem. Due to the presence of ghost particles, one is skeptical about single particles in the region where one expects a vortex since they could be ghost particles. When a track is genuinely a particle track, it could be interpreted as a ghost particle and ignored, which could be the difference between a vortex being spotted or not being spotted.

Determining the precise value of Φ corresponding to certain stages of vortex development is also a relatively inaccurate process. It is prone to human interpretation of when a vortex starts and ends and is error sensitive due to the possible faulty placement of the wing relative to the particles. Checking for variation in the values of Φ corresponding to vortex development and breakdown is a lot of work and this information is relatively unimportant for answering the research questions. Therefore no attempt has been made to check for whether there is variation in the values of Φ corresponding to vortex development and breakdown over different measurements. The region of vortex development corresponds well to the lowest effective angles of attack though, indicating that the method of detection is good enough for the purpose of this thesis.

Determining the maximum value of U_y is also quite error-sensitive. Human interpretation of the flow influences what is and isn't seen as a vortex, and what is and isn't seen as a ghost particle. The noted values of U_y should therefore be taken with a large grain of salt. From Figure 38a, which shows U_y/U_∞ for varying Strouhal numbers and a constant Reynolds number, it could be concluded that U_y is not (only) dependent on U_∞. The assumption that U_y does represent vortex strength, therefore, seems to be justified.

Determining whether or not a LEV is unstable and/or detached can best be done with for example the vorticity, as an increase in vorticity should be observed for unstable LEVs. This was not available, so the stability can only be analyzed with the particle tracks. No suitable method could be discovered to quantify the stability, as the precise timescales and dimensions associated with the shedding of LEVs were almost impossible to capture accurately. On top of that, it would take a lot of time to analyze this for all the data. Therefore, the particle tracks have not been further investigated for vortex stability and the effect of the Rossby number.

8.2 Reynolds effect

The observed peak in vortex strength at $70.900 \leq Re \leq 86.600$ and $St = 0.20$ is located slightly before the $Re \approx 100.000$ mark that was found by [Ramesh et al., 2012]. This peak was discovered using very large steps for the Reynolds numbers though (..., 10.000, 50.000, 100.000, 500.000, ...), so finding a peak at a value relative close to $Re = 100.000$ is therefore believed to be in line with the findings of Ramesh et al.. A possible explanation for the decreased Reynolds dependency at $St = 0.26$ is that the higher effective angles of attack associated with higher Strouhal numbers become the dominant feature over LEV formation, decreasing the importance of the Reynolds number. Note however that the relatively few amounts of data points at $St = 0.26$ make it hard to make any definite statements about the influence of the Reynolds number on higher Strouhal numbers.

It is unclear why the blunt wing again has a dip in vortex strength in the plots of varying Reynolds number in Figure 38b, while the original and sharp wing seem to follow a relatively similar trend. The sharp wing seems to behave a bit differently than the blunt and original wings at $St = 0.26$, as it seems to remain relatively constant, but with a lower vortex strength than the other two wings. Again, the relatively few amounts of data points at $St = 0.26$ make it hard to make any definite statements about this observation however.

There are clear differences between the average and local Reynolds numbers, which could help explain why the LEVs develop as they do. The differences in local Reynolds numbers over different measurements are very small however for low Strouhal measurements, and practically negligible for constant Strouhal numbers, as explained in Chapter 7.1. The local Reynolds numbers are therefore not a sufficient explanation for the differences in vortex formation for different average Reynolds numbers, which therefore must be caused by the average Reynolds number itself.

8.3 Strouhal effect

It is not clear what may have caused the dip in the data of the blunt wing in the graph for the plots of constant Reynolds number and varying Strouhal number in Figure 38a. Overall the measured data the blunt wing follows the global trend that a higher Strouhal number results in a stronger vortex, but the local dip is contradicting the hypothesis about the Strouhal effect and does not match the clear trend seen for the sharp and original wing. It might have been caused by the failure of finding any fast-moving particle tracks inside the core of the vortex or by the rather crude technique to determine U_y. However, when considering that not one but two measurements are different than expected, the chance of a random error decreases.

Local Reynolds numbers do change when the wing flaps at different Strouhal numbers, as explained in Chapter 7.1. It's therefore also possible that some of the observed effects can be attributed to the differences in the local Reynolds number caused by changing the Strouhal number. It's however not believed that the local Reynolds number changes the vortex strength this much, as it's deemed more likely that the high effective angles of attack associated with high Strouhal numbers change the vortex strength a lot.

8.4 Leading-edge Shape

The relatively large vortex strength of the original wing for all performed measurements and the relatively weak vortices produced by the sharp wing are unexpected results. Almost none of the observations regarding wing shape match the hypothesis that the sharper a wing is, the more prone it is to develop a leading-edge vortex. Only the 'dips' in the data of the blunt wing might indicate sub-optimal vortex development for the blunt wing at $70.900 \leq Re \leq 86.600$ for $St = 0.20$ and $0.31 \leq St \leq 0.36$ for $Re = 55.100$, which is more or less in line with the hypothesis. It's not known however why these possible sub-optimal vortex development conditions are only locally present in the form of 'dips', as one would expect that the effect would be visible over the entire, or a large part of the investigated Reynolds and Strouhal number regime.

The precise reason for the deviation of the hypothesis is not known, but it should be noted that there are a lot of uncertainties coming into play when analyzing the flow around the different wings. First of all, the method of detecting the vortices and their strength is not perfect at all, and should be taken with a grain of sand. It might be that (some of) the observed differences between wings are the result of this coarse detection method. Secondly, the wings used in the experiment have been self-produced, and the repeatability of measuring with these wings has not yet been verified. It might be that for example, the wings have different stiffnesses and that the measured differences can be explained by such factors. At last, the sharp and blunt wings have been post-processed with a sanding machine to create a sharper and blunter leading-edge. This seemed to have been successful based on the looks and feel of the wing, but in reality, this method might also have altered the leading-edges also in other aspects. For example, the surface roughness might have been changed and the front of the wing might have been made less round than anticipated, as is sketched in figure 45, which could all influence flow transition and separation. This could also be the reason that the original wing creates a stronger vortex at $Re = 70.900$ and $St = 0.20$ than the sharp wing at $St = 0.26$ and the same Reynolds number. Due to all of these uncertainties and the unexpected results regarding the hypothesis, more research is required to make definite statements about the influence of the leading-edge radius on leading-edge vortex formation.

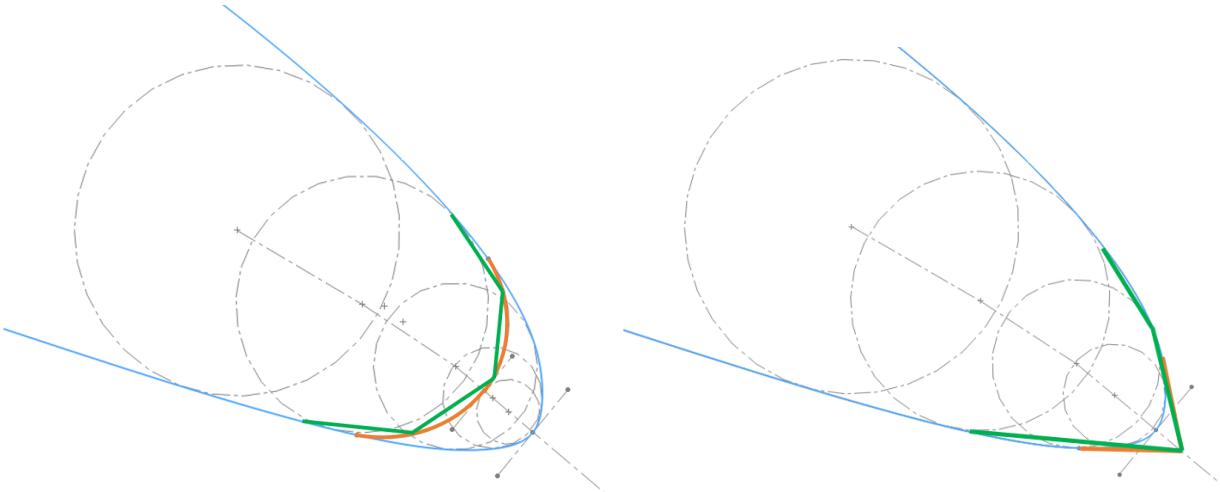

(a) Blunt airfoil design (orange) with possible production errors due to sanding (green) relative to original (blue) airfoil

(b) Sharp airfoil design (orange) with possible production errors due to sanding (green) relative to original (blue) airfoil

Figure 45

8.5 Force data

The reason behind the unreliable force data is not clear and therefore requires more investigation to figure out what precisely has gone wrong. It might be that there is simply too much noise, which messes up the measured data beyond repair. It might be that a problem has occurred during the measurements with the force balance that has remained unnoticed, due to the lack of experience at the University with flapping wings and a half-model balance. It might also be that the calculations used to determine the aerodynamic forces acting on the wing is too crude, and the introduced error due to this method is larger than expected. An other possibility is that the changed location of the black cloth for the top- and bottom flow measurements influenced the flow, and the resulting forces more then expected. The low magnitudes of the average aerodynamic forces can possibly be explained though. They might be caused by the choice of placing the body under zero angle of attack and could be significantly different under a different angle of attack.

The force data is deemed not useful for answering the research questions of this thesis. However, the force data obtained seems to have the potential for future work if unreliabilities can be fixed and the noise reduced.

9 Conclusions and Recommendations

9.1 Conclusions

The main goal of this research was to learn more about leading-edge vortex formation on the RoBird's wing, as there is still very little knowledge about this subject in the context of vertebrate flight. The main question was therefore if leading-edge vortices are present on the bottom surface of the RoBird's wing under zero angle of attack for $0.20 \leq St \leq 0.41$ and $55.100 \leq Re \leq 106.400$. Based on the particle tracking data it can be concluded that leading-edge vortices indeed form in almost the entire specified Reynolds and Strouhal region. Only the sharp and blunt wings do not form a LEV at $Re = 55.100$ and $St = 0.20$, but for all the other measurements a LEV was observed.

For the cases where a LEV was found, the effect of the respective Strouhal number, Reynolds number, and leading-edge radius on LEV formation was investigated using the maximum U_y/U_∞ inside the vortex to represent vortex strength. Based on the literature a hypothesis was created, stating that leading-edge vortex formation on flapping vertebrate wings will be the most profound for sharp wings operating at high Strouhal numbers and Re $\approx$ 100.000.

It could clearly be seen that the vortex strength indeed increased for increasing Strouhal numbers for all three wings investigated, despite the quantification method with U_y/U_∞ being a rather crude method. A Reynolds number effect could also be observed at $St = 0.20$, with no or a weak vortex at the low Reynolds numbers, a peak in vortex strength at approximately $70.900 \leq Re \leq 86.600$, followed by a steady decrease in vortex strength when increasing the Reynolds number even more. The clear differences in local Reynolds number compared to the average Reynolds number over the wing can be useful in explaining the observed LEV formation, but more research is needed into this subject to make any definite statements. It is unlikely however that the observed trends are caused by the local Reynolds numbers, leaving the average Reynolds number as the only viable option to explain the observed trends. At $St = 0.26$ the effect of the Reynolds number seems to be limited, resulting in a more or less constant vortex strength for all measured wings at varying Reynolds numbers. The low amount of data points makes it hard to make definite statements though, so more research is needed to determine if the Reynolds number has a decreasing effect on LEV formation for increasing Strouhal numbers. The Reynolds region associated with the observed peak at $St = 0.20$ is believed to be close enough to the expected peak of $Re \approx 100.000$ to be in line with the literature.

The data suggest that vortex formation is most profound for the original wing, which is contrary to the hypothesis. This might be explained by the method of producing the wings and/or the crude quantification method of the vortex strength. Local dips in the data of the blunt wing raise questions about possible local sub-optimal vortex development conditions for a blunt wing, which could be in line with the hypothesis. However, there is still not enough data and too much uncertainty about the measured data to make any definite statements about the influence of the leading-edge radius.

The force measurements from a half-model balance have been processed with a low-frequency filter to subtract noise from the data. This data and filtered force data from measurements without wind have been subtracted from each other to obtain the aerodynamic forces acting on the wing. When comparing the average aerodynamic forces of different, similar measurements though, no consistency could be found at all. Although the obtained data looks promising, this leads to the conclusion that force measurements with a half-model balance can not yet be used reliably to determine lift and drag forces acting on the RoBird's flapping wing in a wind tunnel. It might be that the error introduced by calculating the aerodynamic forces, or by changing the location of the black cloth at the side of the wind tunnel is simply too big, but the data is not available to back this claim. When looking at this unreliable data at the region where LEVs are known to develop, no clear trend could be observed which could be associated with any LEVs.

9.2 Recommendations

The regime where research was possible was highly limited by the measuring set-up, especially the flapping mechanism. Measurements with a frequency above $f \approx 3\,Hz$ would be very interesting as the knowledge of flapping flight for $Re > 100.000$ is even more limited than what has been investigated for this thesis. Achieving higher flapping frequencies would also enable more research at higher Strouhal numbers, and would allow for gathering enough data to make more definite statements about the effect of Re at higher Strouhal numbers. Also, a working $\Delta\Phi$ mechanism would enable research closer to the actual flight kinematics of birds. It's therefore recommended to create a flapping mechanism that can flap at frequencies significantly higher than $f = 3\,Hz$ and preferably has a working phase change mechanism.

The main uncertainties in the particle tracking data could be traced back to either the method of detection of the vortex (strength) or the error introduced by the production method of the different wings. It is therefore recommended to improve the production process until wings can be produced reliably with approximately the same mass, moment of inertia, stiffness en torsion characteristics without the need for any corrections with a sanding machine. Different wings with the same design can then be tested with both PTV and with a force balance to check for the repeatability of the results obtained.

For the detection of the vortex (strength), it is recommended to try to increase the particle tracks in the region where leading-edge vortices can be present. This could be done by optimizing the post-processing of the data and by further minimizing reflections coming from the wing, for example by better aiming of the laser or wrapping of the wing to make the surface structure less coarse. Measuring more flapping cycles per measurement further increases the certainty about claims, especially for measurements at a relatively low Strouhal- and Reynolds number, where it is very hard to judge if a vortex is or isn't present. More cycles per measurement also help when the data is binned and averaged, which results in a more complete and reliable vector field of the data. This vector field can then be used to quantify the vortices with the use of vorticity or the Q-criterion, which are less crude methods than the used maximum U_y/U_∞ inside of the vortices.

Despite using the settings as prescribed by [Faleiros et al., 2019] to create HFSBs, it is for future research recommended to check if the bubbles generated are actually neutrally buoyant, due to the contradicting input settings provided by LaVision.

For the force balance measurements, it is recommended to perform measurements with a simplified set-up, gradually increasing the complexity, in order to determine the main cause of the inconsistent results. During these measurements, no cloth should be present on either side of semi-open test section. It might be that error introduced to calculate the aerodynamic forces is the cause of the inconsistencies, but this can only be claimed for sure if more measurements are performed. Also, a solution for reducing the noise is needed, since it might contribute to the inconsistencies, and hinders the analysis of the data due to the data being very chaotic, even after processing.

On a more practical level, the timing mechanism with the trigger and the DaVis software did not seem to work that well together, resulting in the timing of the flapping cycle being shifted to random time frames for all the PTV measurements. Due to this shift, it was not clear at what t/T certain phenomena happened, and therefore hindered the comparison of different measurements with each other. On top of that, some measurements developed vortices just as a new cycle started, resulting in a gap in the measurement data, and more difficulties in extracting for example U_y/U_∞. Also, the velocities and accelerations in DaVis are in cartesian coordinates, while the kinematic model is in semi-polar coordinates. It's not known if this can be changed in DaVis, or for example ParaView, but this would help with analyzing the flow.

10 Acknowledgements

I would like to thank Luuk Groot Koerkamp for his guidance throughout the entire thesis. Your knowledge about everything regarding flapping flight and Particle Tracking Velocimetry was of enormous value throughout this project. When I doubted my work you were always there to talk. You never pushed me in a certain direction and trusted me with the set-up, which was perfect for me to find out what topics I found interesting and how I wanted to perform my research. And on top of that, I had a lot of fun working with you!

Thanks to Alexander Dijkshoorn, Elise Leusink, and Steven Wanrooij for their enormous help with the preparations for, and production of the RoBird wings. Without your knowledge, skills, and creative solutions to all the unexpected problems I encountered, I would never have been able to produce the wings as they are now. Thanks to Clear Flight Solutions for the information they provided regarding the production process of the wings, and the willingness they showed to help out where they could. Thanks to Emre Ozturk, who helped me with the preparation of the measurement set-up, and helped me during my entire measurement campaign in the wind tunnel. Without your help, I would have never been able to generate so much data and extract the maximum out of the measurement set-up. Thanks to Walter Lette, who was always willing to help with anything related to the wind tunnel. Also thanks to Gijs van Oort, who took all the time in the world to answer all my questions about the flapping mechanism.

In addition, I would like to thank my exam committee. Prof. dr. ir. C.H. Venner as Chair of the Engineering Fluid Dynamics Group, ir. L. Groot Koerkamp as daily supervisor, dr. ir M.P.J. Sanders and Dr. A. Martinetti Msc. as an external member.

I would have never been able to be where I am today without the support and love of my parents, Kees and Sandra, and my siblings Robin, David, Marije, and Tijmen. Studying in Twente often separated us, but when I returned home for the weekend you were always there for good conversations, silly jokes, and lots of fun.

Thanks to my friends both in Nijkerk and here in Enschede, with whom I had the most amazing student time I could possibly imagine. In particular, I would like to thank my dispuut 'O Tempora, O Mores'. You never fail to amaze me with all the wonderful and stupid things you can come up with at our dispuuts avonden and the wonderful times we have together. Thanks for helping me clear my head through my thesis process when I needed that. Thanks to my (ex) housemates of Het Krat. Despite having one of the most crappy buildings in Enschede, you guys created the most amazing home (and kratbad) one can dream of.

Maybe most of all I would like to thank my fiancée Bente Meijerink. You have been by my side for almost my entire studies and have supported me through all my highs and lows. You helped me relax when I was busy and helped me focus when my work was boring or difficult.

At last some honorable mentions of contributors to my studies in one way or another in no particular order: Brian Douglas, Mickie Krause, Marcus Tullius Cicero, Ikke Hüftgold, Mr. List, Markus Becker und das Rote Pferd, The writers of Wikipedia, my Dell Precision M2800 laptop, the brothers scooter, the inventor of the metric system Gabriel Mouton, the knights who say Ni, Harro's scheurijzer, RED E, Grand Vizier Sissa Ben Dahir and King Shirham of India, Great Gam Gam, Paul Elstak, The Royal Society for the prevention of Birds, Luc Hartmans and his mother, Sir Bedivere who is wise in the ways of science, The planet Saturn, and of course all of its rings, Helene Fischer, my neighbors cat Puck, the design department of the Bowmore distillery, Adrian Newey, the village Ausbach and all of it's residents, a man named Brian, King Willem-Alexander of the Netherlands and his wife Maxima, the Brandaris, Karl Marx, and last but not least: Grolsch.

References

[Altshuler et al., 2004] Altshuler, D. L., Dudley, R., and Ellington, C. P. (2004). Aerodynamic forces of revolving hummingbird wings and wing models. *Journal of zoology*, 264(4):327–332. doi:10.1017/S0952836904005813.

[Arredondo-Galeana and Viola, 2018] Arredondo-Galeana, A. and Viola, I. M. (2018). The leading-edge vortex of yacht sails. *Ocean Engineering*, 159:552–562. doi:10.1016/j.oceaneng.2018.02.029.

[Brentjes and Hoeijmakers, 2017] Brentjes, A. and Hoeijmakers, H. W. (2017). Experimental investigation into wake flapping wing robotic bird. In *35th AIAA Applied Aerodynamics Conference*, page 3409. doi:10.2514/6.2017-3409.

[Chin and Lentink, 2016] Chin, D. D. and Lentink, D. (2016). Flapping wing aerodynamics: from insects to vertebrates. *Journal of Experimental Biology*, 219(7):920–932. doi:10.1242/jeb.042317.

[Chin et al., 2020] Chin, Y.-W., Kok, J. M., Zhu, Y.-Q., Chan, W.-L., Chahl, J. S., Khoo, B. C., and Lau, G.-K. (2020). Efficient flapping wing drone arrests high-speed flight using post-stall soaring. *Science Robotics*, 5(44):eaba2386. doi:10.1126/scirobotics.aba2386.

[de Santana et al., 2018] de Santana, L., Sanders, M. P. J., Venner, C. H., and Hoeijmakers, H. W. (2018). The utwente aeroacoustic wind tunnel upgrade. In *2018 AIAA/CEAS Aeroacoustics Conference*, page 3136. doi:10.2514/6.2018-3136.

[Dickinson and Gotz, 1993] Dickinson, M. H. and Gotz, K. G. (1993). Unsteady aerodynamic performance of model wings at low reynolds numbers. *Journal of experimental biology*, 174(1):45–64. doi:10.1242/jeb.174.1.45.

[Dickinson et al., 1999] Dickinson, M. H., Lehmann, F.-O., and Sane, S. P. (1999). Wing rotation and the aerodynamic basis of insect flight. *Science*, 284(5422):1954–1960. doi:10.1126/science.284.5422.1954.

[Eldredge and Jones, 2019] Eldredge, J. D. and Jones, A. R. (2019). Leading-edge vortices: mechanics and modeling. *Annual Review of Fluid Mechanics*, 51:75–104. doi:10.1146/annurev-fluid-010518-040334.

[Ellington et al., 1996] Ellington, C. P., Van Den Berg, C., Willmott, A. P., and Thomas, A. L. (1996). Leading-edge vortices in insect flight. *Nature*, 384(6610):626–630. doi:10.1038/384626a0.

[Faleiros et al., 2019] Faleiros, D. E., Tuinstra, M., Sciacchitano, A., and Scarano, F. (2019). Generation and control of helium-filled soap bubbles for piv. *Experiments in Fluids*, 60(3):1–17. doi:10.1007/s00348-019-2687-4.

[Floreano and Wood, 2015] Floreano, D. and Wood, R. J. (2015). Science, technology and the future of small autonomous drones. *nature*, 521(7553):460–466. doi:10.1038/nature14542.

[Folkertsma et al., 2017] Folkertsma, G. A., Straatman, W., Nijenhuis, N., Venner, C. H., and Stramigioli, S. (2017). Robird: a robotic bird of prey. *IEEE robotics & automation magazine*, 24(3):22–29. doi:10.1109/MRA.2016.2636368.

[Gill Jr et al., 2005] Gill Jr, R. E., Piersma, T., Hufford, G., Servranckx, R., and Riegen, A. (2005). Crossing the ultimate ecological barrier: evidence for an 11 000-km-long nonstop flight from alaska to new zealand and eastern australia by bar-tailed godwits. *The Condor*, 107(1):1–20. doi:10.1093/condor/107.1.1.

[Groot Koerkamp, 2018] Groot Koerkamp, L. H. (2018). PIV measurements in the wake of a robotic bird. Master's thesis, University of Twente, the Netherlands.

[Harbig et al., 2013] Harbig, R. R., Sheridan, J., and Thompson, M. C. (2013). Relationship between aerodynamic forces, flow structures and wing camber for rotating insect wing planforms. *Journal of Fluid Mechanics*, 730:52–75. doi:10.1017/jfm.2013.335.

[Hedenström and Johansson, 2015] Hedenström, A. and Johansson, L. C. (2015). Bat flight: aerodynamics, kinematics and flight morphology. *The Journal of experimental biology*, 218(5):653–663. doi:10.1242/jeb.031203.

[Hubel and Tropea, 2010] Hubel, T. Y. and Tropea, C. (2010). The importance of leading edge vortices under simplified flapping flight conditions at the size scale of birds. *Journal of Experimental Biology*, 213(11):1930–1939. doi:10.1088/1748-3182/9/2/025006.

[Jahanmiri, 2011] Jahanmiri, M. (2011). Laminar separation bubble: its structure, dynamics and control. Technical report, Chalmers University of Technology. Retrieved from `https://core.ac.uk/display/70588164?utm_source=pdf&utm_medium=banner&utm_campaign=pdf-decoration-v1`.

[Jongerius, 2017] Jongerius, C. H. (2017). "Real-time" control system for wing twist and flapping frequency. Bachelor's thesis, University of Twente, the Netherlands. Retrieved from `https://purl.utwente.nl/essays/81007`.

[Kasiemkhan and van Vilsteren, 2021] Kasiemkhan, S. A. and van Vilsteren, J. G. (2021). *UT high lift device & HM balances and angle setting tool*. NLR.

[Kruyt et al., 2015] Kruyt, J. W., Van Heijst, G. F., Altshuler, D. L., and Lentink, D. (2015). Power reduction and the radial limit of stall delay in revolving wings of different aspect ratio. *Journal of the Royal Society Interface*, 12(105):20150051. doi:10.1098/rsif.2015.0051.

[Lentink and Dickinson, 2009] Lentink, D. and Dickinson, M. H. (2009). Rotational accelerations stabilize leading edge vortices on revolving fly wings. *Journal of experimental biology*, 212(16):2705–2719. doi:10.1242/jeb.022269.

[Lilley, 1998] Lilley, G. (1998). A study of the silent flight of the owl. In *4th AIAA/CEAS aeroacoustics conference*, page 2340. doi:10.2514/6.1998-2340.

[Muijres et al., 2012] Muijres, F. T., Johansson, L. C., and Hedenström, A. (2012). Leading edge vortex in a slow-flying passerine. *Biology letters*, 8(4):554–557. doi:10.1098/rsbl.2012.0130.

[Muijres et al., 2014] Muijres, F. T., Johansson, L. C., Winter, Y., and Hedenström, A. (2014). Leading edge vortices in lesser long-nosed bats occurring at slow but not fast flight speeds. *Bioinspiration & biomimetics*, 9(2):025006. doi:10.1088/1748-3182/9/2/025006.

[Norberg, 2012] Norberg, U. M. (2012). *Vertebrate flight: mechanics, physiology, morphology, ecology and evolution*, volume 27. Springer Science & Business Media. doi:10.1007/978-3-642-83848-4.

[Nudds et al., 2004] Nudds, R. L., Taylor, G. K., and Thomas, A. L. (2004). Tuning of strouhal number for high propulsive efficiency accurately predicts how wingbeat frequency and stroke amplitude relate and scale with size and flight speed in birds. *Proceedings of the Royal Society of London. Series B: Biological Sciences*, 271(1552):2071–2076. doi:10.1098/rspb.2004.2838.

[Polhamus, 1966] Polhamus, E. C. (1966). A concept of the vortex lift of sharp-edge delta wings based on a leading-edge-suction analogy. Technical report, NASA TN D-3767, Langely Research Center, Langely Station, Hampton, Va. Required from `https://ntrs.nasa.gov/api/citations/19670003842/downloads/19670003842.pdf`.

[Ponitz et al., 2014] Ponitz, B., Schmitz, A., Fischer, D., Bleckmann, H., and Brücker, C. (2014). Diving-flight aerodynamics of a peregrine falcon (falco peregrinus). *PLoS One*, 9(2):e86506. doi:10.1371/journal.pone.0086506.

[Raffel et al., 2018] Raffel, M., Willert, C. E., et al. (2018). *Particle image velocimetry: a practical guide*, volume 3. Springer Cham. doi:10.1007/978-3-319-68852-7.

[Ramesh et al., 2012] Ramesh, K., Ke, J., Gopalarathnam, A., and Edwards, J. (2012). Effect of airfoil shape and reynolds number on leading edge vortex shedding in unsteady flows. In *30th AIAA applied aerodynamics conference*, page 3025. doi:10.2514/6.2012-3025.

[Rival et al., 2014] Rival, D. E., Kriegseis, J., Schaub, P., Widmann, A., and Tropea, C. (2014). Characteristic length scales for vortex detachment on plunging profiles with varying leading-edge geometry. *Experiments in fluids*, 55(1):1–8. doi:10.1007/s00348-013-1660-x.

[Sane, 2003] Sane, S. P. (2003). The aerodynamics of insect flight. *Journal of experimental biology*, 206(23):4191–4208. doi:10.1242/jeb.00663.

[Schanz et al., 2016] Schanz, D., Gesemann, S., and Schröder, A. (2016). Shake-the-box: Lagrangian particle tracking at high particle image densities. *Experiments in fluids*, 57(5):1–27. doi:10.1007/s00348-016-2157-1.

[Schanz et al., 2012] Schanz, D., Gesemann, S., Schröder, A., Wieneke, B., and Novara, M. (2012). Non-uniform optical transfer functions in particle imaging: calibration and application to tomographic reconstruction. *Measurement Science and Technology*, 24(2):024009. doi:10.1088/0957-0233/24/2/024009.

[Sedov, 1965] Sedov, L. I. (1965). *Two-dimensional problems in hydrodynamics and aerodynamics*. Interscience Publishers, New York. 10-20, Translated and edited by C. Chu, H Cohen and B. Seckler, doi:10.1016/0016-0032(66)90076-7.

[Swartz et al., 2008] Swartz, S. M., Breuer, K. S., and Willis, D. J. (2008). Aeromechanics in aeroecology: flight biology in the aerosphere. *Integrative and comparative biology*, 48(1):85–98. doi:10.1093/icb/icn054.

[Taylor et al., 2003] Taylor, G. K., Nudds, R. L., and Thomas, A. L. (2003). Flying and swimming animals cruise at a strouhal number tuned for high power efficiency. *Nature*, 425(6959):707–711. doi:10.1038/nature02000.

[Thielicke and Stamhuis, 2015] Thielicke, W. and Stamhuis, E. J. (2015). The influence of wing morphology on the three-dimensional flow patterns of a flapping wing at bird scale. *Journal of Fluid Mechanics*, 768:240–260. doi:10.1017/jfm.2015.71.

[Usherwood and Ellington, 2002] Usherwood, J. R. and Ellington, C. P. (2002). The aerodynamics of revolving wings i. model hawkmoth wings. *Journal of Experimental biology*, 205(11):1547–1564. doi:10.1242/jeb.205.11.1547.

[UToday, 2012] UToday (2012). Nieuwe tijdelijke ondernemersplaatsen. Date accessed: Okt. 22, 2022 Retrieved from `https://www.utoday.nl/news/58118/nieuwe_tijdelijke_ondernemersplaatsen`.

[Vaseur, 2014] Vaseur, C. S. E. (2014). Robird wind tunnel test setup design. Master's thesis, University of Twente, the Netherlands. Retrieved from `https://purl.utwente.nl/essays/66414`.

[Videler et al., 2004] Videler, J. J., Stamhuis, E. J., and Povel, G. D. E. (2004). Leading-edge vortex lifts swifts. *Science*, 306(5703):1960–1962. doi:10.1126/science.1104682.

[Warrick et al., 2005] Warrick, D. R., Tobalske, B. W., and Powers, D. R. (2005). Aerodynamics of the hovering hummingbird. *Nature*, 435(7045):1094–1097. doi:10.1038/nature03647.

[Wieneke, 2008] Wieneke, B. (2008). Volume self-calibration for 3d particle image velocimetry. *Experiments in fluids*, 45(4):549–556. doi:10.1007/s00348-008-0521-5.

[Wilson Jr and Lovell, 1947] Wilson Jr, H. A. and Lovell, J. C. (1947). Full-scale investigation of the maximum lift and flow characteristics of an airplane having approximately triangular plan form. Technical report, NACA. RM. No RM L6K20. Retrieved from `https://apps.dtic.mil/sti/pdfs/ADB814224.pdf`.

[Wolf and Konrath, 2015] Wolf, T. and Konrath, R. (2015). Avian wing geometry and kinematics of a free-flying barn owl in flapping flight. *Experiments in Fluids*, 56(2):1–18. doi:10.1007/s00348-015-1898-6.

Appendices

A Kinematic Relation between $\beta(t)$, $\Phi(t)$ and $\dot{\Phi}(t)$

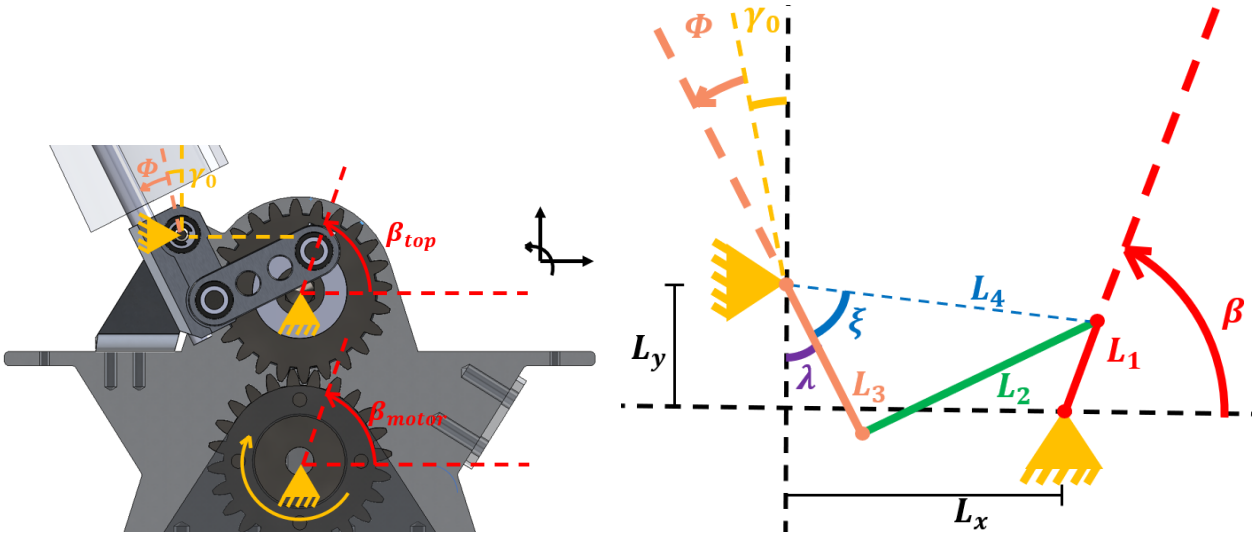

(a) Flapping mechanism

(b) Free body diagram of the crank rocker mechanism

Figure 46

Figure 46a shows the flapping mechanism used in the experiment, whereas Figure 46b shows the free body diagram of the crank rocker mechanism. The motor is attached to the bottom gear of Figure 46a, and in the current view, it spins in the clockwise direction, as shown with the yellow arrow. The 1:1 gear ratio will therefore let the top gear rotate in the counterclockwise direction. Therefore β is defined as:

$$\beta = \beta_{top} = -\beta_{motor} \tag{11}$$

The dimensions of the rigid components are known and can be found in table 5.

What	Length [mm]
L_x	25
L_y	12
L_1	9
L_2	23.5
L_3	15.5

Table 5: Dimensions of different components crank rocker mechanism

With the use of Figure 46b, Φ can now rewritten as a function of β. First $L_4(\beta)$ can be calculated:

$$L_4(\beta) = \sqrt{[L_x + L_1\cos(\beta)]^2 + [L_y - L_1\sin(\beta)]^2} \tag{12}$$

Using the cosine rule $\xi(\beta)$ can now be calculated:

$$L_2^2 = L_3^2 + L_4(\beta)^2 - 2L_3L_4(\beta)\cos(\xi) \tag{13}$$

$$\xi(\beta) = cos^{-1}\left(\frac{-L_2^2 + L_3^2 + L_4(\beta)^2}{2L_3L_4(\beta)}\right) \tag{14}$$

The combined angle $\lambda(\beta) + \xi(\beta)$ can be calculated as:

$$\lambda(\beta) + \xi(\beta) = tan^{-1}\left(\frac{L_x + L_1\cos(\beta)}{L_y - L_1\sin(\beta)}\right) \tag{15}$$

Inserting Equation 14 into this equation results in:

$$\lambda(\beta) = tan^{-1}\left(\frac{L_x + L_1\cos(\beta)}{L_y - L_1\sin(\beta)}\right) - cos^{-1}\left(\frac{-L_2^2 + L_3^2 + L_4(\beta)^2}{2L_3L_4(\beta)}\right) \tag{16}$$

$$= tan^{-1}\left(\frac{L_x + L_1\cos(\beta)}{L_y - L_1\sin(\beta)}\right) - cos^{-1}\left(\frac{-L_2^2 + L_3^2 + [L_x + L_1\cos(\beta)]^2 + [L_y - L_1\sin(\beta)]^2}{2L_3\sqrt{[L_x + L_1\cos(\beta)]^2 + [L_y - L_1\sin(\beta)]^2}}\right) \tag{17}$$

Using the geometric relation $\lambda(\beta) = \Phi(\beta) + \gamma_0$ results in Φ as a function of β:

$$\begin{aligned}\Phi(\beta) = {} & tan^{-1}\left(\frac{L_x + L_1\cos(\beta)}{L_y - L_1\sin(\beta)}\right) \quad \cdots \\ & - cos^{-1}\left(\frac{-L_2^2 + L_3^2 + [L_x + L_1\cos(\beta)]^2 + [L_y - L_1\sin(\beta)]^2}{2L_3\sqrt{[L_x + L_1\cos(\beta)]^2 + [L_y - L_1\sin(\beta)]^2}}\right) - \gamma_0\end{aligned} \tag{18}$$

The motor rotates with a constant angular velocity, so β can be written as a function of time t and flapping frequency f. The start of the flapping motion is defined such that the wing is parallel to the midline during the upstroke, such that $\Phi(\beta) = 0$. The motor angle $\beta(f,t)$ corresponding to this position is found to be 268.1°. Therefore β can be written as:

$$\beta(f,t) = 360ft + 268.1 \tag{19}$$

Which allows Φ to be rewritten into:

$$\begin{aligned}\Phi(f,t) = {} & tan^{-1}\left(\frac{L_x + L_1\cos(360ft + 268.1)}{L_y - L_1\sin(360ft + 268.1)}\right) \quad \cdots \\ & - cos^{-1}\left(\frac{-L_2^2 + L_3^2 + [L_x + L_1\cos(360ft + 268.1)]^2 + [L_y - L_1\sin(360ft + 268.1)]^2}{2L_3\sqrt{[L_x + L_1\cos(360ft + 268.1)]^2 + [L_y - L_1\sin(360ft + 268.1)]^2}}\right)\end{aligned} \tag{20}$$

The angular velocity $\dot{\Phi}(f,t)$ can now be calculated by differentiating $\Phi(f,t)$ over time while keeping f constant:

$$\dot{\Phi}(f,t) = \left(\frac{\partial\Phi(f,t)}{\partial t}\right)_f = \frac{360fL_1\left[L_1 + L_x cos(360ft) - L_y sin(360ft)\right]}{\left[L_y - L_1 sin(360ft)\right]^2\left[\frac{(L_x + L_1 cos(360ft))^2}{(L_y - L - 1 sin(360ft))^2} + 1\right]} \quad \cdots$$

$$- \frac{180fL_1\left[L_y cos(360ft) + L_x sin(360ft)\right]\left[L_1^2 + L_2^2 - L_3^3 + L_x^2 + L_y^2 + 2L_1L_x cos(360ft) - 2L_1L_y sin(360ft)\right]}{L_3\left[(L_x + L_1 cos(360ft))^2 + (L_y - L_1 sin(360ft))^2\right]^{3/2}\sqrt{\frac{1 - 0.25\left[L_3^2 - L_2^2 + (L_x + L_1 cos(360ft))^2 + (L_y - L_1 sin(360ft))^2\right]^2}{L_3^2\left[(L_x + L_1 cos(360ft))^2 + (L_y - L_1 sin(360ft))^2\right]}}} \tag{21}$$

Figure 47 shows the plots of Equation 20 and 21. The blue dots are measured values of Φ from the CAD model of the flapping mechanism, with the corresponding motor angle β. As can be seen, the calculated line of $\Phi(f,t)$ and the measured values of $\Phi(\beta)$ show excellent agreement.

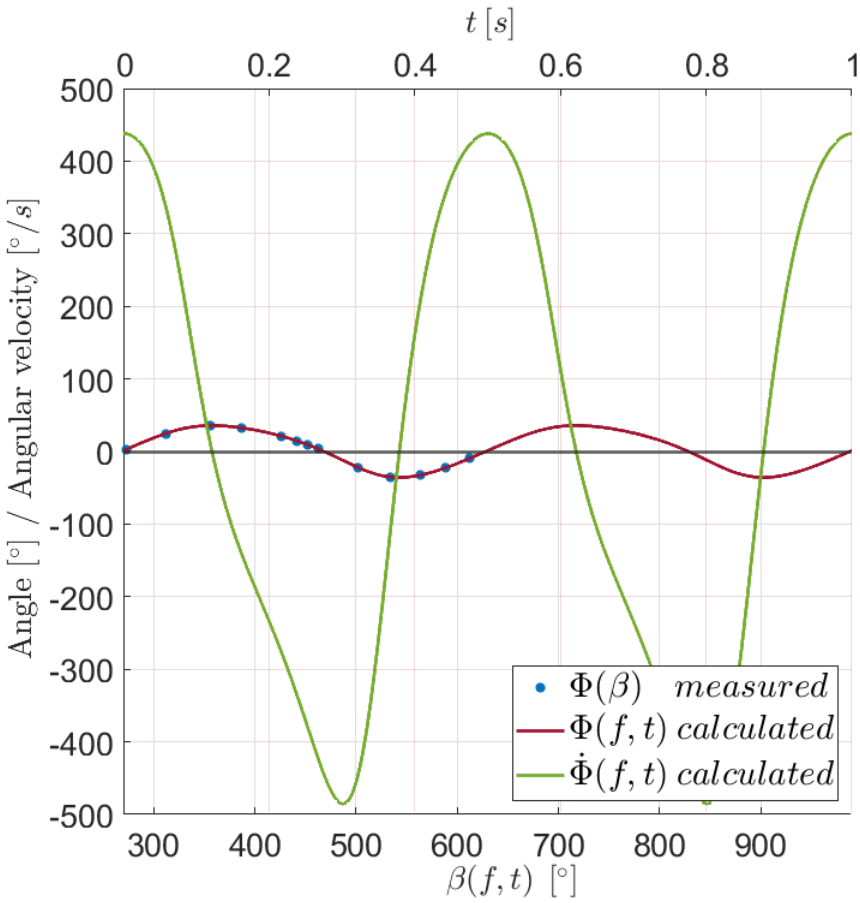

Figure 47: Plots of Equation 20 and 21 for $f = 2Hz$, with measured values of $\Phi(\beta)$ obtained from the CAD model of the flapping mechanism.

B Characterisation of Flow Variables

The value of ρ can be calculated using the ideal gas law, which is given by Equation 22:

$$\rho = \frac{p}{TR_{\text{specific}}} \tag{22}$$

Where p is the pressure (Pa), T is the temperature (K), and R_{specific} is the specific ideal gas constant for dry air, which is 287.05 $Jkg^{-1}K^{-1}$. Throughout the measurements the air temperature has been measured to be $\pm$ 293 K, and the air pressure fluctuated between $101170 \leq p \leq 101870\ Pa$. When using the average pressure $p = 101520\ Pa$, this results in $\rho = 1.206\ kgm^{-3}$. The dynamic viscosity of the air μ can be calculated using Sunderland's law:

$$\mu = \mu_{\text{ref}} \left(\frac{T}{T_{\text{ref}}} \right)^{3/2} \frac{T_{\text{ref}} + S}{T + S} \tag{23}$$

Where μ_{ref} is a reference dynamic viscosity, which is $1.716 * 10^{-5}\ Pas$ for air, T_{ref} is a reference temperature, which is 273.15 K for air, and S is the Sunderland constant, which is 110.4 K. At $T = 293\ K$ it follows that $\mu = 1.813 * 10^{-5}\ Pas$.

C Local Reynolds number

Throughout the thesis, the average Reynolds number is used to describe the flow over the wing. It should be noted however that this average Reynolds number can vary quite drastically from the local Reynolds number. As can be seen in Figure 48, the chord length is significantly higher than the average chord length for the armwing and the first part of the hand wing.

From the root to the kink in the wing $c = 0.225\,m$, and decreases more or less linearly from the kink in the wing to 80% of the total wing length where $c = 0.114\,m$. Over the last 20 % of the wing, the chord decreases more and more, until it reaches the tip, where c approaches $c = 0\,m$. Even when ignoring the tip of the wing, this results in large deviations between local and average Reynolds numbers, as $c \propto Re$. Therefore the local Reynolds number is approximately $1.4 * Re_{\text{avg}}$ over the arm wing and $0.7 * Re_{\text{avg}}$ at 80 % wing length.

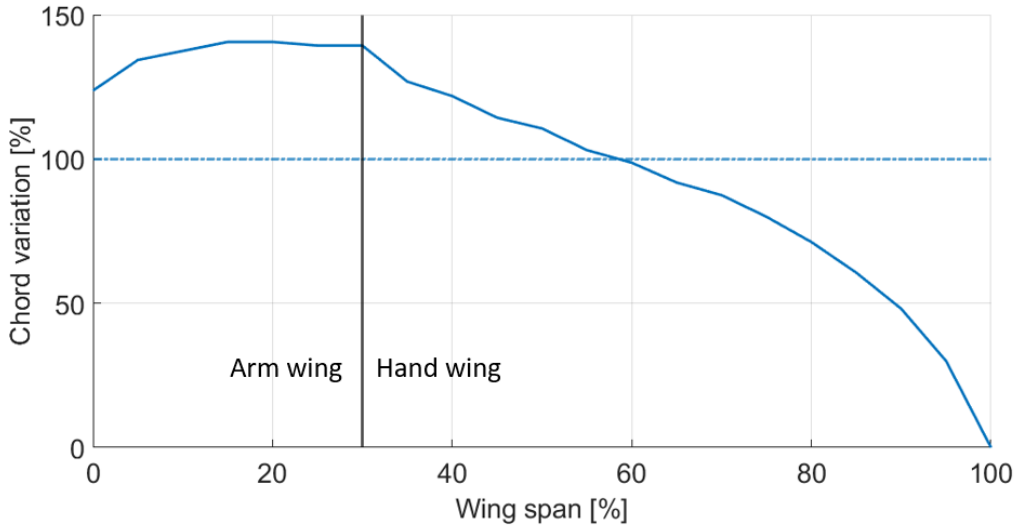

Figure 48: Chord variation over the RoBird's wing span as a percentage of mean chord length. The black line indicates the kink in the wing, which is the separation point between the arm- and handwing

On top of the chord length effect, the flapping motion of the wing induces an extra velocity component $\dot{A}(r, f, t)$, which varies throughout the flapping motion. $\dot{A}(r, f, t)$ increases in strength for increasing f and is very weak near the root and the strongest at the tip. When looking at Figure 5, one can see that the effective velocity U_{eff} as experienced by the wing can be calculated with the Pythagorean theorem:

$$U_{\text{eff}} = \sqrt{U_\infty^2 + \dot{A}(r, f, t)^2} \tag{24}$$

The Strouhal number effectively describes the ratio between forward velocity and flapping velocity, so for constant Strouhal numbers, the relative increase of U_{eff} compared to U_∞ due to the extra velocity component will not change regardless of the average Reynolds number. Since both U_{eff} and U_∞ are used to calculate the local and average Reynolds number respectively, the relative increase of Re_{local} compared to Re_{avg} is also independent of the value of the average Reynolds number. The figures in this chapter, therefore, hold true for every possible average Reynolds number, as long as the Strouhal number is constant.

Figure 49 shows the difference in U_{eff} over a single flapping cycle at the wing tip compared to U_∞ for all the investigated Strouhal numbers. Note, however, that U_{eff} decreases when traveling towards the root, making the effect less dominant. This percentage is exactly how the local Reynolds number behaves compared to the average Reynolds number, as U_{eff} can be used in Equation 5 instead of U_∞.

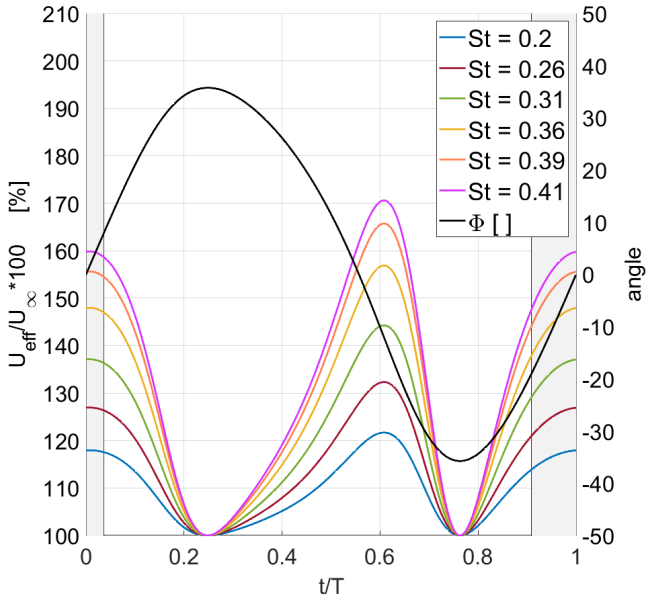

Figure 49: Effective velocity at wingtip compared to U_∞ of a single flapping cycle for $0.20 \leq St \leq 0.41$. The grey region indicates the region where LEVs approximately form, as is discussed in Chapter 7.2

The local Reynolds number is calculated for a relevant time for vortex development $\Phi = -19°$ (t/T = 0.91) and every location on the wing, resulting in the graph in Figure 50. From this figure, it can be seen that especially at the low Strouhal numbers, the local Reynolds number is dominated by the varying chord length, and U_{eff} changes Re_{local} very minimal. For increasing Strouhal numbers the effect increases and appears to be maximal at a wing span of approximately 70 %, but its effect is still relatively modest compared to the varying chord length.

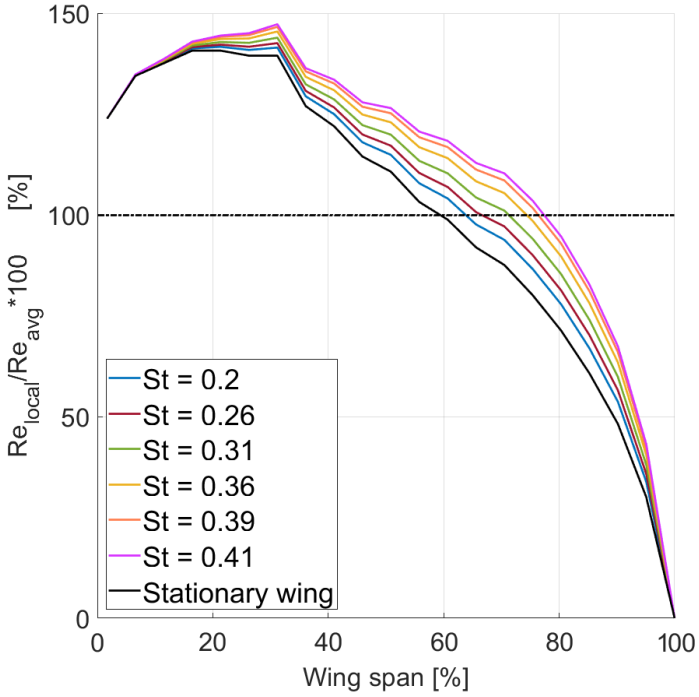

Figure 50: Local Reynolds number at $\Phi = -19°$ $(t/T = 0.91)$ compared to the average Reynolds number. The non-moving wing shows only the chord variation effect.

D Additional Pictures of Measurement Set-up

Figure 51: Measurement set-up for measuring the flow over the bottom of the wing

Figure 52: Measurement set-up for measuring the flow over the top of the wing

E Noise Analysis

E.1 Eigenfrequency Analysis

A crude frequency analysis was performed with a model of the set-up as used in the wind tunnel to gain a rough understanding of where the eigenfrequencies of the set-up might be located. The leaf springs of the force balance were deemed to be the weakest factor of the set-up and therefore thought to be responsible for the main eigenfrequency behavior. The error introduced by the simplifications made is therefore believed to be of an acceptable level. The materials of the force balance were not known, so stainless steel has been selected. It was not possible to simulate the entire flapping set-up with the wing, so a block of 2 kg has been placed on the force balance to simulate its weight. The set-up has been fixed on the top of the two C-shaped steel bars, so the effect of the finite stiffness of the wind tunnel itself is also ignored. The results of the frequency analysis can be seen in Figure 53, with the lowest eigenfrequency located at $f = 50.1\,Hz$.

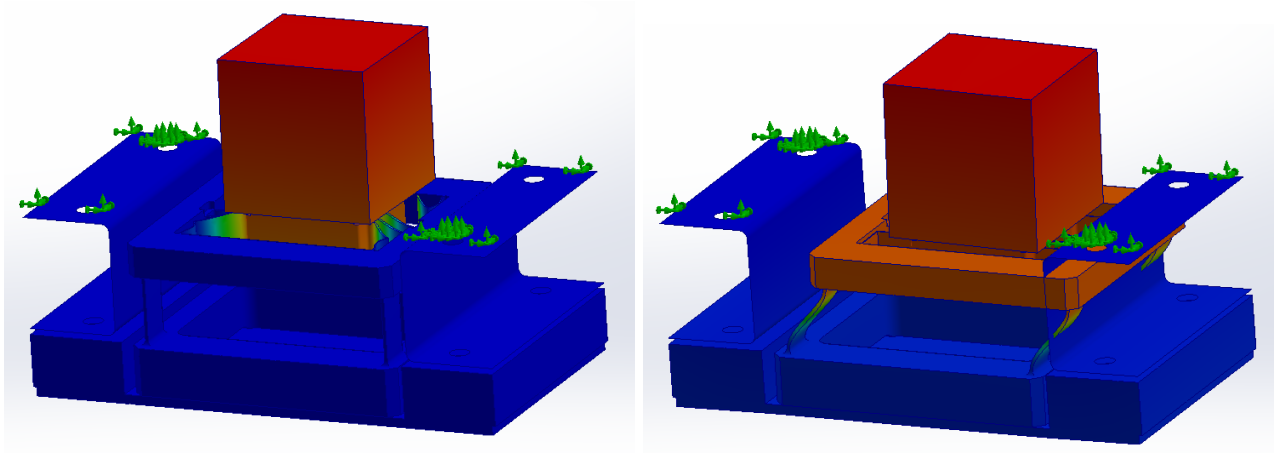

(a) First theoretical eigenfrequency at $f = 50.1\,Hz$ (b) Second theoretical eigenfrequency at $f = 94.2\,Hz$

Figure 53: Crude eigenfrequency analysis on stainless steel model with a weight of 2 kg

E.2 Signal Frequency Domain Analysis

The useful raw force data as described in Chapter 7.3.1 was transformed into the frequency domain using a fast Fourier transform (FFT) algorithm in MATLAB 2021b. The power of the transformed signal was computed with the following equation:

$$\text{Power} = \frac{|\text{DFT}|^2}{n} \tag{25}$$

Where DFT is the data after the Discrete Fourier transform and n is the number of data points. The data is plotted as Relative Power as the signals of the Lift, Thrust, and Moment have different magnitudes, and therefore would not be good visible in the same graph. This is calculated with:

$$\text{Relative Power} = \frac{\text{Power}}{max(\text{Power})} \tag{26}$$

Showing the Relative Powers for all the different measurements performed would result in too many graphs, so, therefore, three cases have been shown in Figures 54 to 56:

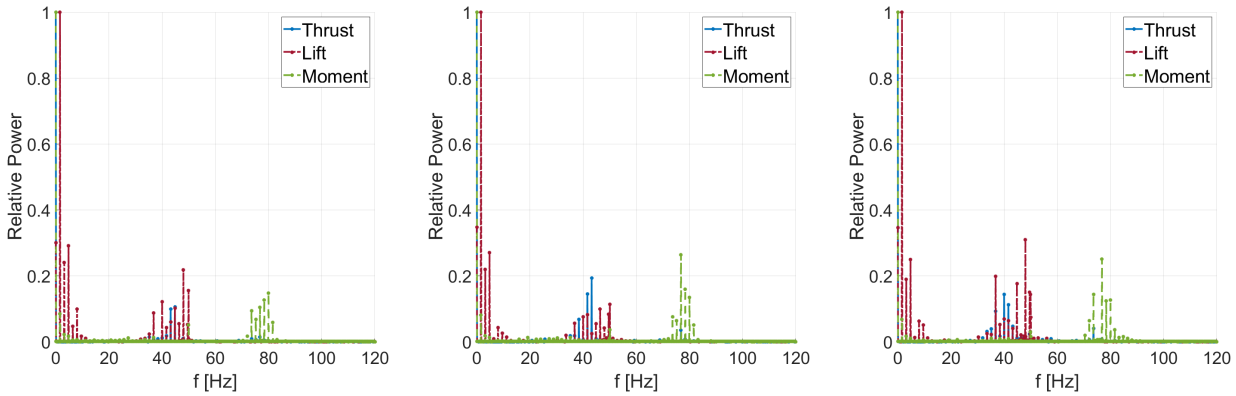

(a) Blunt wing (b) Original wing (c) Sharp wing

Figure 54: Relative power of the Lift, Thrust, and Moment signal for the three different wings at $Re = 55.100$ and $St = 0.20$.

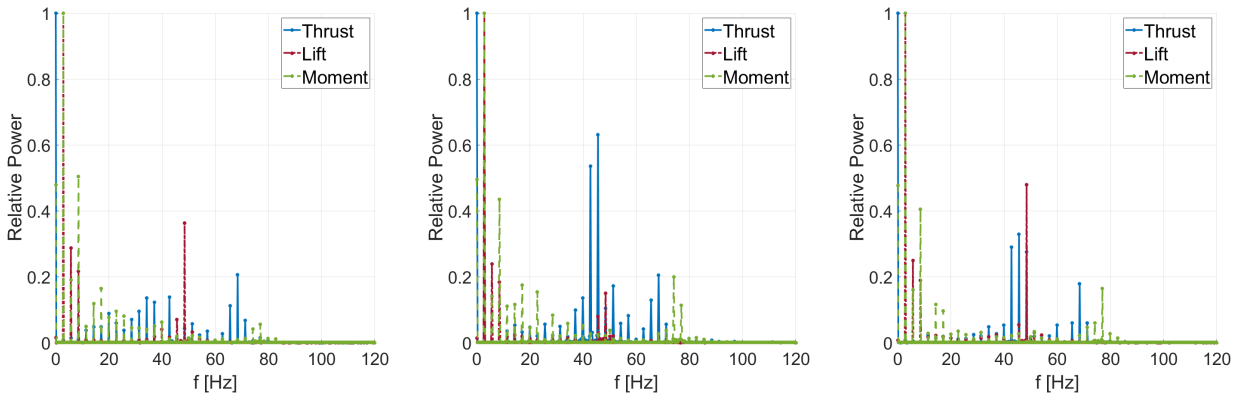

(a) Blunt wing (b) Original wing (c) Sharp wing

Figure 55: Relative power of the Lift, Thrust, and Moment signal for the three different wings at $Re = 98.500$ and $St = 0.20$.

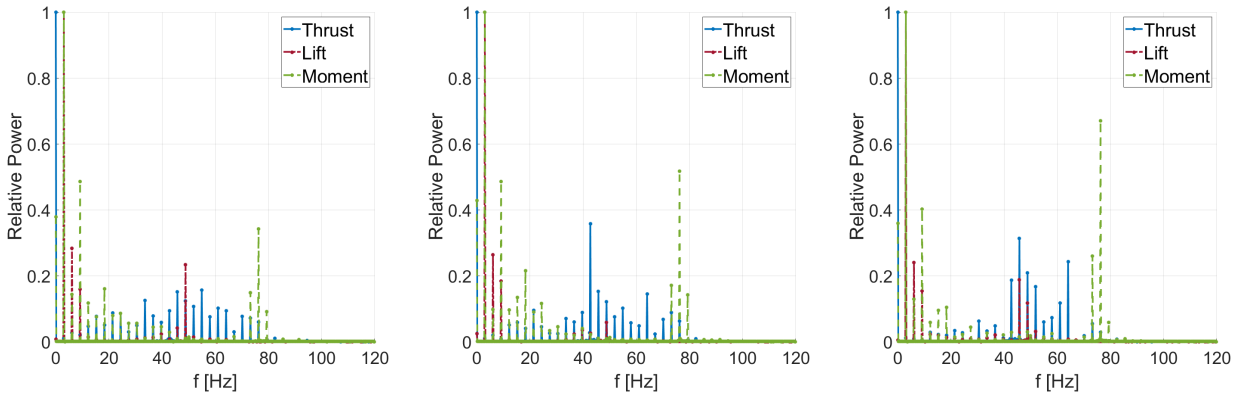

(a) Blunt wing (b) Original wing (c) Sharp wing

Figure 56: Relative power of the Lift, Thrust, and Moment signal for the three different wings at $Re = 55.100$ and $St = 0.39$.

As can be seen from these graphs, the signals have a strong power for $f < 10\,Hz$, with relatively much noise at approximately $40 - 50\,Hz$ and approximately $80\,Hz$. For some cases, such as the $Re = 55.100$ and $St = 0.20$ case, there exists hardly any signal in between, while other measurements have a

relatively continuous transition from data to noise. This makes the choice for the cutoff frequency very hard, as it's hard to say what the useful data and noise is. The two regions of noise match the theoretical eigenfrequencies from Chapter E.1 quite well, although the peaks in the signal are approximately $5 - 10\,Hz$ lower than predicted by the crude eigenfrequency analysis. It is therefore assumed that the noise observed at $40 - 50\,Hz$ is caused by excitation of the first eigenfrequency of the system, and can therefore be ignored. A cutoff frequency of $30\,Hz$ has been chosen as it is located far enough away from the main noise, while still keeping as much as possible useful data.

F Aerodynamic Force Data for Sharp Wing

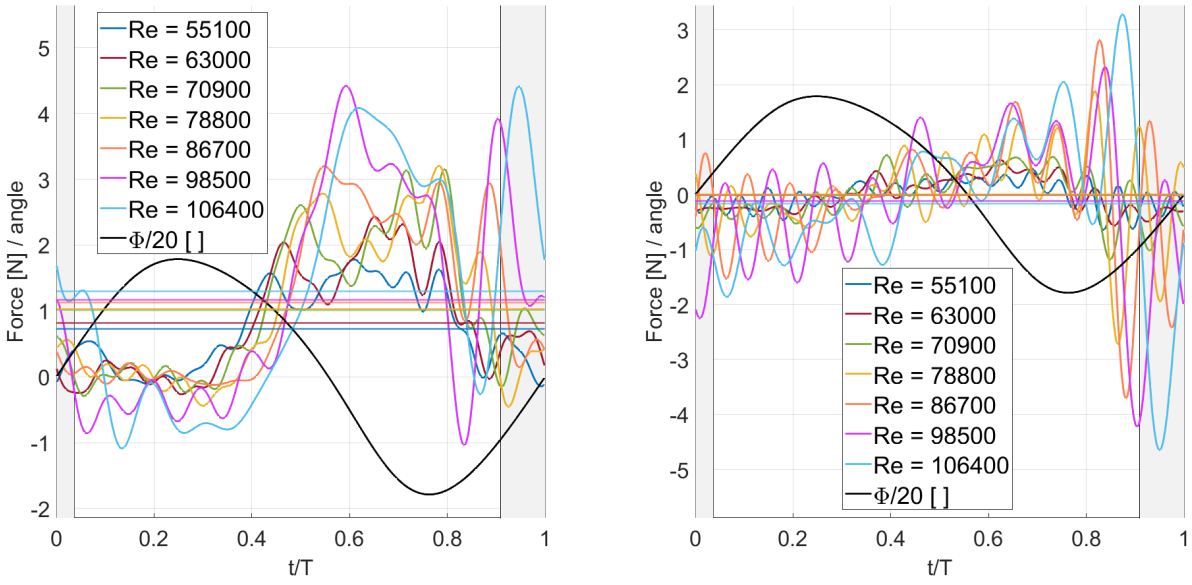

(a) Lift (b) Thrust

Figure 57: Comparison of aerodynamic forces acting on a sharp wing with $55.100 \leq Re \leq 106.400$ and $St = 0.20$, with average force as a horizontal line.

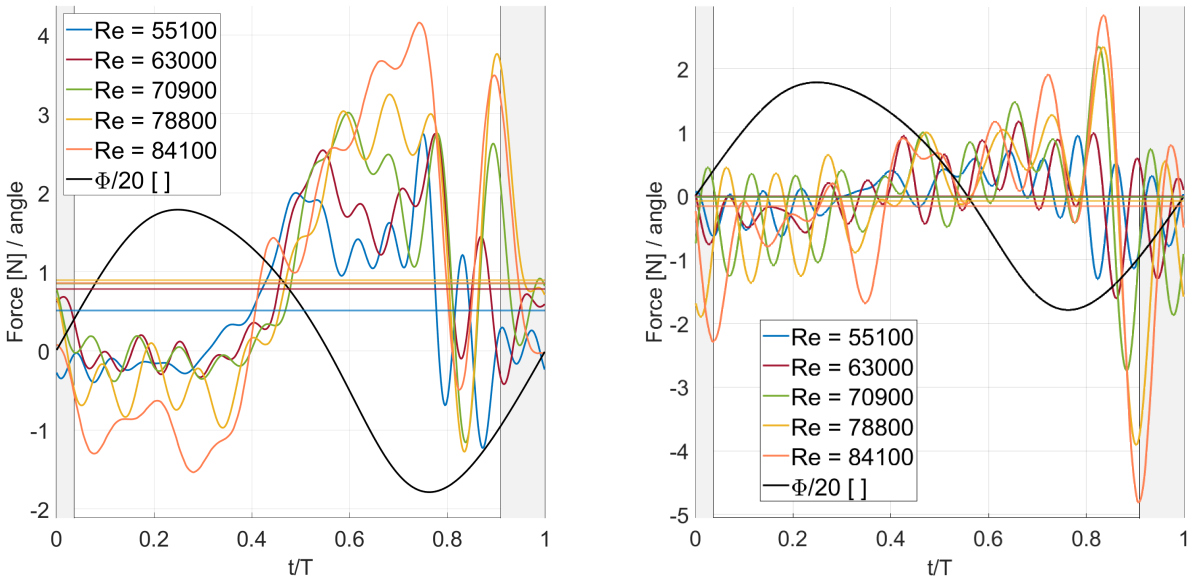

(a) Lift (b) Thrust

Figure 58: Comparison of aerodynamic forces acting on a sharp wing with $55.100 \leq Re \leq 84.100$ and $St = 0.26$, with average force as a horizontal line.

G Average Force Measurement Data

Top measurements: Lift [N]

Blunt

Re:	55100	63000	70900	74500	78800	84100	86600	98500	106400
St = 0,2	-0,14	-0,23	-0,37		-0,51		-0,61	-0,44	-0,45
St = 0,26	-0,17	-0,38	-0,42		-0,38		-0,59		
St = 0,31	-0,09								
St = 0,36	-0,04								
St = 0,39	-0,06								
St = 0,41	-0,05								

Original

Re:	55100	63000	70900	74500	78800	84100	86600	98500	106400
St = 0,2	-0,09	-0,16	-0,19		-0,29		-0,42	-0,57	
St = 0,26	-0,16	-0,11	-0,24	-0,34					
St = 0,31	-0,10								
St = 0,36	-0,19								
St = 0,39	-0,18								
St = 0,41									

Sharp

Re:	55100	63000	70900	74500	78800	84100	86600	98500	106400
St = 0,2	-0,10	-0,12	-0,19		-0,20		-0,31	-0,66	-0,71
St = 0,26	-0,08	-0,25	-0,35		-0,31	-0,42			
St = 0,31	-0,24								
St = 0,36	-0,19								
St = 0,39	-0,19								
St = 0,40									
St = 0,41	-0,19								

Bottom measurements: Lift [N]

Blunt

Re:	55100	63000	70900	74500	78800	84100	86600	98500	106400
St = 0,2	0,85	0,76	0,87		0,97		1,04	1,27	1,37
St = 0,26	0,66	0,73	0,83		0,95		0,99		
St = 0,31	0,66								
St = 0,36	0,70								
St = 0,39	0,66								
St = 0,41	0,63								

Original

Re:	55100	63000	70900	74500	78800	84100	86600	98500	106400
St = 0,2	0,63	0,65	0,78		0,90		1,06	1,09	
St = 0,26	0,65	0,67	0,87	0,92					
St = 0,31	0,62								
St = 0,36	0,69								
St = 0,39	0,58								
St = 0,41									

Sharp

Re:	55100	63000	70900	74500	78800	84100	86600	98500	106400
St = 0,2	0,73	0,82	1,02		1,03		1,13	1,17	1,30
St = 0,26	0,51	0,78	0,85		0,90	0,86			
St = 0,31	0,45								
St = 0,36	0,57								
St = 0,39	0,57								
St = 0,40									
St = 0,41	0,56								

Figure 59: Average aerodynamic lift forces acting on the wing during both the top- and bottom flow measurements

Top measurements: Thrust [N]

Blunt

Re:	55100	63000	70900	74500	78800	84100	86600	98500	106400
St = 0,2	-0,08	-0,08	-0,13		-0,22		-0,28	-0,34	-0,41
St = 0,26	-0,08	-0,15	-0,22		-0,27		-0,41		
St = 0,31	-0,12								
St = 0,36	-0,14								
St = 0,39	-0,20								
St = 0,41	-0,18								

Original

Re:	55100	63000	70900	74500	78800	84100	86600	98500	106400
St = 0,2	-0,11	-0,14	-0,12		-0,17		-0,24	-0,39	
St = 0,26	-0,07	-0,08	-0,18	-0,24					
St = 0,31	-0,10								
St = 0,36	-0,19								
St = 0,39	-0,25								
St = 0,41									

Sharp

Re:	55100	63000	70900	74500	78800	84100	86600	98500	106400
St = 0,2	-0,11	-0,14	-0,18		-0,22		-0,26	-0,43	-0,45
St = 0,26	-0,11	-0,20	-0,24		-0,28	-0,31			
St = 0,31	-0,16								
St = 0,36	-0,18								
St = 0,39	-0,23								
St = 0,40									
St = 0,41	-0,26								

Bottom measurements: Thrust [N]

Blunt

Re:	55100	63000	70900	74500	78800	84100	86600	98500	106400
St = 0,2	0,01	0,00	0,01		0,01		0,01	-0,03	-0,11
St = 0,26	0,00	0,01	0,00		-0,02		-0,11		
St = 0,31	0,00								
St = 0,36	-0,04								
St = 0,39	-0,07								
St = 0,41	-0,13								

Original

Re:	55100	63000	70900	74500	78800	84100	86600	98500	106400
St = 0,2	0,00	-0,01	-0,01		-0,03		-0,04	-0,12	
St = 0,26	0,00	-0,02	-0,03	-0,05					
St = 0,31	-0,04								
St = 0,36	-0,09								
St = 0,39	-0,13								
St = 0,41									

Sharp

Re:	55100	63000	70900	74500	78800	84100	86600	98500	106400
St = 0,2	0,00	-0,01	-0,01		0,00		-0,01	-0,11	-0,16
St = 0,26	-0,01	0,00	-0,01		-0,08	-0,15			
St = 0,31	-0,08								
St = 0,36	-0,08								
St = 0,39	-0,14								
St = 0,40									
St = 0,41	-0,15								

Figure 60: Average aerodynamic thrust forces acting on the wing during both the top- and bottom flow measurements

11 Plagiarism Report

9% Overall Similarity

Top sources found in the following databases:

- 7% Internet database
- Crossref database
- 0% Submitted Works database
- 8% Publications database
- Crossref Posted Content database

TOP SOURCES

The sources with the highest number of matches within the submission. Overlapping sources will not be displayed.

1	edepot.wur.nl Internet	<1%
2	annualreviews.org Internet	<1%
3	ar.scribd.com Internet	<1%
4	flair.monash.edu Internet	<1%
5	arc.aiaa.org Internet	<1%
6	jeb.biologists.org Internet	<1%
7	repository.tudelft.nl Internet	<1%
8	Frank Gijsman, Harry W. Hoeijmakers. "Experimental Study of Flow in ... Crossref	<1%

9	link.springer.com Internet	<1%
10	new.esp.org Internet	<1%
11	Animal Locomotion, 2010. Crossref	<1%
12	pdfs.semanticscholar.org Internet	<1%
13	Markus Raffel, Christian E. Willert, Fulvio Scarano, Christian J. Kähler, ... Crossref	<1%
14	unsworks.unsw.edu.au Internet	<1%
15	utwente on 2021-01-11 Submitted works	<1%
16	biorxiv.org Internet	<1%
17	Antoni Brentjes, Harry W. Hoeijmakers. "Experimental Investigation int... Crossref	<1%
18	pure.tudelft.nl Internet	<1%
19	"New Results in Numerical and Experimental Fluid Mechanics XI", Sprin... Crossref	<1%
20	journals.biologists.com Internet	<1%

21	rahauav.com Internet	<1%
22	frontiersin.org Internet	<1%
23	ltces.dem.ist.utl.pt Internet	<1%
24	mobt3ath.com Internet	<1%
25	par.nsf.gov Internet	<1%
26	spiral.imperial.ac.uk Internet	<1%
27	William Thielicke, EizeJ. Stamhuis. "The influence of wing morphology ... Crossref	<1%
28	utwente on 2020-11-11 Submitted works	<1%
29	Notes on Numerical Fluid Mechanics and Multidisciplinary Design, 2013. Crossref	<1%
30	krex.k-state.edu Internet	<1%
31	web.archive.org Internet	<1%
32	Dong Kim, Mirae Kim, Edoardo Saredi, Fulvio Scarano, Kyung Chun Kim... Crossref	<1%

33	researchmgt.monash.edu Internet	<1%
34	Azar Eslam Panah, James H. J. Buchholz. "Parameter dependence of v... Crossref	<1%
35	H. DONG, R. MITTAL, F. M. NAJJAR. "Wake topology and hydrodynami... Crossref	<1%
36	Hesam Salehipour, David J. Willis. "A coupled kinematics-energetics m... Crossref	<1%
37	J.B. Will, N.P. Kruyt, C.H. Venner. "An experimental study of forced con... Crossref	<1%
38	Kiran Ramesh, Jianghua Ke, Ashok Gopalarathnam, Jack Edwards. "Eff... Crossref	<1%
39	Symposium Transsonicum III, 1989. Crossref	<1%
40	Yingwei Liu, Shingo Matsuno, Hiroki Komatsuzaki, Satomitsu Imai, Yas... Crossref	<1%
41	dspace.lib.cranfield.ac.uk Internet	<1%
42	mafiadoc.com Internet	<1%
43	open.uct.ac.za Internet	<1%
44	openaccess.city.ac.uk Internet	<1%

45	von Ellenrieder, K.D.. "Fluid mechanics of flapping wings", Experimental... Crossref	<1%
46	"Handbook of Wind Energy Aerodynamics", Springer Science and Busin... Crossref	<1%
47	Makoto Mizoguchi, Hajime Itoh. "Effect of Aspect Ratio on Aerodynami... Crossref	<1%
48	m.scirp.org Internet	<1%
49	Harry W. Hoeijmakers, Joost Mulder. "Computational and Experimental... Crossref	<1%
50	Shantanu S. Bhat, Jisheng Zhao, John Sheridan, Kerry Hourigan, Mark ... Crossref	<1%
51	d-nb.info Internet	<1%
52	iopscience.iop.org Internet	<1%
53	pastel.archives-ouvertes.fr Internet	<1%
54	cambridge.org Internet	<1%
55	Nathan Beals, Anya R. Jones. "Lift Production by a Passively Flexible R... Crossref	<1%
56	doi.org Internet	<1%

57	dspace.library.uvic.ca:8080 Internet	<1%
58	E. van Bokhorst, R. de Kat, G. E. Elsinga, D. Lentink. "Feather roughness... Crossref	<1%
59	Hao Liu, Toshiyuki Nakata, Na Gao, Masateru Maeda, Hikaru Aono, Wei... Crossref	<1%
60	Mohamed Y. Zakaria, Farid Jafari, Muhammad R. Hajj. "PIV Measurem... Crossref	<1%
61	Robert L. Nudds. "Tuning of Strouhal number for high propulsive efficie... Crossref	<1%
62	cyberleninka.org Internet	<1%
63	library.wur.nl Internet	<1%
64	rivallab.com Internet	<1%
65	Abel-John Buchner, Nicolas Buchmann, Kareem Kilany, Callum Atkinso... Crossref	<1%
66	C. A. Ozen, D. Rockwell. "Flow structure on a rotating plate", Experimen... Crossref	<1%
67	J. LAMAR. "The use of linearized-aerodynamics and vortex-flow metho... Crossref	<1%
68	hdl.handle.net Internet	<1%

69	ir.canterbury.ac.nz Internet	<1%
70	ucf.digital.flvc.org Internet	<1%
71	A. Santhanakrishnan, A. K. Robinson, S. Jones, A. A. Low, S. Gadi, T. L. ... Crossref	<1%
72	Joel E. Guerrero. "Chapter 7 Wake Topology and Aerodynamic Perform... Crossref	<1%
73	Kim, Dae-Kwan, Jun-Seong Lee, Jae-Hung Han, Anand K. Asundi, and ... Crossref	<1%
74	Norizham Abdul Razak, Grigorios Dimitriadis. "Experimental study of wi... Crossref	<1%
75	S. C. Steele, J. M. Dahl, G. D. Weymouth, M. S. Triantafyllou. "Shape of ... Crossref	<1%
76	Y. Shah, S. Ghaemi, S. Yarusevych. "Experimental investigation of extre... Crossref	<1%
77	en.wikibooks.org Internet	<1%
78	qspace.library.queensu.ca Internet	<1%
79	A. Widmann, C. Tropea. "Parameters influencing vortex growth and det... Crossref	<1%
80	Bente Meijerink, Fernanda Leticia dos Santos, Laura Botero, Cornelis V... Crossref	<1%

81	Discetti, Stefano, and Tommaso Astarita. "The detrimental effect of inc... Crossref	<1%
82	J. Weinkauff, D. Michaelis, A. Dreizler, B. Böhm. "Tomographic PIV me... Crossref	<1%
83	Juan Alberto Franco Sumariva, Stefan J. Hein. "Adaptive Harmonic Lin... Crossref	<1%
84	M. Okamoto, A. Azuma. "Aerodynamic Characteristics at Low Reynolds... Crossref	<1%
85	MICHELE MILANO, MORTEZA GHARIB. "Uncovering the physics of flap... Crossref	<1%
86	Matthew Keennon, Karl Klingebiel, Henry Won. "Development of the Na... Crossref	<1%
87	P Wu. "Structural dynamics and aerodynamics measurements of biolo... Crossref	<1%
88	Phil F. Battley. "Contrasting extreme long-distance migration patterns i... Crossref	<1%
89	Syaiful, Anggie Restue Saputra, Nazaruddin Sinaga, Bambang Yunianti.... Crossref	<1%
90	Xu, Y.. "Calculation of the flow around turbine flowmeter blades", Flow ... Crossref	<1%
91	core-cms.prod.aop.cambridge.org Internet	<1%
92	digital.lib.washington.edu Internet	<1%

93	en.m.wikipedia.org Internet	<1%
94	enstrophy.mae.ufl.edu Internet	<1%
95	etheses.whiterose.ac.uk Internet	<1%
96	opac.ll.chiba-u.jp Internet	<1%
97	pt.scribd.com Internet	<1%
98	utwente on 2021-05-07 Submitted works	<1%
99	dlr.de Internet	<1%
100	rug.nl Internet	<1%
101	"Biological Timekeeping: Clocks, Rhythms and Behaviour", Springer Sci... Crossref	<1%
102	"Fixed and Flapping Wing Aerodynamics for Micro Air Vehicle Applicati... Crossref	<1%
103	"New Results in Numerical and Experimental Fluid Mechanics XII", Spri... Crossref	<1%
104	"Proceedings of 16th Asian Congress of Fluid Mechanics", Springer Sci... Crossref	<1%

105	"Society for Experimental Biology Annual Main Meeting", Comparative ... Crossref	<1%
106	A. C. Carruthers, A. L. R. Thomas, G. K. Taylor. "Automatic aeroelastic ... Crossref	<1%
107	Abel Arredondo-Galeana, Anna M. Young, Amanda S.M. Smyth, Ignazio... Crossref	<1%
108	Ali R Davari, Rezvan Abdollahi, Ehsaneddin Azimizadeh. "Experimental ... Crossref	<1%
109	Arjan Boonman, Yossi, Yovel, Ofri Eitan. "Wing-Beat Frequency and Its ... Crossref	<1%
110	Attar, P.J.. "Aeroelastic prediction of the limit cycle oscillations of a cr... Crossref	<1%
111	Covert, E.E.. "Magnetic balance and suspension systems for use with ... Crossref	<1%
112	D.-K. Kim. "Experimental Investigation on the Aerodynamic Characteris... Crossref	<1%
113	David B. Mayo, James L. Lankford, Moble Benedict, Inderjit Chopra. "Ex... Crossref	<1%
114	David J. Willis, Per-Olof Persson. "Multiple-Fidelity Computational Fra... Crossref	<1%
115	Dietrich Küchemann. "The Aerodynamic Design of Aircraft", American I... Crossref	<1%
116	Fritz-Olaf Lehmann. "The mechanisms of lift enhancement in insect fli... Crossref	<1%

117	Ilyas Karasu, Besir Sahin, M. Oguz Tasci, Huseyin Akilli. "Effect of Yaw ... Crossref	<1%
118	J.M. Luckring. "The discovery and prediction of vortex flow aerodynam... Crossref	<1%
119	Jafar Hasan, Anindo Roy, Kaushik Chatterjee, Prasad K. D. V. Yarlagad... Crossref	<1%
120	Kolomenskiy, D.. "Two- and three-dimensional numerical simulations o... Crossref	<1%
121	Laminar-Turbulent Transition, 2000. Crossref	<1%
122	Laura Botero, Fernanda Leticia dos Santos, Cornelis Venner, Leandro D... Crossref	<1%
123	Laura Botero-Bolívar, Fernanda L. dos Santos, Cornelis H. Venner, Lean... Crossref	<1%
124	P. Henningsson, A. Hedenstrom. "Aerodynamics of gliding flight in co... Crossref	<1%
125	Q T Truong. "A modified blade element theory for estimation of forces ... Crossref	<1%
126	S. Bull, N. Chiereghin, I. Gursul, D.J. Cleaver. "Unsteady aerodynamics ... Crossref	<1%
127	Stefan Hartman, Harry Hoeijmakers, Robert Musters. "Experimental Inv... Crossref	<1%
128	Swathi Krishna, Melissa A. Green, Karen Mulleners. "Flowfield and Forc... Crossref	<1%

129	T. Jardin, A. Farcy, L. David. "Three-dimensional effects in hovering fla... Crossref	<1%
130	Yoshifumi Suzuki. "CFD by first order PDEs", Continuum Mechanics an... Crossref	<1%
131	etd.library.vanderbilt.edu Internet	<1%
132	ia802803.us.archive.org Internet	<1%
133	lup.lub.lu.se Internet	<1%
134	open.metu.edu.tr Internet	<1%
135	strathprints.strath.ac.uk Internet	<1%
136	wiki.openfoam.com Internet	<1%
137	science.gov Internet	<1%
138	scribd.com Internet	<1%

Excluded from Similarity Report

- Bibliographic material
- Manually excluded sources
- Small Matches (Less then 8 words)

EXCLUDED SOURCES

utwente on 2022-11-23

Submitted works

97%